Quasi-Optical Active Antennas

Thesis by

Alina Moussessian

In Partial Fulfillment of the Requirements

for the Degree of

Doctor of Philosophy

California Institute of Technology

Pasadena, California

1997

(Submitted May 22, 1997)

To my Family

Acknowledgements

I would like to thank my advisor, David Rutledge, for the opportunity to work in his group. Through his support, guidance and advice I've had a fulfilling experience at Caltech.

I also wish to thank Jim Rosenberg for his suggestions, sharing his wealth of ideas, and interesting conversation. I am indebted to Peter Smith, who supported part of this work by fabricating devices at the Jet Propulsion Laboratory along with Suzi Martin, John Liu, and Rich Muller. For fabricating the terahertz frequency multipliers I would like to thank Yonjun Frank Li and Tom Crowe at the University of Virginia. Thanks to Jim Allen at the University of California, Santa Barbara for making the Free-Electron Laser available for the multiplier measurements. I am grateful to Mike Wanke and Frank Hegmann also at UCSB, who assisted with the measurements. I cannot imagine how these measurements would have been completed without their help and expertise. In operating the laser many thanks go to Dave Enyeart and the rest of the staff at the Center for Free-Electron Laser Studies. I would also like to thank the Physical Optics Corporation for their financial support.

I am glad to have had the opportunity of knowing and building friendships with many good people during my years at Caltech. For his many rescues with measurements and technical assistance I would like to thank Kent Potter. Irene Loera's pleasant conversation and birthday parties will be remembered fondly. Connie Rodrigez deserves thanks for the many last-minute requests. For his friendship and suggestions to improve this thesis I would like to thank Mike De Lisio. I am grateful to Jung-Chih Chiao, who laid most of the groundwork for the multiplier work, and for sharing his knowledge about the measurements. I also appreciate the friendship of Victor Lubecke and Olga Borić-Lubecke who made sure that I didn't forget to have a social life, and the Stimson family for always welcoming me to their home. I want to thank Polly Preventza for her

help with technical issues even when she didn't have time and for encouraging me to go back to the gym. For his friendship and good conversation I thank John Davis. Shi-Jie Li made my first year at Caltech more pleasant. Thanks to Cheh-Ming Liu whose computerized measurement setup was a big help. I feel fortunate to have had the friendship and kindness of Bobby Weikle, Scott Wedge, Jon Hacker, Moonil Kim, Yong Guo, Dave Haub, Lisa De Lisio, Armine Apcar, and Lee Burrows. I would also like to thank the more recent members of the group, Blythe Dickman and Ute Zimmerman and wish them the best of luck. I have enjoyed meeting with many visitors to the MMIC group, including Ken-Ichiro Natsume, Kazuhiro Uehara, Ashley Robinson, Minoru Saga and Eui-Joon Park. Many thanks go to Jeff Dickson not only for proofreading this thesis but also for his never-ending assistance with my computer problems.

Finally I would like to express my gratitude to my family. Without their help and support this endeavor would have not been possible. I would like to thank them for always being there for me, understanding me, and helping me pursue my goals.

So long as a man imagines that he cannot do this and that, so long is he determined not to do it, and consequently, so long is it impossible to him that he should do it.

— Benedict Spinoza

Quasi-Optical Active Antennas

Abstract

Quasi-optical power combiners such as quasi-optical grids provide an efficient means of combining the output power of many solid-state devices in free space. Unlike traditional power combiners no transmission lines are used, therefore, high output powers with less loss can be achieved at higher frequencies.

This thesis investigates four different active antenna grids. The first investigation is into X-band High Electron Mobility Transistor (HEMT) grid amplifiers. Modelling and stability issues of these grids are discussed, and gain and power measurements are presented. A grid amplifier with a maximum efficiency of 22.5% at 10 GHz and a peak gain of 11 dB is presented. The second grid is a varactor grid used as a positive feedback network for a grid amplifier to construct a tunable grid oscillator. Reflection measurements for the varactor grid show a tuning range of 1.2 GHz. The third grid is a self-complementary grid amplifier. The goal is to design a new amplifier with a unit cell structure that can be directly modelled using CAD tools. The properties of self-complementary structures are studied and used in the design of this new amplifier grid. The fourth grid is a 12×12 terahertz Schottky grid frequency doubler with a measured output power of 24 mW at 1 THz for 3.1-μs 500-GHz input pulses with a peak power of 47 W.

A passive millimeter-wave travelling-wave antenna built on a dielectric substrate is also presented. Calculations indicate that the antenna has a gain of 15 dB with 3-dB beamwidths of 10° in the H-plane and 64° in the E-plane. Pattern measurements at 90 GHz support the theory. The antenna is expected to have an impedance in the range of 50Ω to 80Ω.

Contents

Chapter 1

Introduction

Applications of millimeter-wave (30–300 GHz) and submillimeter-wave (300 GHz–3 THz) technologies have been increasing in recent years. The small wavelength in these bands enables us to build smaller and lighter equipment than is possible using microwaves. This is important in military and spaceborne applications. Moreover, components in these frequencies have broader bandwidths and higher resolution for use in radars and imaging systems.

Unlike optical waves, millimeter-waves have the ability to penetrate clouds, fog and dust. This has made millimeter-waves very attractive for military use for a long time. Recently, however, the commercial use of these frequencies is increasing. This includes collision-avoidance radars for automobiles, personal communication systems, Wireless Local Area Networks (WLAN's), and imaging systems for airplane landing [1,2]. For both military and commercial applications there is a need for high-power, low-cost components.

The interstellar medium emits energy mostly in the submillimeter-wave region, making terahertz frequencies very useful in studying the emission spectra of distant celestial bodies [3]. Submillimeter-waves can also be used in atmospheric remote sensing [4]. For example, observations in terahertz region have been successful in determining the density of many chemicals that are responsible for depleting the Antarctic ozone layer [5,6]. The interest for terahertz applications has increased the need for high-power submillimeter-wave sources, receivers and mixers.

1.1. QUASI-OPTICAL POWER COMBINING

Traditionally high-powered sources in millimeter-waves and submillimeter-waves are realized with vacuum tubes and gas lasers that are bulky, heavy, expensive and require high-voltage power supplies. On the other hand, recent advances in fabricating high frequency solid-state devices have enabled us to use solid-state components as building blocks for high power sources. However, the limitation of solid-state devices is their low output power. To overcome this, the output power of many devices is combined. Typically this is done using transmission-line combiners or resonant waveguide cavities [7]. These conventional approaches have a number of limitations, especially at higher frequencies. As the frequency increases, machining of the waveguides becomes more complicated and the radiation and conduction losses become too high, reducing the efficiency of the system. Power-combiners based on resonant cavities have narrow bandwidths and sometimes each device needs to be tuned independently. This makes the operation of many devices complicated and limits the output power using this technique.

James Mink in his 1986 paper suggested the use of quasi-optical power combining techniques of solid-state devices [8]. The output powers of many solid-state devices combine in free space, minimizing the conductor losses associated with conventional power combiners. Quasi-optical power combining has many advantages. These advantages become more apparent as the frequency increases. High output powers can be achieved with less loss at higher frequencies. Because these arrays are planar they are suitable for monolithic fabrication. They have better tolerance for failure, and are easier to tune.

1.2. QUASI-OPTICAL POWER GRIDS

A number of quasi-optical devices have been developed, including oscillators [9–13], mixers [14], multipliers [15–17], phase shifters [18,19], and amplifiers

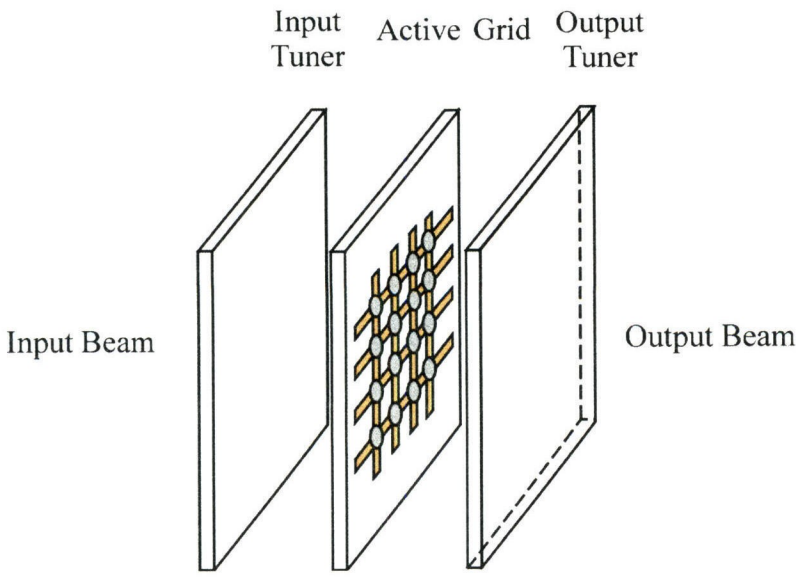

Figure 1.1. Perspective view of a quasi-optical grid. The active grid consists of an array of solid-state devices embedded in a metal structure.

[20–43]. A general quasi-optical grid is shown in Fig. 1.1. It consists of an active array of solid-state devices embedded in a metal structure. The devices and the embedding structures differ depending on the quasi-optical component. Examples of different devices are single transistors used in oscillator grids, diodes for mixers and doublers, or differential-pair transistors for amplifiers. The tuners also vary depending on the grid. Examples of tuners are mirrors for oscillator grids, polarizers for amplifier grids, and dielectric slabs for impedance matching of any grid. An interesting property of a quasi-optical grid is that the unit cell determines the driving-point impedances seen by the devices while the power scales with the grid area, provided that the grid is reasonably large. This allows one to analyze the grid by analyzing the unit cell and independently select the total grid size to meet the power requirement.

For many grid structures, it is common to find planes of symmetry which leaves the grid unchanged with respect to reflection. The simplification that re-

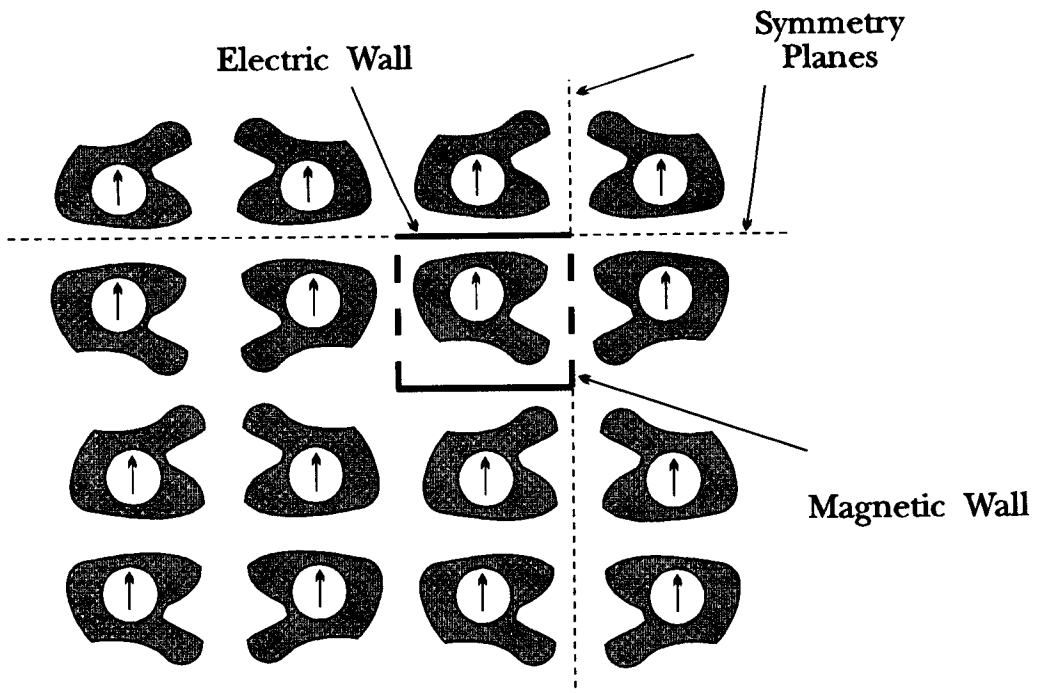

Figure 1.2. Schematic of a planar grid with reflection symmetry. Two symmetry planes are shown. The horizontal symmetry plane can be replaced with an electric wall and the vertical symmetry plane with a magnetic wall.

sults from this particular symmetry is shown in Fig. 1.2. Cells in Fig. 1.2 are assumed to contain identical AC current sources, which are locked to a single phase. Identical currents flow above and below the horizontal symmetry line, causing cancellation of the tangential electric field. This allows us to replace the horizontal symmetry lines with electric walls. Similarly the vertical symmetry lines can be replaced with magnetic walls. In this way an infinite grid can be replaced by a single waveguide. Thus, the problem of analyzing the entire grid reduces to the analysis of an equivalent waveguide. The induced EMF technique, method of moments, commercially available electromagnetic wave-solver CAD programs are some possible methods to do this analysis. An induced EMF method has been

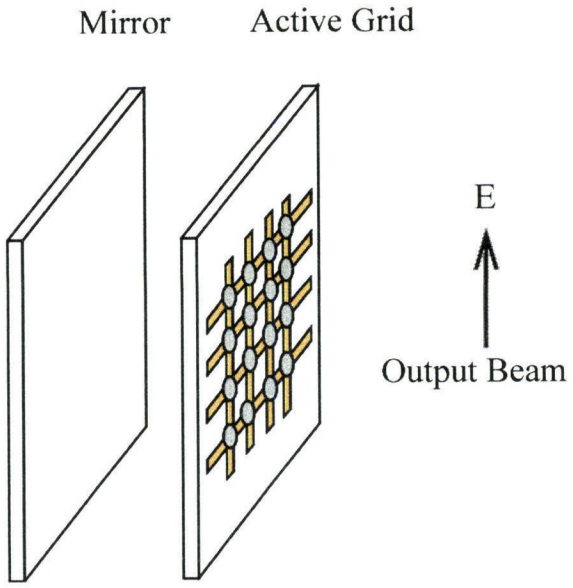

Figure 1.3. A grid oscillator. The active grid is an array of solid-state devices. The mirror is used to synchronize the individual elements.

used for the analysis of grid oscillators [11]. The Hewlett-Packard High Frequency Structure Simulator (HFSS), a 3-D finite-element electromagnetic-wave solver is used in analyzing multiplier grids [16].

1.3. QUASI-OPTICAL GRID OSCILLATORS

A grid oscillator, shown in Fig. 1.3, consists of an active array of closely spaced solid-state sources. These devices lock together in frequency and phase, producing a polarized coherent beam. A mirror provides feedback to help synchronize the individual elements and directs the output beam forward. To first order the oscillation frequency is determined by the spacing between devices, and the power is scaled with the number of elements in the grid. The first grid oscillator was a 25-element MESFET grid tested by Popović, Kim, and Rutledge [9]. The grid worked at 9.7 GHz with an output power of 460 mW. Grid oscillators can be tuned by varying the mirror position, however, the tuning range is very narrow [9,11,13].

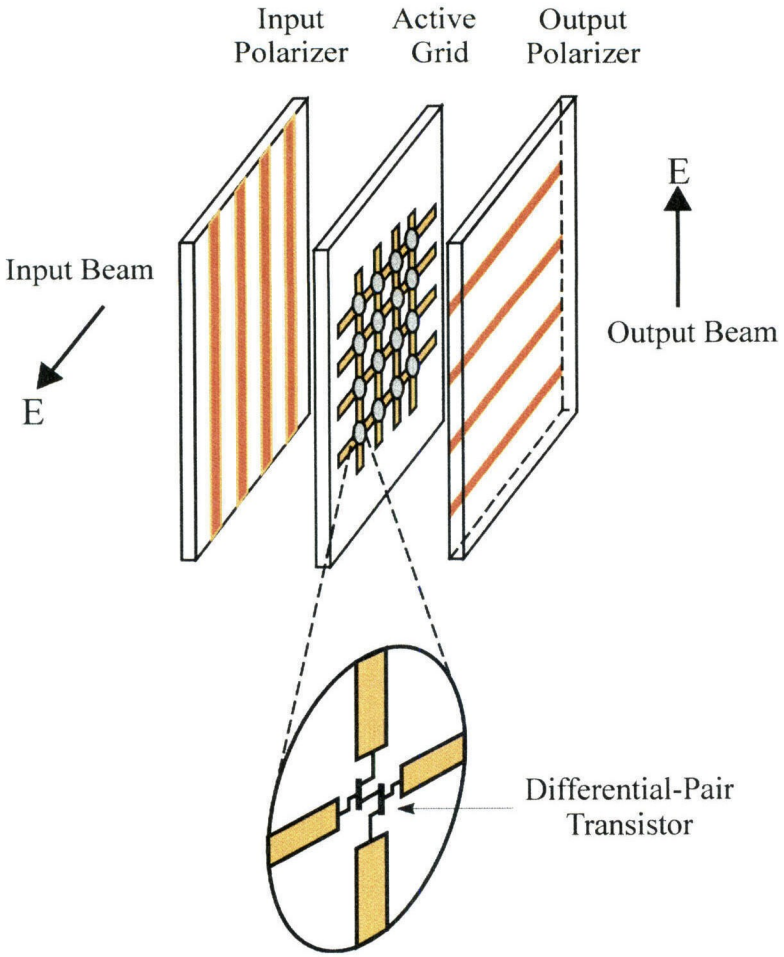

Figure 1.4. A grid amplifier. The horizontal input beam is incident from the left. The input beam passes through the input polarizer and is amplified by the active grid. The vertically polarized output beam passes through the output polarizer to the right.

1.4. QUASI-OPTICAL GRID AMPLIFIERS

Fig. 1.4 shows an amplifier grid. Horizontally polarized power is incident from the left, and passes through the input polarizer. The grid amplifies the beam and radiates it as vertically polarized output power, which passes through an output polarizer to the right. The polarizers provide isolation between the input and the output, and are used to tune the input and output independently. Table 1.1 summarizes the grid amplifier work at Caltech in chronological order. The first grid amplifier, which is also the first quasi-optical amplifier, was the

# of Cells	Devices	Type	Freq. (GHz)	Gain (dB)	Efficiency (%)	Reference
25	MESFET	Hybrid	3.3	11	—	[20]
100	HBT	Hybrid	10	10	5	[21]
16	pHEMT	Hybrid	10	8	—	[22]
16	HEMT	Hybrid	10	7	—	[22] [Chapter 3]
16	HBT	Hybrid	10	11	—	[23]
100	pHEMT	Hybrid	9	12	12	[24]
16	HEMT	Hybrid	10	11	22.5	[Chapter 3]
16	HBT	Hybrid	16	5.7	—	[25]
36	HBT	Monolithic	40	5	4	[27]
36	pHEMT	Monolithic	44–60	2.5–6.5	—	[28]

Table 1.1. Quasi-optical grid amplifiers developed at Caltech.

work of Moonil Kim [20]. This was a 25-element MESFET grid amplifier. A 100-element HBT grid amplifier, also work of Moonil Kim, followed the first grid [21]. These grids were designed empirically. Several HEMT and HBT grids followed the HBT grid. In order to design these grids transmission-line equivalent models developed by Michael De Lisio and Cheh-Ming Liu at Caltech were used [22–25]. A 40-GHz HBT monolithic grid [26,27], and a tunable 44–60 GHz pHEMT monolithic grid followed [28]. These were the first monolithic grid amplifiers and were also designed using a transmission-line equivalent model. Unlike what is described in Section 1.2 current distribution in these amplifier grids does not allow any electric or magnetic walls to be imposed on the edge of a unit cell. Therefore, instead of a direct solution using the techniques discussed in Section 1.2 a transmission-line equivalent model is used to model the cell [24].

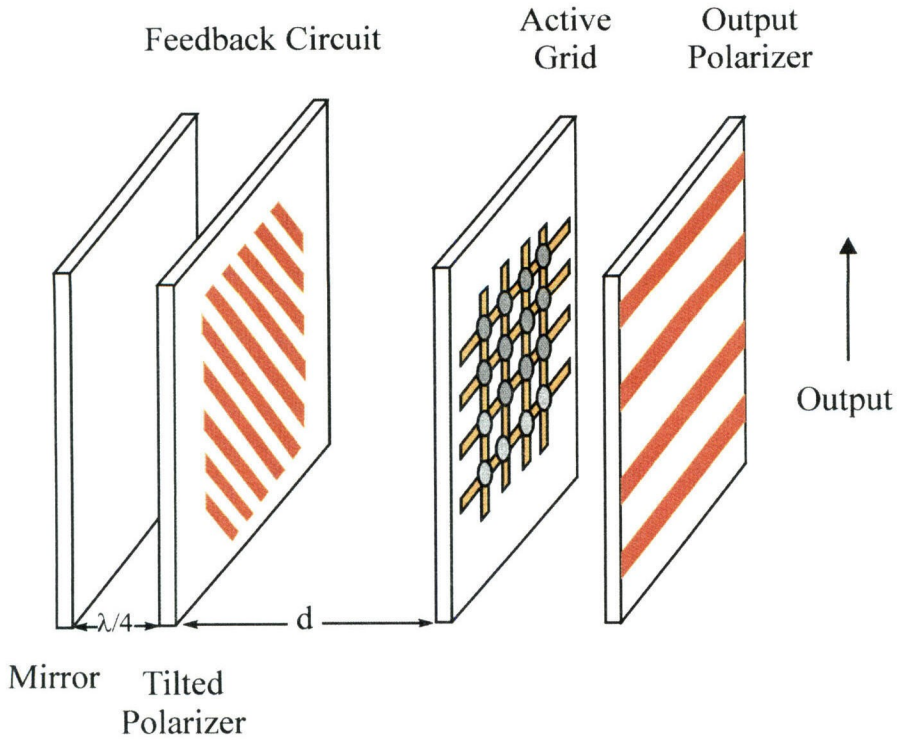

Figure 1.5. An external feedback grid frequency oscillator. The feedback circuit replaces the input polarizer of the standard grid amplifier and provides positive feedback. The spacing between the active array and the feedback circuit is varied to tune the oscillator.

1.5. AN EXTERNAL FEEDBACK OSCILLATOR

As explained in Section 1.3, the metal structure determines the operating frequency of a conventional oscillator grid while the mirror provides some tuning. Therefore the operating frequency of the grid cannot be changed after the grid is fabricated [9–13]. In an approach shown in Fig. 1.5, Moonil Kim used a grid amplifier with external positive feedback to build an oscillator [44]. The input matching polarizer of the standard grid amplifier is replaced by a 45° tilted polarizer and a mirror positioned $\lambda/4$ away. This feedback circuit provides positive feedback by converting the vertical output polarization into horizontal polarization. The oscillation frequency of the grid was tuned from 8.2 GHz to 11 GHz by varying the spacing between the active array surface and the feedback circuit.

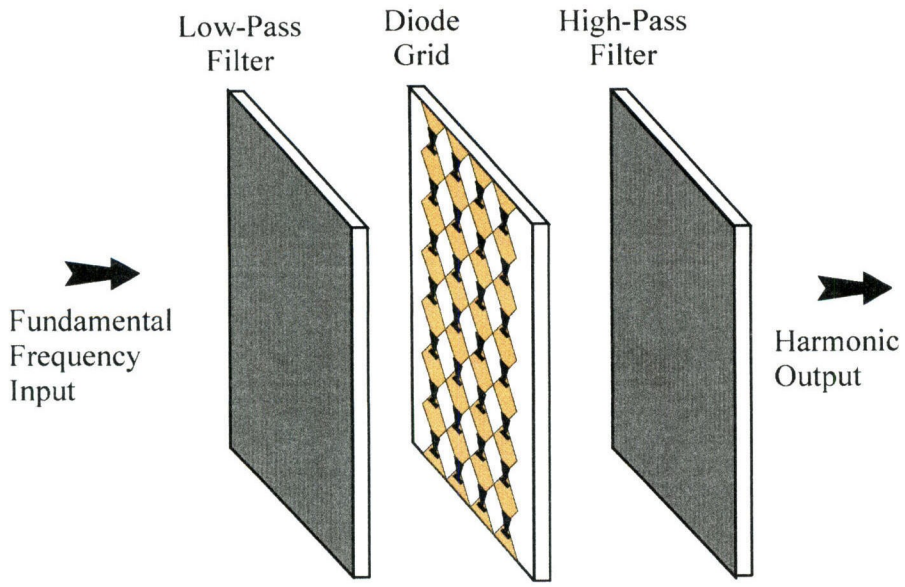

Figure 1.6. A grid frequency multiplier. The fundamental frequency enters the grid through a low-pass filter. The grid acts as a nonlinear surface and generates harmonics which pass through a high-pass filter.

1.6. QUASI-OPTICAL THz GRID FREQUENCY MULTIPLIERS

One way of generating terahertz signals is to use solid-state diode multipliers to generate higher harmonics from low-frequency tunable signal sources. Currently most of these diode multipliers are a single diode, or a cascade of two or more diodes mounted in a waveguide with a whisker contact [45–47].

Quasi-optical techniques can be used to build multipliers in submillimeter-wave frequencies. A diode-grid frequency multiplier, shown in Fig. 1.6, is an array of closely spaced planar Schottky diodes. The fundamental beam excites RF currents on the leads of the bow-tie antennas that contain the diodes. The diodes act as a nonlinear surface and generate harmonics. The low-pass filter in the input insures that only the fundamental frequency of the laser will excite the grid. The high-pass output filter allows the higher harmonics generated by the grid to pass through but blocks the fundamental. Table 1.2 shows the achievements in quasi-

# of Cells	Multiplier Type	Freq. (GHz)	Power (mW)	Efficiency (%)	Reference
760	Schottky Doubler	66	500	9.5	[48]
6000	BIN Tripler (Barrier-Intrinsic-N^+)	99	2.16	24	[49]
3100	SQBV Tripler (Schottky-Quantum-Barrier Varactor)	99	5000	2	[50]
3000	MQBV Tripler (Multi-Quantum-Barrier Varactor)	99	1250	0.7	[50]
36	Schottky Doubler	1000	0.33	0.1	[16]
144	Schottky Doubler	1000	24	0.17	[17] [Chapter 6]

Table 1.2. Quasi-optical frequency multipliers.

optical frequency multipliers. The first quasi-optical terahertz doubler grid with a peak output power of $330\,\mu$W at 1 THz was demonstrated by Chiao *et al.* [16].

1.7. ORGANIZATION OF THE THESIS

The bulk of this thesis deals with quasi-optical grids; Chapter 2, however, describes a passive millimeter-wave antenna. This is a 90-GHz V-shaped slot antenna built on a dielectric substrate. The substrate is fused quartz with a dielectric constant of 3.78. The antenna is a non-resonant travelling-wave design, with a predicted impedance of 50–80 Ω, and gain of 15 dB with 3-dB beamwidth of 10° in the H-plane and 64° in the E-plane. The design and fabrication of the antenna is discussed and measurements are compared to theory.

Chapter 3 presents the work on two X-band HEMT grid amplifiers. The devices were provided by Dr. Peter Smith at the Jet Propulsion Laboratory. A transmission-line equivalent circuit model is presented. Gain measurements are

compared to theory. One of the grids demonstrated oscillations at X-band. A stability model is presented and techniques for stabilizing the grid are discussed.

Chapter 4 discusses a tunable grid oscillator using an amplifier with external feedback. The tuning is provided by a varactor grid. The design of an X-band varactor grid is described. Preliminary measurements of the varactor grid are presented and compared to theory.

Chapter 5 presents the theory for a grid amplifier with a self-complementary structure as its unit cell. The goal is to design a new grid amplifier with cross-polarized input and output using single transistors as opposed to differential-pair devices used in conventional grid amplifiers. As discussed in Section 1.4, the current distribution on a conventional grid amplifier prevents a direct solution for the unit cell. Therefore, a transmission-line equivalent circuit model has been used to model these grids. Due to the properties of self-complementary structures it is possible to divide the unit cell into odd and even modes, solve the odd mode directly using HFSS, and find the even-mode equivalent circuit from the odd mode. By combining the odd and even-mode equivalent circuits of the unit cell the entire cell can be modelled.

Chapter 6 describes a 144-element terahertz quasi-optical grid frequency-doubler. The grid is a planar structure with bow-tie antennas as the unit cell each loaded with a planar Schottky diode. The grids were fabricated at the Semiconductor Devices Laboratory at the University of Virginia. The measurements were done at the Center for Free-Electron Laser Studies at the University of California, Santa Barbara. A peak output power of 24 mW is measured at 1 THz for 3.1-μs 500-GHz input pulses with a peak power of 47 W.

Chapter 7 discusses the directions for future work in the area of quasi-optical power combining.

References

[1] G.C. DiPiazza, "Dual-Use and Defense Conversion: A View from the Second Tier," *1995 IEEE MTT-S Int. Microwave Symp. Dig.*, pp. 1059–1062, 1995.

[2] L.Q. Bui, Y. Alon, D. Neilson, "Extended Range Coverage of an Imaging Radar System with Feed-Mounted 94 GHz MIMIC Low Noise Amplifier and External ILO," *1992 IEEE MTT-S Int. Microwave Symp. Dig.*, pp. 687–690, 1992.

[3] T.G. Phillips, "Development in Submillimeter Astronomy," *The 19th International Conference on Infrared and Millimeter Waves,* Sendai, Japan, Oct. 1994.

[4] J.W. Waters and P.H. Siegel, "Applications of Millimeter and Submillimeter Technology to Earth's Upper Atmosphere: Results To Date and Potential for the Future," *The 4th International Symposium on Space Terahertz Technology,* Los Angeles, CA, March 1993.

[5] J. Farman, B. Gardiner, J. Shanklin, "Large Losses of Total Ozone in Antarctica Reveal Seasonal ClO_x/NO_x Interaction," *Nature*, vol. 315, pp. 207, 1985.

[6] P.B. Hayes and H.E. Snell, "Atmospheric Remote Sensing in the Terahertz Region," *The 1st Int. Symp. Space Terahertz Tech.*, pp. 482, 1990.

[7] K. Chang, C. Sun, "Millimeter-Wave Power Combining Techniques," *IEEE Trans. Microwave Theory Tech.*, vol. 31, pp. 91–107, Feb. 1983.

[8] J.W. Mink, "Quasi-Optical Power Combining of Solid-State Millimeter-Wave Sources," *IEEE Trans. Microwave Theory Tech.*, vol. 34, pp. 273–279, Feb. 1986.

[9] Z.B. Popović, M. Kim, D.B. Rutledge, "Grid Oscillators," *Int. J. Infrared Millimeter Waves*, vol. 9, pp. 647–654, July 1988.

[10] Z.B. Popović, R.M. Weikle, M. Kim, D.B. Rutledge, "A 100-MESFET Planar Grid Oscillator," *IEEE Trans. Microwave Theory Tech.*, vol. 39, pp. 193–200, March 1990.

[11] R.M. Weikle, M. Kim, J.B. Hacker, M.P. De Lisio, D.B. Rutledge, "Planar MESFET Grid Oscillators Using Gate Feedback," *IEEE Trans. Microwave Theory Tech.*, vol. 40, pp. 1997–2003, Nov. 1992.

[12] J.B. Hacker, M.P. De Lisio, M. Kim, C.-M. Liu, S.-J. Li, S.W. Wedge, D.B. Rutledge, "A 10-Watt X-Band Grid Oscillator," *1994 IEEE MTT-S Int. Microwave Symp. Dig.*, pp. 823–826, 1994.

[13] P. Preventza, M. Matloubian, D.B. Rutledge, "A 43-GHz AlInAs/GaInAs/InP HEMT Grid Oscillator," to be presented at *The IEEE MTT-S Int. Microwave Symp.*, June 1997.

[14] J.B. Hacker, R.M. Weikle, M. Kim, M.P. De Lisio, D.B. Rutledge, "A 100-Element Planar Schottky Diode Grid Mixer," *IEEE Trans. Microwave Theory Tech.*, vol. 40, pp. 557–562, March 1992.

[15] H.-X.L. Liu, L.B. Sjogren, C.W. Domier, N.C. Luhmann, Jr., D.L. Sivco, A.Y. Cho, "Monolithic Quasi-Optical Frequency Tripler Array with 5-W Output Power at 99 GHz," *IEEE Electron Device Lett.*, vol. 14, pp. 329–331, July 1993.

[16] J.-C. Chiao, A. Markelz, Y. Li, J. Hacker, T. Crowe, J. Allen, D.B. Rutledge, "Terahertz Grid Frequency Doublers," presented at *The 6th Int. Symp. Space Terahertz Tech.*, March 1995.

[17] A. Moussessian, M.C. Wanke, Y. Li, J.-C. Chiao, F.A. Hegmann, S.A. Allen, T.W. Crowe, D.B. Rutledge, "A Terahertz Grid Frequency Doubler," to be presented at *The IEEE MTT-S Int. Microwave Symp.*, June 1997.

[18] W.W. Lam, H.Z. Chen, K.S. Stolt, C.F. Jou, N.C. Luhmann, Jr., D.B. Rutledge, "Millimeter-Wave Diode Grid Phase Shifters," *IEEE Trans. Microwave Theory Tech.*, vol. 36, pp. 902–907, May 1988.

[19] L.B. Sjogren, H.-X.L. Liu, X.-H. Qin, C.W. Domier, N.C. Luhmann, Jr., "Phased Array Operation of a Diode Grid Impedance Surface," *IEEE Trans. Microwave Theory Tech.*, vol. 42, pp. 565–572, April 1994.

[20] M. Kim, J.J. Rosenberg, R.P. Smith, R.M. Weikle, J.B. Hacker, M.P. De Lisio, D.B. Rutledge, "A Grid Amplifier," *IEEE Microwave Guided Wave Lett.*, vol. 1, pp. 322–324, Nov. 1991.

[21] M. Kim, E.A. Sovero, J.B. Hacker, M.P. De Lisio, J.-C. Chiao, S.-J. Li, D.R. Gagnon, J.J. Rosenberg, D.B. Rutledge, "A 100-Element HBT Grid Amplifier," *IEEE Trans. Microwave Theory Tech.*, vol. 41, pp. 1762–1771, Oct. 1993.

[22] D.B. Rutledge, A. Moussessian, M.P. De Lisio, C.-M. Liu, J.J. Rosenberg, "Modelling of Transistor Grid Amplifiers," *1994 IEEE MTT-S Int. Microwave Symp.*, Workshop Notes, WFFA: Circuit Level Design and Modelling of Quasi-Optical Circuits and Systems, pp. C.1–C.16, 1994.

[23] C.-M. Liu, E.A. Sovero, M.P. De Lisio, A. Moussessian, J.J. Rosenberg, D.B. Rutledge, "Gain and Stability Models for HBT Grid Amplifiers," *1995 IEEE AP-S Int. Symp. Dig.*, pp. 1292–1295, 1995.

[24] M.P. De Lisio, S.W. Duncan, D.-W. Tu, C.-M. Liu, A. Moussessian, J.J. Rosenberg, D.B. Rutledge, "Modelling and Performance of a 100-Element pHEMT Grid Amplifier," *IEEE Trans. Microwave Theory Tech.*, vol. 44, pp. 2136–2144, December 1996.

[25] C.-M. Liu, "Monolithic Grid Amplifiers," Ph.D. Thesis, California Institute of Technology. Pasadena, CA, 1996.

[26] C.-M. Liu, E.A. Sovero, W.J. Ho, J.A. Higgins, D.B. Rutledge, "A Millimeter-Wave Monolithic Grid Amplifier," *Int. Journal of Infrared and Millimeter Waves*, vol. 16, pp. 1901–1910, Nov. 1995.

[27] C.-M. Liu, E.A. Sovero, W.J. Ho, J.A. Higgins, M.P. De Lisio, D.B. Rutledge, "Monolithic 40-GHz 670-mW HBT Grid Amplifier," *1996 IEEE MTT-S Int. Microwave Symp.*, pp. 1123–1126, 1996.

[28] M.P. De Lisio, S.W. Duncan, D.-W. Tu, S. Weinreb, C.-M. Liu, D.B. Rutledge, "A 44-60 GHz Monolithic pHEMT Grid Amplifier," *1996 IEEE MTT-S Int. Microwave Symp.*, pp. 1127–1130, 1996.

[29] C.-Y. Chi, G.M. Rebeiz, "A Quasi-Optical Amplifier," *IEEE Microwave Guided Wave Lett.*, vol. 3, pp. 164–166, June 1993.

[30] T.P. Budka, M.W. Trippe, S. Weinreb, G.M. Rebeiz, "A 75 GHz to 110 GHz Quasi-Optical Amplifier," *IEEE Trans. Microwave Theory Tech.*, vol. 42, pp. 899–901, May 1994.

[31] N. Kolias, R.C. Compton, "A Microstrip-Based Unit Cell for Quasi-Optical Amplifier Arrays," *IEEE Microwave Guided Wave Lett.*, vol. 3, pp. 330–332, Sept. 1993.

[32] T. Mader, J. Schoenberg, L. Harmon, Z.B. Popović, "Planar MESFET Transmission Wave Amplifier," *Electronics Lett.*, vol. 29, pp. 1699–1701, Sept. 1993.

[33] H.S. Tsai, R.A. York, "Polarization-Rotating Quasi-Optical Reflection Amplifier Cell," *Electronics Lett.*, vol 29, pp. 2125–2127, Nov. 1993.

[34] N. Sheth, T. Ivanov, A. Balasubramaniyan, A. Mortazawi, "A Nine HEMT Spatial Amplifier," *1994 IEEE MTT-S Int. Microwave Symp. Dig.*, pp. 1239–1242, 1994.

[35] J.S.H. Schoenberg, S.C. Bundy, Z.B. Popović, "Two-Level Power Combining Using a Lens Amplifier," *IEEE Trans. Microwave Theory Tech.*, vol. 42, pp. 2480–2485, Dec. 1994.

[36] T. Ivanov, A. Mortazawi, "Two Stage Double Layer Microstrip Spatial Amplifiers," *1995 IEEE MTT-S Int. Microwave Symp. Dig.*, pp. 589–592, 1995.

[37] J. Schoenberg, T. Mader, B. Shaw, Z.B. Popović, "Quasi-Optical Antenna Array Amplifiers," *1995 IEEE MTT-S Int. Microwave Symp. Dig.*, pp. 605–608, 1995.

[38] J.S.H. Schoenberg, T.B. Mader, J.W. Dixon, B.L. Shaw, Z.B. Popović, "Quasi-Optical Antenna Array Amplifiers," submitted to *IEEE Trans. Microwave Theory Tech.*, March 1995.

[39] T. Ivanov, A. Balasubramaniyan, A. Mortazawi, "One- and Two-Stage Spatial Amplifiers," *IEEE Trans. Microwave Theory Tech.*, vol. 43, pp. 2138–2143, Sept. 1995.

[40] H.S. Tsai, M.J.W. Rodwell, R.A. York, "Planar Amplifier Array With Improved Bandwidth Using Folded-Slots," *IEEE Microwave Guided Wave Lett.*, vol. 4, pp. 112–114, April 1994.

[41] H.S. Tsai, R.A. York, "Quasi-Optical Amplifier Array using Direct Integration of MMICs and 50 Ω Multi-Slot Antennas," *1995 IEEE MTT-S Int. Microwave Symp. Dig.*, pp. 593–596, 1995.

[42] J. Hubert, J. Schoenberg, Z.B. Popović, "High-Power Hybrid Quasi-Optical Ka-Band Amplifier Design," *1995 IEEE MTT-S Int. Microwave Symp. Dig.*, pp. 585–588, 1995.

[43] J.A. Higgins, E.A. Sovero, W.J. Ho, "44-GHz Monolithic Plane Wave Amplifiers," *IEEE Microwave Guided Wave Lett.*, vol. 5, pp. 347–348, Oct. 1995.

[44] M. Kim, E.A. Sovero, J.B. Hacker, M.P. De Lisio, J.J. Rosenberg, D.B. Rutledge, "A 6.5 GHz–11.5 GHz Source Using a Grid Amplifier with a Twist Reflector," *IEEE Trans. Microwave Theory Tech.*, vol. 41, pp. 1772–1774, October 1993.

[45] A. Rydberg, B.N. Lyons and S.U. Lidholm, "On the Development of a High Efficiency 750 GHz Frequency Tripler for THz Heterodyne Systems," *IEEE Trans. on Microwave Theory and Tech.*, vol. 40, No. 5, pp. 827-830, May 1992.

[46] N. Erickson and J. Tuovinen, "A Waveguide Tripler for 800-900 GHz," *The 6th International Symposium on Space Terahertz Technology,* Pasadena, CA, March 1995.

[47] R. Zimmermann, T. Rose and T. Crowe, "An All Solid-State 1 THz Radiometer for Space Applications," *The 6th International Symposium on Space Terahertz Technology,* Pasadena, CA, March 1995.

[48] E.R. Brown, "Submillimeter-wave Resonant-Tunneling Oscillators," *The Proceedings of the 1st International Symposium on Space Terahertz Technology,* pp. 74–83, 1990.

[49] D.P. Steenson, R.D. Pollard, R.E. Miles and J.M. Chamberlain, "Power-Combining of Resonant Tunnelling Diode Oscillators ar W-band," *The 19th International Conference on Infrared and Millimeter Waves,* Sendai, Japan, 1994.

[50] E.R. Brown, C.D. Parker, A.R. Calawa, M.J. Manfra, C.L. Chen, L.J. Mahoney, W.D. Goodhue, J.R. Soderstromt and T.C. McGill, "High Frequency Resonant-tunneling Oscillators," *Microwave and Optical Technology Letters,* vol. 4, No. 1, Jan. 5, 1991.

Chapter 2

A Millimeter-Wave Slot-V Antenna

In this chapter, a new V-shaped slot antenna built on a dielectric substrate is discussed. The antenna is a non-resonant, travelling-wave design, with a predicted impedance in the range from 50 Ω to 80 Ω. Calculations indicate that this antenna should have a gain of 15 dB with 3-dB beamwidths of 10° in the H-plane and 64° in the E-plane. Pattern measurements at 90 GHz support the theory. Fabrication is simple, and it should be possible to make this antenna at wavelengths as short as 10 μm with conventional photolithography.

2.1. INTRODUCTION

In millimeter-wave MMIC receivers and transmitters it is desirable to integrate the receiving and transmitting antennas with the rest of the circuit. Since these circuits are built on dielectric materials such as silicon or GaAs, construction of antennas on these dielectric materials are of interest.

In general, antennas on dielectric substrates suffer from losses to substrate modes, and tend to have low gain and poor patterns. An example of this is the bow-tie antenna [1]. An elegant way to solve the substrate problem is to fabricate the antennas on silicon-oxynitride membranes inside horns [2], but this requires sophisticated fabrication techniques. An alternative is to add a superstrate so that the antenna is entirely inside the dielectric, to make a sandwich. This has been demonstrated with a V antenna [3]. Here we propose a simpler approach, a slot antenna in the shape of a V [4–6], Fig. 2.1. A V-shaped slot is fabricated

by evaporation and lift-off on top of a dielectric substrate, in this case fused quartz. The arm length of the V is $5\lambda_d$, where λ_d is the wavelength inside the dielectric. The slot angles are $\phi_1 = 57.5°$ and $\phi_2 = 10°$. The substrate is 25-mm square and 14-mm thick. A diode is mounted at the apex of the antenna, and acts as a detector. The slot extensions of the V are used for DC isolation. One can get a feeling for how the slot-V works by considering how waves propagate along conductors at a dielectric interface. A wave in a slot tends to propagate at a velocity that is intermediate between the velocity of waves in air and the velocity of waves in the dielectric. The wave is slow compared to the air

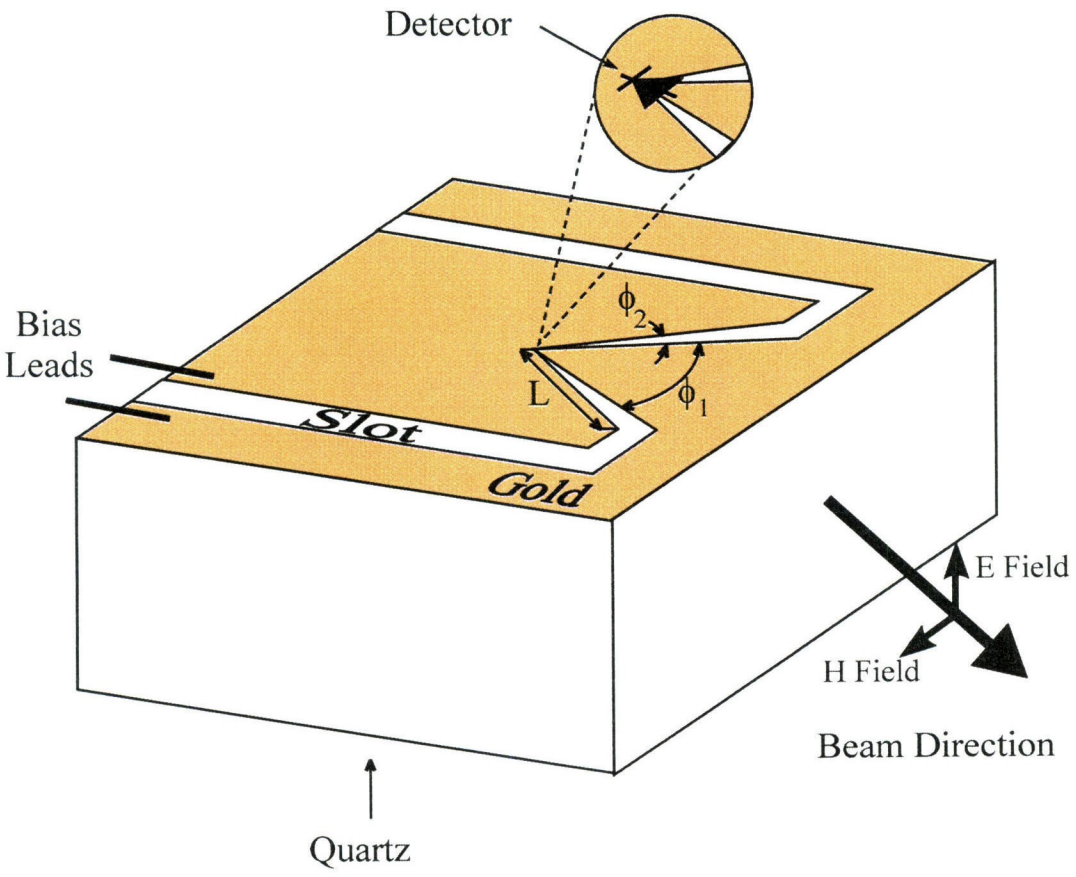

Figure 2.1. Diagram of the slot-V antenna on fused quartz. The arm length L is $5\lambda_d$. The slot angles are $\phi_1 = 57.5°$ and $\phi_2 = 10°$.

velocity, and excites primarily evanescent waves in the air. This means that little power radiates directly into the air. On the other hand, the wave velocity is fast compared to the dielectric velocity, and the antenna radiates strongly into the dielectric at an angle $\psi = \arccos(v_d/v_s)$, where v_s is the slot phase velocity and v_d is the dielectric velocity [7]. When the angle between the slot arms is twice this radiation angle, the radiation from the two arms adds in phase, producing a strong beam on the V axis.

2.2. THEORY

This is a non-resonant travelling-wave antenna, and we can estimate the impedance as a special case of a conformal-mapping formula developed for V-couplers [8]:

$$Z = \left(\frac{\eta_0}{4n_e}\right)\left(\frac{K'(m)}{K(m)}\right), \tag{2.1}$$

where η_0 is the free-space wave impedance, and n_e, the effective refractive index is given by $\sqrt{\frac{\epsilon_r+1}{2}}$, where ϵ_r is the relative dielectric constant of the substrate. The assumption is that propagation is similar to that in a material that has a dielectric constant that is the mean of the dielectric constant of the substrate and the dielectric constant of air. The dielectric constant of fused quartz is 3.78 [9]. The functions K and K' are elliptic integrals, and the parameter m is given by:

$$m = \left(\frac{\tan(\phi_1/4)}{\tan(\phi_1/4+\phi_2/2)}\right)^2. \tag{2.2}$$

Fig. 2.2 shows a plot of the impedance as a function of ϕ_1, with ϕ_2 as a parameter. For convenient angles the impedance ranges between 50 Ω and 80 Ω. The dashed line in the figure shows an impedance of approximately 60 Ω for $\phi_1 = 57.5°$ and $\phi_2 = 10°$.

To estimate the radiation pattern of the slot-V inside the dielectric, we assume a radial magnetic current in the left slot of the form:

$$I_m = \exp(-jn_e k_0 r), \tag{2.3}$$

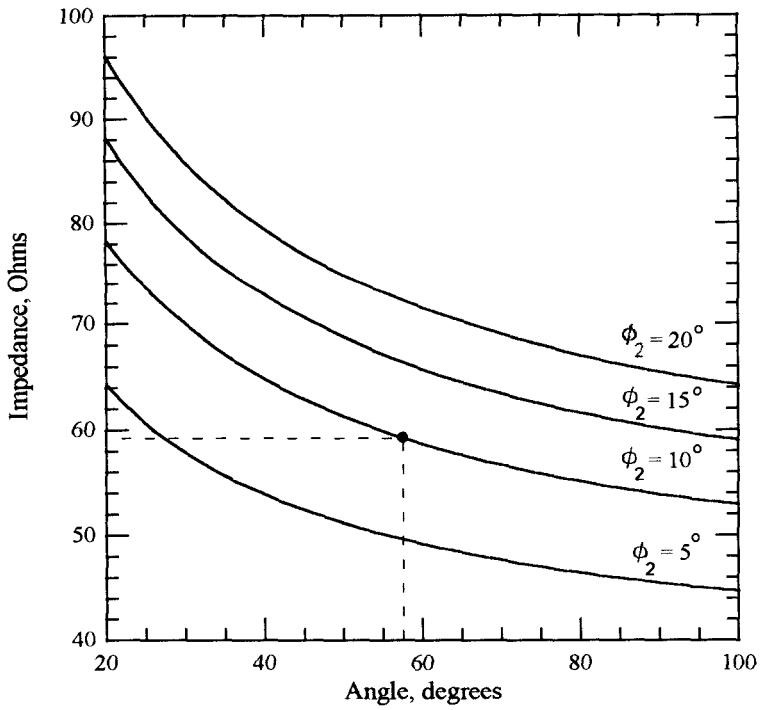

Figure 2.2. Impedance of the slot-V antenna, calculated from (2.1).

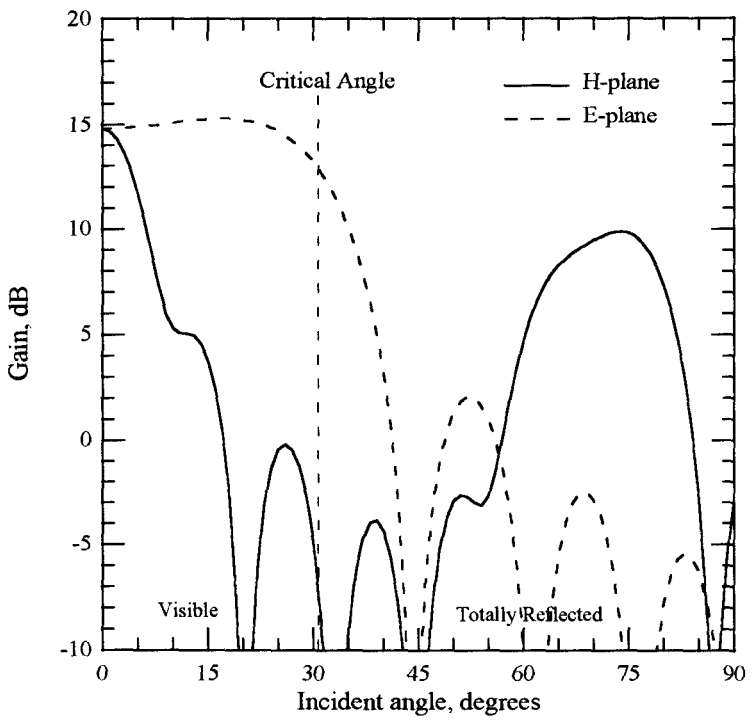

Figure 2.3. Calculated slot-V patterns in the dielectric. The critical angle of fused quartz is shown in the figure.

where k_0 is the propagation constant of free space. The magnetic current for the right slot changes sign. We can then integrate these currents to calculate the magnetic radiation vectors and the pattern in the dielectric [10].

The patterns are shown in Fig. 2.3. The gain on axis is 15 dB and the 3-dB beamwidths are 10° in the H-plane and 64° in the E-plane. The critical angle of fused quartz which is also shown in Fig. 2.3 is approximately 30.9°. Only part of the pattern with angles less than the critical angle is visible outside the dielectric. The pattern with angles larger than the critical angle is totally reflected, therefore the large sidelobe of the H-plane at 75° is not visible in the pattern measured in air.

The theoretical two-dimensional co-polarized and cross-polarized patterns of the antenna inside the dielectric are shown in Fig. 2.4. The angle ϕ is the azimuth angle and θ is the angle from the vertical. The antenna has a relatively strong cross-polarized radiation.

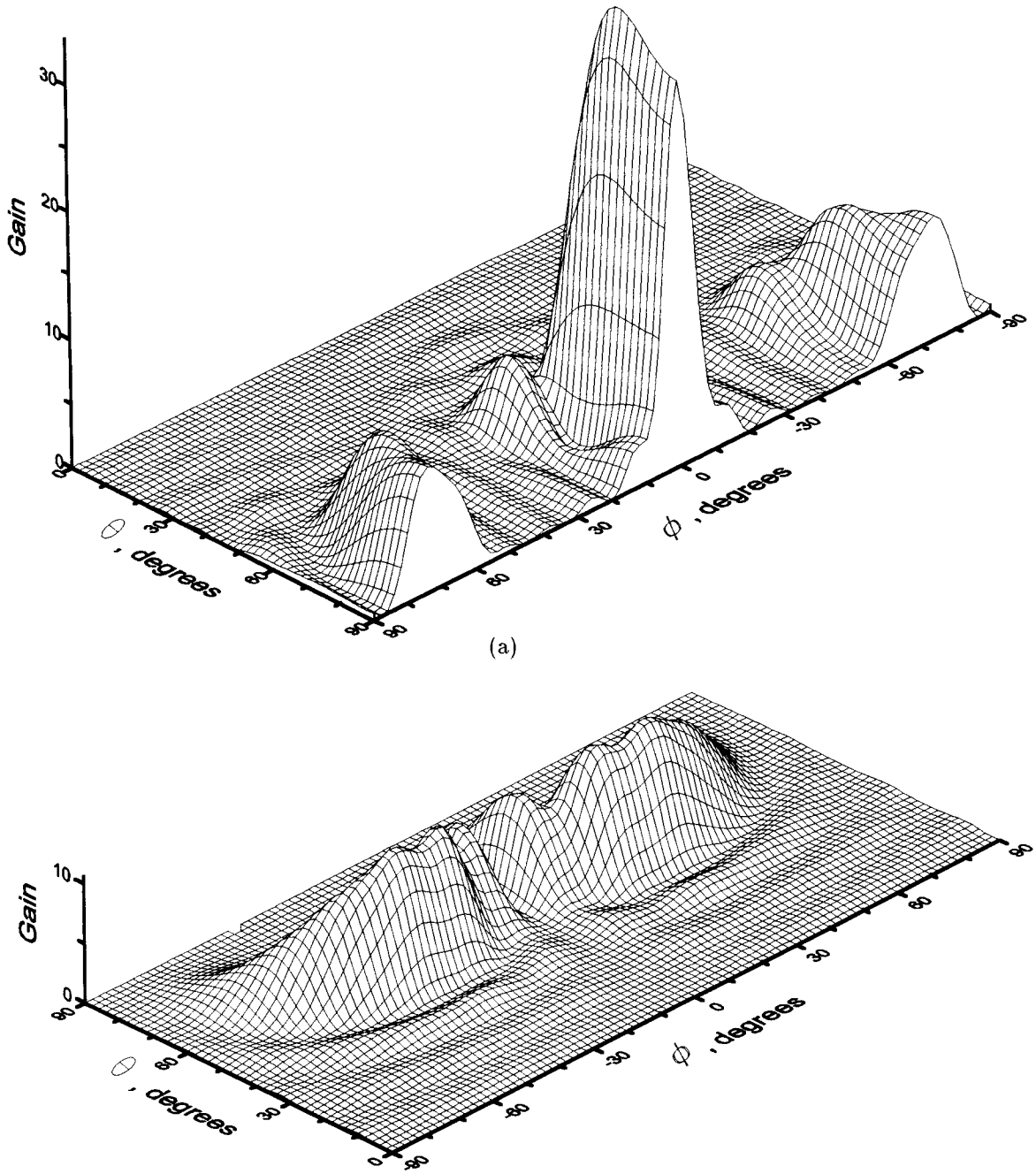

Figure 2.4. Two-dimensional theoretical radiation patterns. (a) Co-polarized pattern. (b) Cross-polarized pattern.

2.3. FABRICATION AND MEASUREMENTS

The antenna is fabricated by evaporation and lift-off. The metal film is a 1600-Å layer of gold on top of 120 Å of chrome. A M/A-Com GaAs Schottky diode (MA40417), mounted across the slot at the apex of the V, acts as a detector. A photograph of the slot-V antenna is shown in Fig. 2.5. The diode is biased at 100 μA. The substrate is covered with absorber on the bottom face and three side faces, so that the antenna receives power only from the front and top faces.

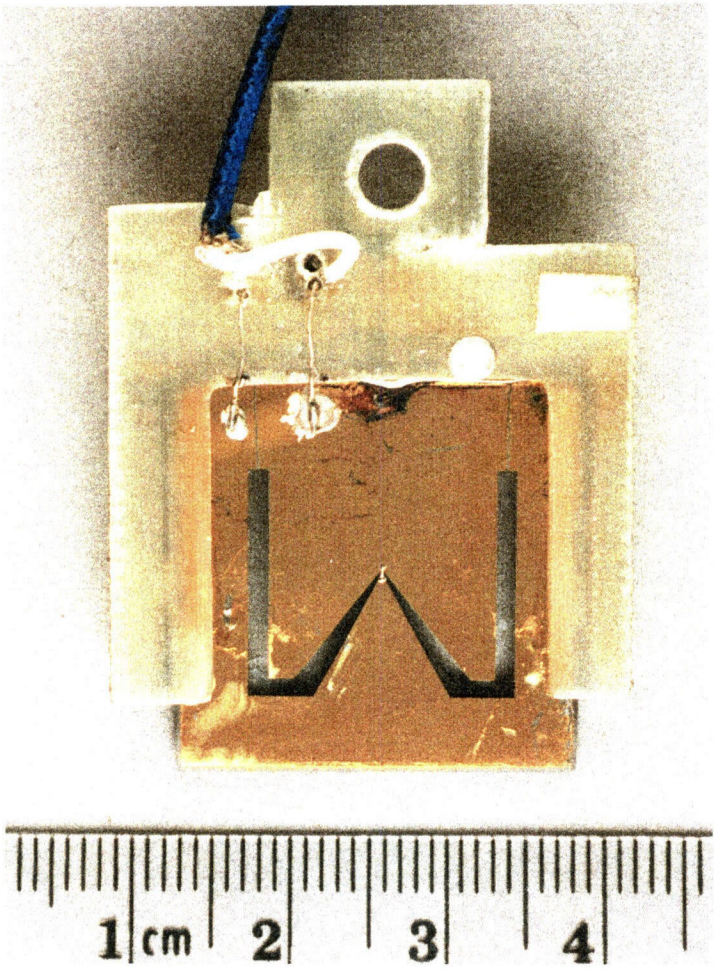

Figure 2.5. Photograph of the slot-V antenna.

The measurement setup is shown in Fig. 2.6. The transmitting antenna is a horn. The source is a HP 83558A millimeter-wave multiplier, driven by a HP 83620 synthesized sweeper with a HP 8349B amplifier. A EG&G Princeton Applied Research model 5210 lock-in amplifier is used to measure the output signal from the diode. The setup is computer controlled to facilitate data collection.

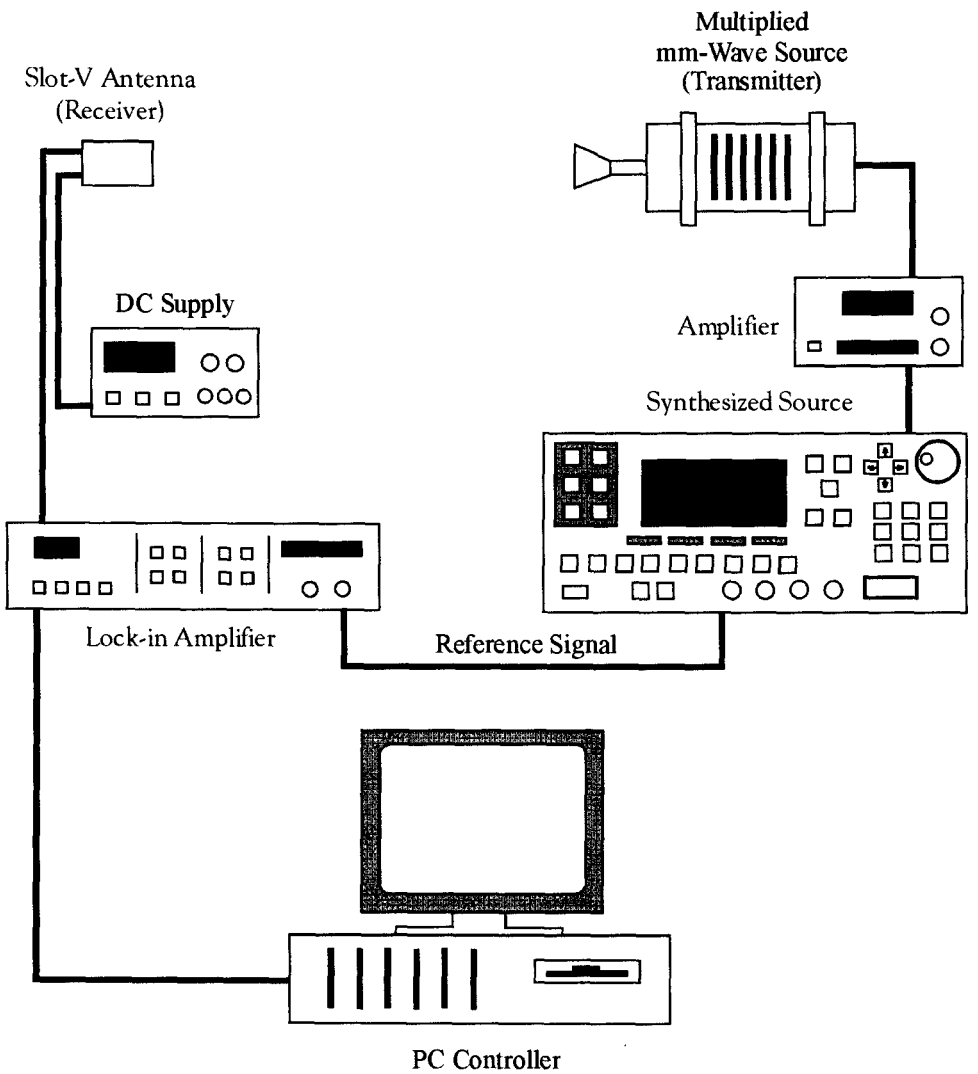

Figure 2.6. Setup used to measure the E-plane and H-plane patterns of the antenna.

The measured patterns are shown in Fig. 2.7. In the E-plane (Fig. 2.7(a)) the antenna is much more sensitive to radiation from the dielectric side. The peak in the pattern is not along the antenna axis but is 20° off. We suspect that this effect comes from the fact that the edge of the groundplane is only 12 mm from the apex of the V. The measured pattern decays faster than theory predicts, and this may be due to the fact that the substrate is only 14-mm thick. The theoretical pattern is for dielectric incidence only (Fig. 2.3), and takes reflection and refraction through the front face into account. Waves with an incident angle greater than 30.9° (the critical angle of fused quartz) are totally reflected. Fig. 2.7(b) is the measured H-plane pattern. This pattern is actually measured at 20° in the E-plane, where the gain is maximum. The theory is for an E-plane angle of 0°, and takes reflection and refraction through the front face into account. In the H-plane theory and experiment agree. The patterns are broader than in Fig. 2.3, primarily because of refraction at the front face of the substrate.

In many applications it is desirable that E-plane and H-plane beamwidths be the same so that the antenna can couple efficiently to an optical system. It should be possible to equalize the two beamwidths with a cylindrical lens that would reduce the E-plane beamwidth without changing the H-plane beamwidth. The broad bandwidth and high gain characteristics make the slot-V a good candidate for picosecond optoelectronic measurements [11–13].

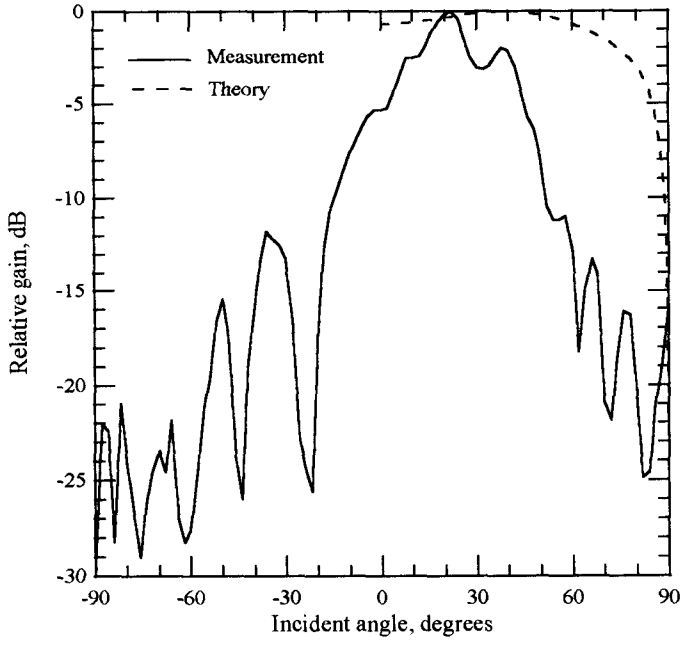

(a)

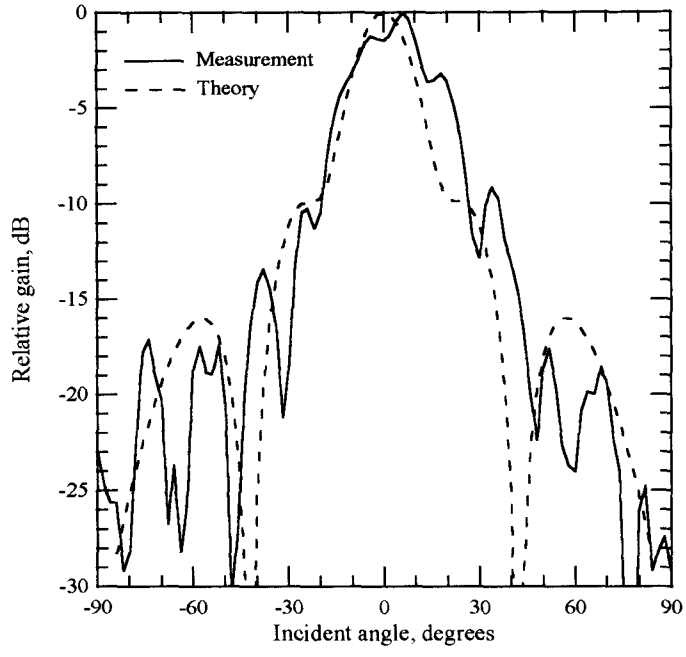

(b)

Figure 2.7. (a) Measured 90-GHz E-plane pattern. For positive angles, radiation is incident from the dielectric, and for negative angles, radiation is incident from the air. (b) Measured 90-GHz H-plane pattern.

2.4. FUTURE WORK

As discussed earlier, it is predicted that the application of this antenna will be mostly on material such as silicon or GaAs which have higher dielectric constants than fused quartz used in our measurements. Therefore it is useful to investigate the properties of a slot-V on high dielectric constant material. Our calculations predict a gain of approximately 16 dB and 3 dB beamwidths of 7° in the H-plane and 55° in the E-plane for a slot-V on silicon ($\epsilon_r = 11.9$). This is a design similar to Fig. 2.1 with $\phi_1 = 72°$ and $\phi_2 = 14°$ [5].

Lee Burrows at Caltech has designed slot-V antennas on $LiNbO_3$ ($\epsilon_r = 28$) for use with his traveling-wave electro-optic modulators at 20 GHz, 44 GHz, and 100 GHz. Measurements are in progress.

References

[1] R.C. Compton, R.C. McPhedran, Z. Popović, G.M. Rebeiz, P.P. Tong, and D. B. Rutledge, "Bow-Tie Antenna on a Dielectric Half-Space: Theory and Experiment," *IEEE Trans. on Antennas and Propagation, AP-35,* pp. 622–631, June 1987.

[2] G.V. Eleftheriades, W.Y. Ali-Ahmad, L.P. Ketehi, G.M. Rebeiz, "Millimeter-Wave Integrated-Circuit Horn Antennas, Part I–Theory, Part II–Experiment," *IEEE Trans. on Antennas and Propagation, AP-39,* pp. 1575–1586, November 1991.

[3] D.B. Rutledge, S.E. Schwartz, and A.T. Adams, "Infrared and Submillimeter Antennas," *Infrared Physics, 18,* pp. 713–729, 1978.

[4] A. Moussessian, D.B. Rutledge,"A Millimeter-Wave Slot-V Antenna," *1992 IEEE AP-S Int. Symp. Dig.,* pp. 1894–1897, 1992.

[5] A. Moussessian, D.B. Rutledge, "A Millimeter-Wave Slot-V Antenna," *17th International Conference on Infrared and Millimeter Waves,* pp. 282–283, 1992.

[6] D.B. Rutledge, "High-Gain Broadband V-Shaped Slot Antenna," *U.S. patent no. 5,404,146,* granted April 4, 1995.

[7] D.B. Rutledge, D.P. Neikirk, D.P. Kasilingam, "Integrated Circuit Antennas," in *Infrared and Millimeter Waves, 10,* K. J. Button, ed., Academic Press, Inc., 1983, pp. 1–90.

[8] D.B. Rutledge, S.E. Schwarz, T.L. Hwang, D.J. Angelakos, K.K. Mei, and S. Yokota, *IEEE J. Quantum Electronics, QE-16,* pp. 508–516, May 1980.

[9] *Reference Data for Radio Engineering,* sixth ed., Howard W. Sams & Co., Inc., pp. 4–28. The dielectric constant for fused quartz is quoted at 25 GHz.

[10] S. Ramo, J.R. Whinnery, and T. Van Duzer, *Fields and Waves in Communication Electronics.* John Wiley & Sons, Inc., 1965, sec. 12.10 and 12.16.

[11] Y. Konishi, M. Kamegawa, M. Case, R. Yu, S.T. Allen, and M.J.W. Rodwell, "A Broadband Free-Space Millimeter-Wave Vector Transmission Measurement System," *IEEE Trans. on Microwave Theory and Techniques, 42,* pp. 1131–1139, July 1994.

[12] G. Arjavalingam, Y. Pastol, J.M. Halbout, and G.V. Kopcsay, "Broad-Band Microwave Measurements with Transient Radiation from Optoelectronic Pulsed Antennas," *IEEE Trans. on Microwave Theory and Techniques, 38,* pp. 615–621, May 1990.

[13] W.M. Robertson, G.V. Kopcsay, and G. Arjavalingam, "Picosecond Time-Domain Electromagnetic Scattering from Conducting Cylinders," *IEEE Microwave and Guided Wave Letters, MGWL1,* pp. 371–373, December, 1991.

Chapter 3

Hybrid X-Band HEMT Amplifier Grids

This chapter discusses two 16-element X-band High Electron Mobility Transistor (HEMT) grid amplifiers. A gain model for the grid amplifier is presented and compared to measurements. The active devices are custom-made differential-pair HEMT's provided by Dr. Peter Smith at the Jet Propulsion Laboratory. The first grid has a gain of 7 dB at 10 GHz. The second grid with 20-Ω stabilizing resistors, has a gain of 11 dB at 10 GHz. The saturated output power is 166 mW at 10 GHz, with a peak power-added efficiency of 22.5%.

3.1. INTRODUCTION

Quasi-optical amplifiers combine the output power of many devices in free space, eliminating the conductor losses associated with waveguides or transmission-line combiners. A grid amplifier is an array of closely-spaced differential pairs of transistors. Fig. 3.1 shows the approach. The horizontal input beam excites RF currents on the input leads, which drives the transistors in the differential mode. This in turn generates currents on the output leads. These currents radiate as a vertically-polarized output beam. The polarizers provide independent tuning of the input and output. The first quasi-optical amplifier using this approach was a 25-element MESFET grid amplifier developed by Moonil Kim at Caltech [1]. Another grid amplifier, also developed by Moonil Kim, soon followed [2]. Unlike the first grid, this amplifier had a completely planar structure that makes the construction of the grid less complicated and more suitable

for monolithic fabrication. This 100-element Heterojunction Bipolar Transistor (HBT) grid amplifier had a gain of 10 dB, saturated output power of 450 mW, and noise figure of 7 dB at 10 GHz [2].

One of the shortcomings of this HBT grid was its relatively high noise figure and low output power. In an attempt to improve the noise and power performance, the use of HEMT devices in a grid amplifier was proposed. At microwave and millimeter-wave frequencies, HEMT's have the lowest noise figure of any amplifying solid-state device at room temperature. HEMT's using pseudomorphic

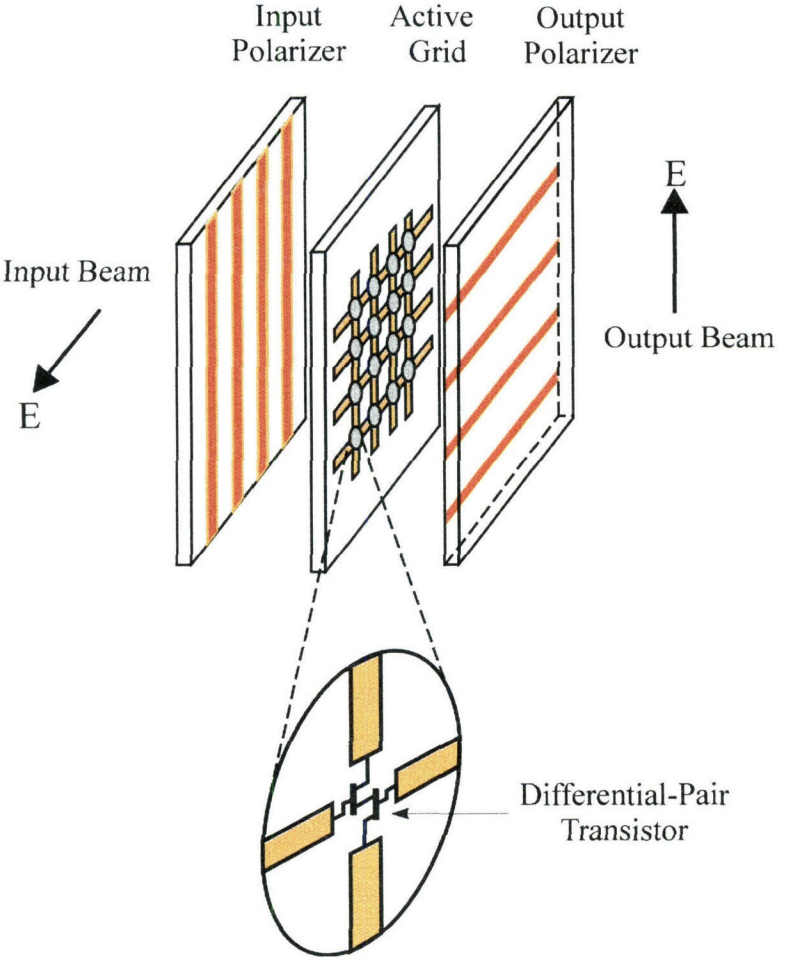

Figure 3.1. Perspective view of a grid amplifier. The input beam is horizontally polarized and is incident from the left. The vertically polarized output beam radiates to the right. The polarizers tune the input and output independently.

InGaAs material for the electron channels exhibit higher electron velocity than conventional GaAs channel HEMT's. This improves the power performance of these devices. HEMT's can also have a maximum frequency of oscillation (f_{max}) of few hundred GHz, making them desirable for fabrication of millimeter-wave grid amplifiers.

Differential-pair HEMT chips similar to the HBT chips used in the previous amplifier grid were designed by Moonil Kim at Caltech and Peter Smith at JPL. The chips for this work were fabricated at the Microdevices Laboratory (MDL) at JPL. This chapter discusses HEMT grid amplifiers using these devices. These grids are designed using a transmission-line equivalent model developed by Michael De Lisio and Cheh-Ming Liu at Caltech [3,4]. The measured gain is consistent with the predictions of the model.

More recently, a 10×10 hybrid pHEMT grid amplifier with 12 dB gain at 9 GHz was demonstrated [4]. This grid had a saturated output power of 3.7 W and a power-added efficiency of 12% at 9 GHz and a minimum noise figure of 3 dB at 10 GHz. Monolithic millimeter-wave quasi-optical arrays have also been developed. Slot-patch amplifier arrays using HBT's [5] and HEMT's [6] have been reported by Rockwell Science Center. Two millimeter-wave grid amplifiers have been demonstrated at Caltech. A 36-element HBT grid amplifier had a gain of 5 dB at 40 GHz, with saturated output power of 670 mW [7,8]. A 36-element pHEMT grid amplifier demonstrated gains from 6.5 dB at 44 GHz to 2.5 dB at 60 GHz [9].

3.2. GRID AMPLIFIER MODELLING

Fig. 3.2(a) shows a grid amplifier. The horizontal input passes through the input polarizer and air gap t_i and is amplified by the differential pair transistors in the active grid. This horizontal input also continues toward the output, passing through air gap t_o and the output polarizer. Fig. 3.2(b) is the transmission-line equivalent model for this grid [4,10]. The top portion of Fig. 3.2(b) represents

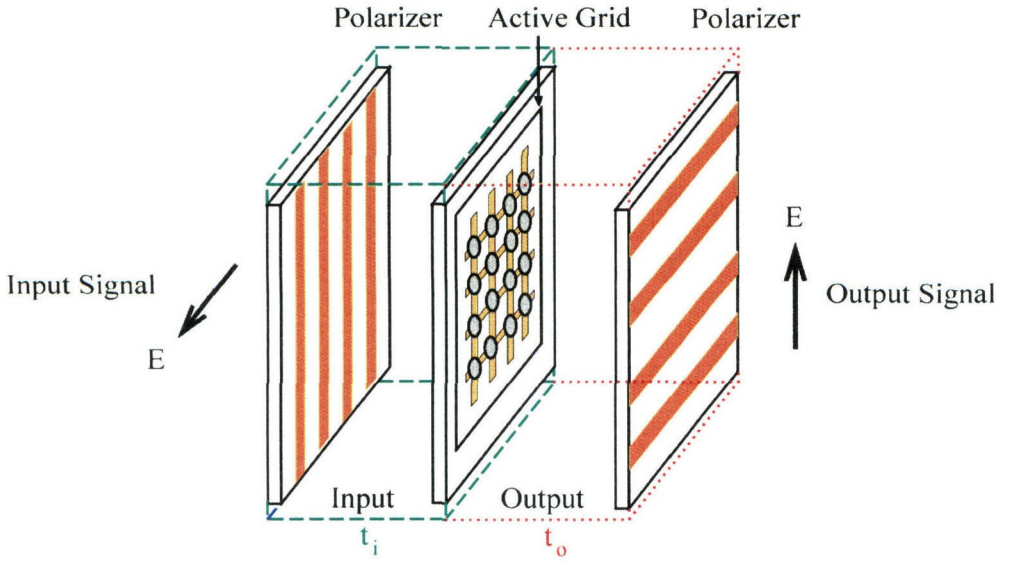

(a)

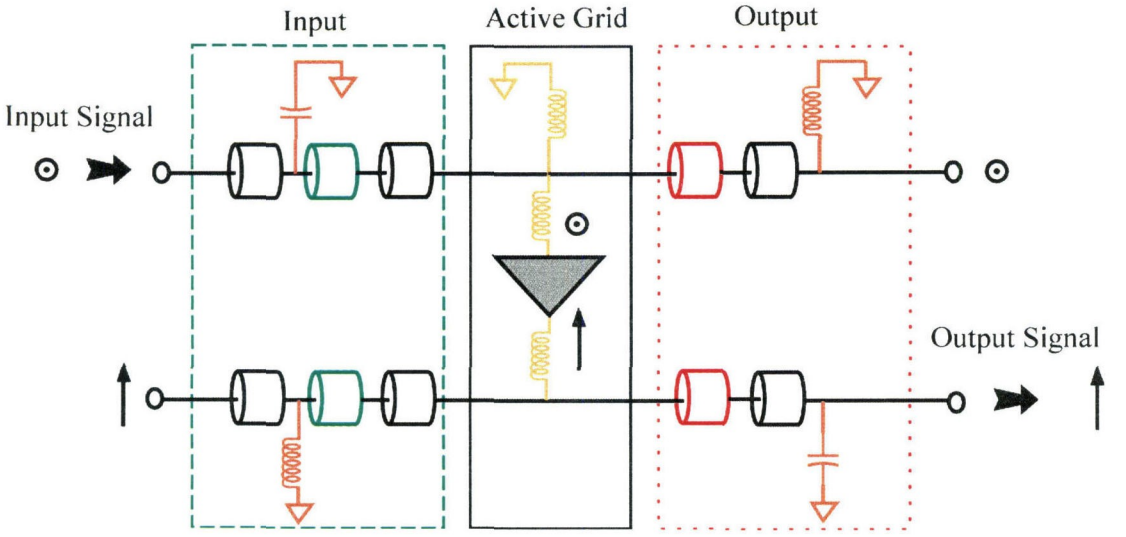

(b)

Figure 3.2. (a) Perspective view of a grid amplifier. It consists of the input polarizer, an active grid, and the output polarizer. The horizontally polarized input beam passes through the input polarizer and air gap t_i and gets amplified by the differential pair transistors in the active grid. The vertically polarized output beam is transmitted to the right. The polarizers tune the input and output independently. (b) Transmission-line equivalent circuit.

the path for the horizontal beam. As discussed in Section 1.2, the unit cell determines the driving-point impedances seen by the devices, while the power scales with the grid area. This allows one to analyze the grid by analyzing the unit cell and independently select the total grid size to meet the power requirement. The air gaps and substrates are represented by transmission lines in Fig. 3.2(b). For a square unit cell the characteristic impedance of the transmission lines representing free space is $\eta_o = 377\,\Omega$ and the characteristic impedance of the substrates is $\eta_o/\sqrt{\epsilon_r}$, where ϵ_r is the relative dielectric constant of the substrate. The metallic part of the polarizers are modelled as inductors or capacitors depending on the polarization of the beam. For a horizontal polarization, the input polarizer is represented as a capacitor. For the same polarization, the output polarizer is modelled as an inductor. The bottom portion of Fig. 3.2(b) is for vertical polarization. The top and bottom portions are linked to each other by the unit cell.

Fig. 3.3 shows the unit cell of the grid amplifier. The gates of a differential-pair transistor chip are connected to the horizontal leads, and the drains to the vertical leads. The meandering lines are for biasing. Meandering lines are used to present a high impedance to the input beam. The input and output leads are presented as inductors in the transmission-line equivalent circuit. The meandering bias lines are mainly horizontal therefore they primarily affect the input and are represented as an inductor. The numeric values for the inductors and capacitors in Fig. 3.2(b) are computed using method of moments [10].

Using this transmission-line equivalent model, two X-band HEMT grid amplifiers were designed and constructed. The remainder of this chapter details the design, construction and measurements for each grid. The active devices for both grids were HEMT's provided by Dr. Peter Smith at JPL.

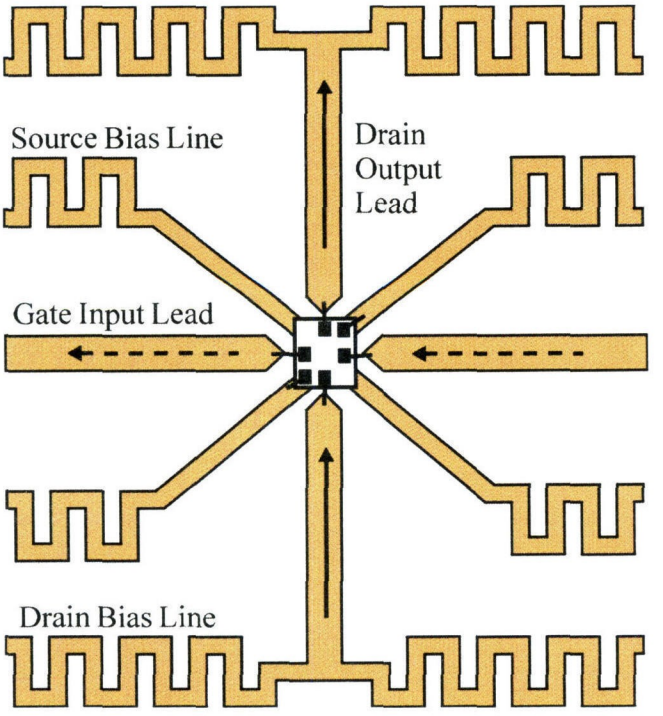

Figure 3.3. Grid amplifier unit cell. The inputs are the horizontal leads, and the outputs are the vertical leads. Arrows indicate the RF currents.

3.3. FIRST GRID

3.3.1. DESIGN

Pseudomorphic InGaAs/AlGaAs HEMT material with approximately $2 \times 10^{12} \mathrm{cm}^{-2}$ sheet carrier concentration was used for the differential-pair devices. Gates were defined with an electron beam lithography system and a tri-layer resist. These HEMT's have 0.25-μm gates with finger widths of 75 μm. The gate metalization consists of 300 Å of Ti, 300 Å of Pt, and 4000 Å of Au. Devices were passivated with 1200 Å of Silicon Nitride deposited in a low temperature ECR plasma deposition system. Air bridges were formed with gold on titanium.

Fig. 3.4 shows the differential-pair chip layout and its equivalent circuit used in the first grid. The 5-kΩ resistor and the 0.3-pF capacitor between gate and drain are to present negative feedback between the input and the output. This is

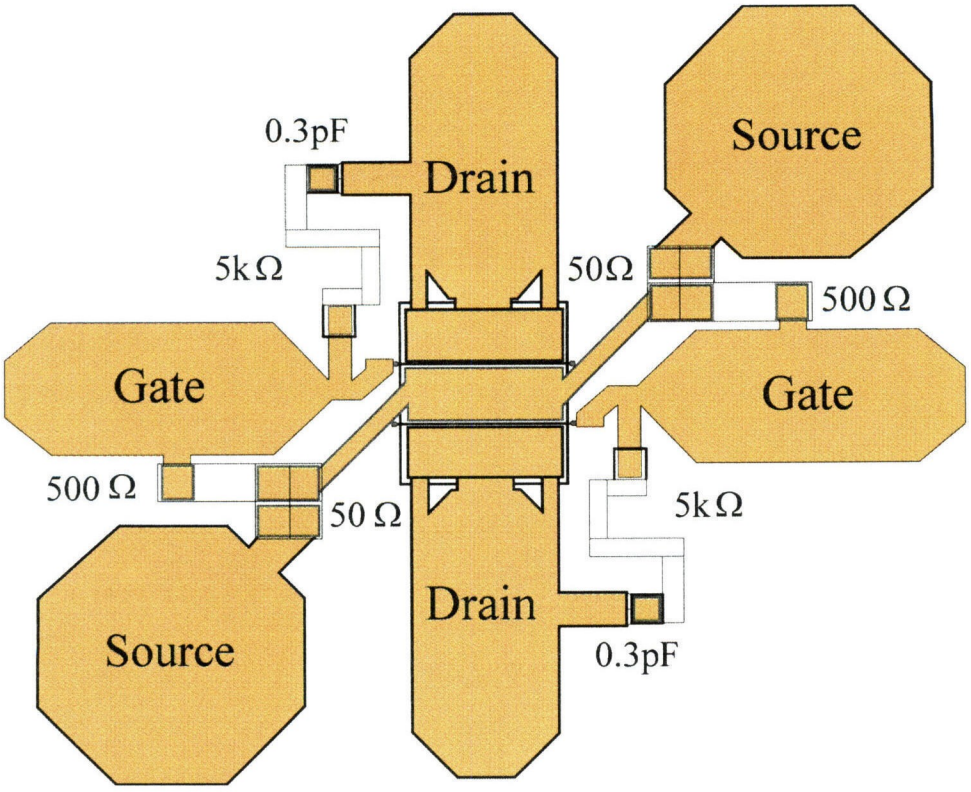

(a)

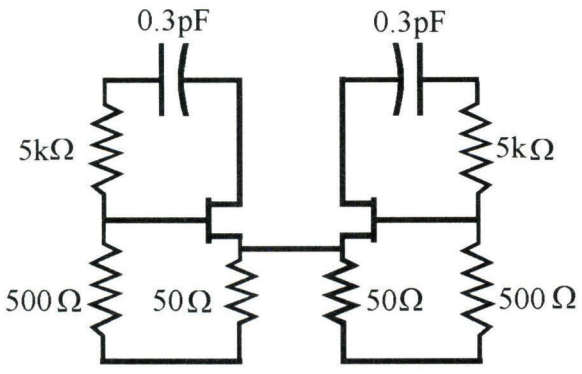

(b)

Figure 3.4. (a) HEMT differential-chip layout. (b) Equivalent circuit for the chip.

to help stabilize the grid at X-band. The 50-Ω resistor is to increase the common-mode rejection ratio and insure that the grid is operating in the differential mode, and the 500-Ω resistor is to self-bias the gate. Fig. 3.5 shows a picture of this chip taken under a microscope.

Fig. 3.6 shows the Maximum Stable Gain (MSG) for the HEMT, and the Maximum Available Gain (MAG) for the differential-pair chip. The maximum operating power gain for a transistor when it is potentially-unstable is called maximum stable gain. Maximum available gain is the operating power gain for a stable transistor [11,12]. The MSG for the HEMT is 16 dB at 10 GHz. Addition of the negative feedback and the self bias resistor decreases the gain of the chip. Therefore the MAG for the chip with feedback and self bias resistor is less than the MSG of the transistor. The chip MAG is 10 dB at 10 GHz.

Based on the equivalent circuit discussed in the previous section, an X-band grid amplifier was designed. The unit cell is shown in Fig. 3.7. Bond wires are used to connect the gates of the chip to the horizontal input leads, and the

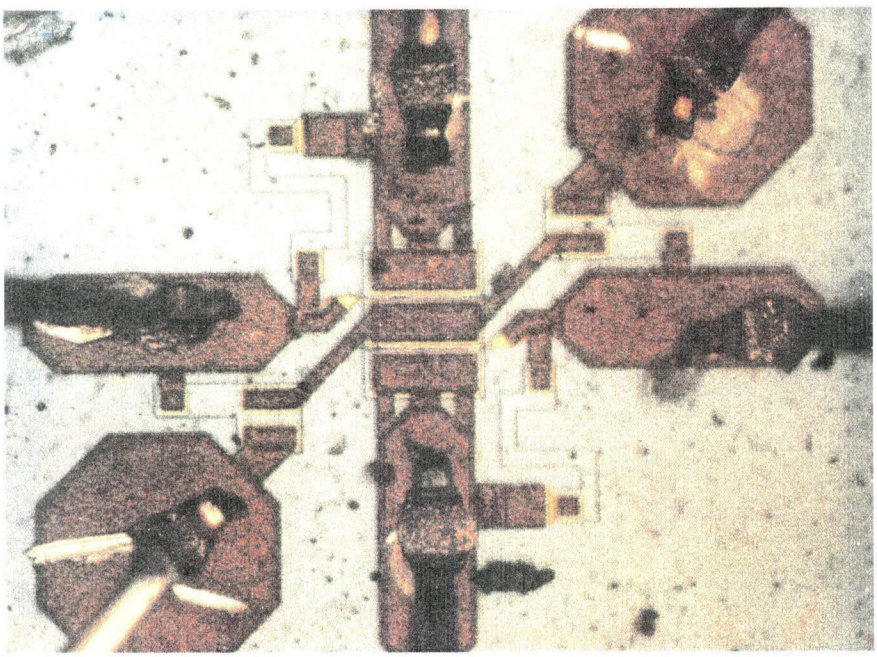

Figure 3.5. A photograph of the differential-pair chip under a microscope.

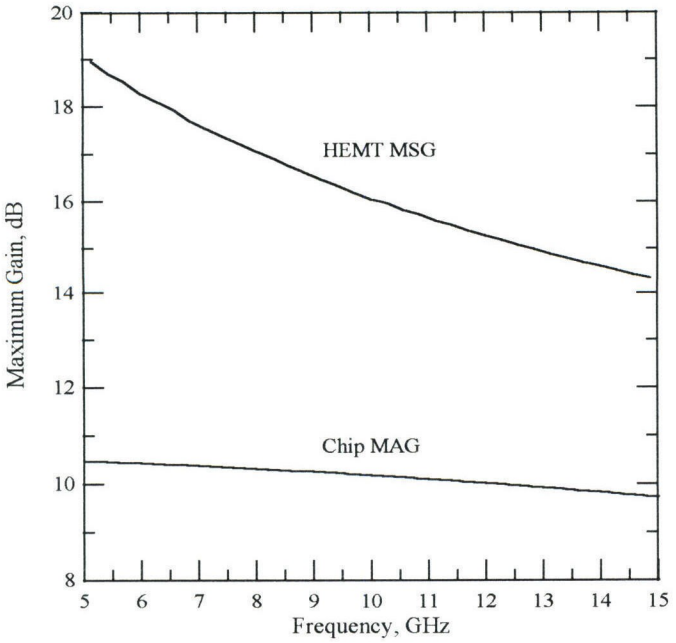

Figure 3.6. Maximum stable gain of the HEMT, and maximum available gain of the chip.

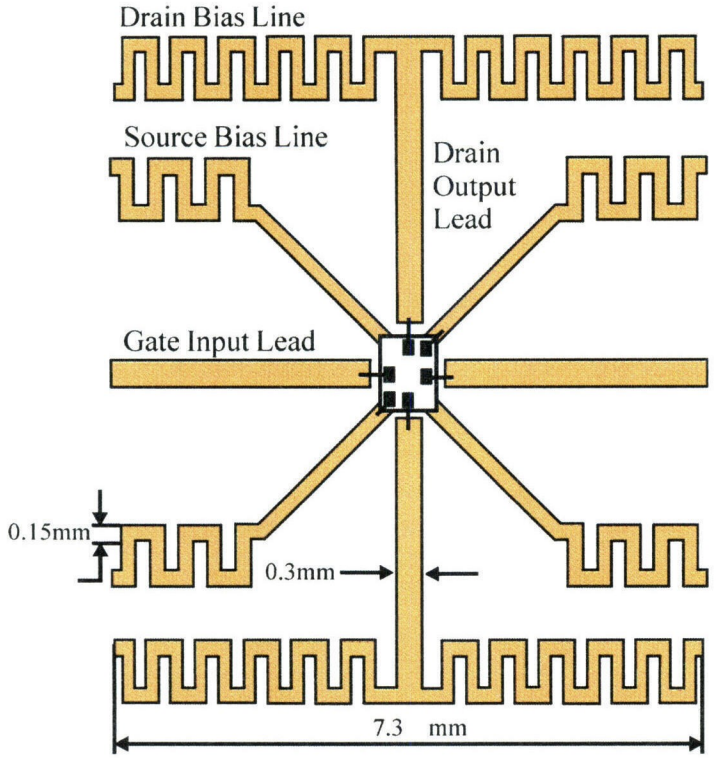

Figure 3.7. The unit cell of the grid amplifier. The gates of the differential-pair chip are connected to the horizontal input leads, and the drains to vertical output leads.

drains of the chip to the vertical output leads. The drains in each row are biased through the meandering lines at the top and bottom of the unit cell. The sources are biased through the source bias meandering lines (Fig. 3.7). The unit cell is 7.3 mm on each side. The input and output leads are 0.3-mm wide, and the width of the meandering bias lines are 0.15 mm. Pictures of the grid are shown in Figs. 3.8 and 3.9. A Duroid substrate with copper cladding is used to etch the metal pattern. The copper is gold plated to facilitate wire bonding to the surface. The devices are attached to the substrate using epoxy, and wire bonds are used to make the connections.

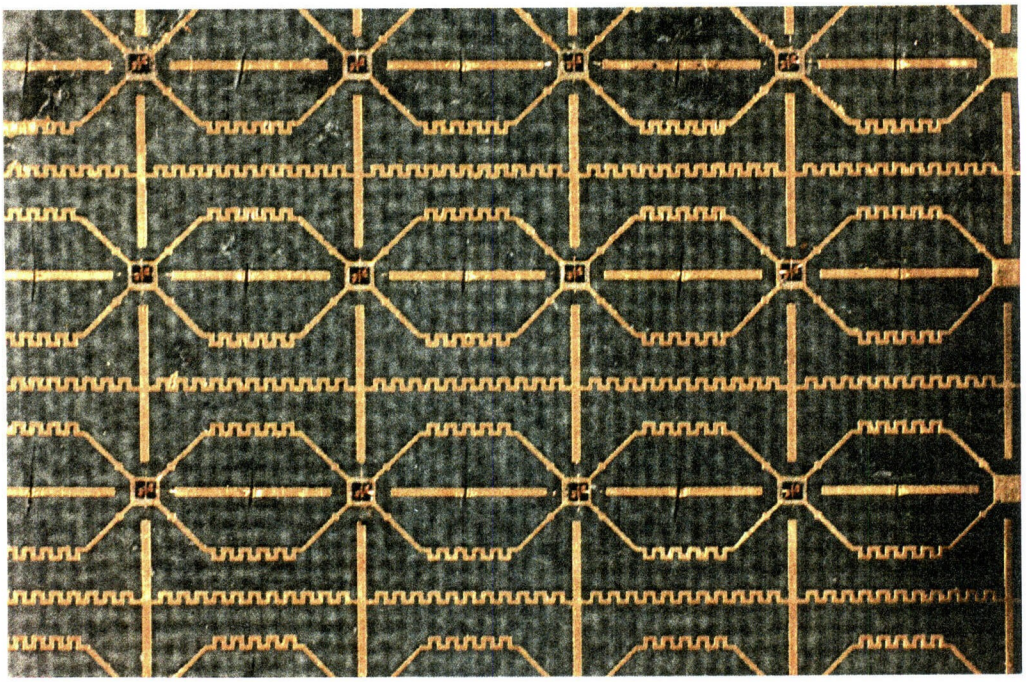

Figure 3.8. Picture of a portion of the grid amplifier.

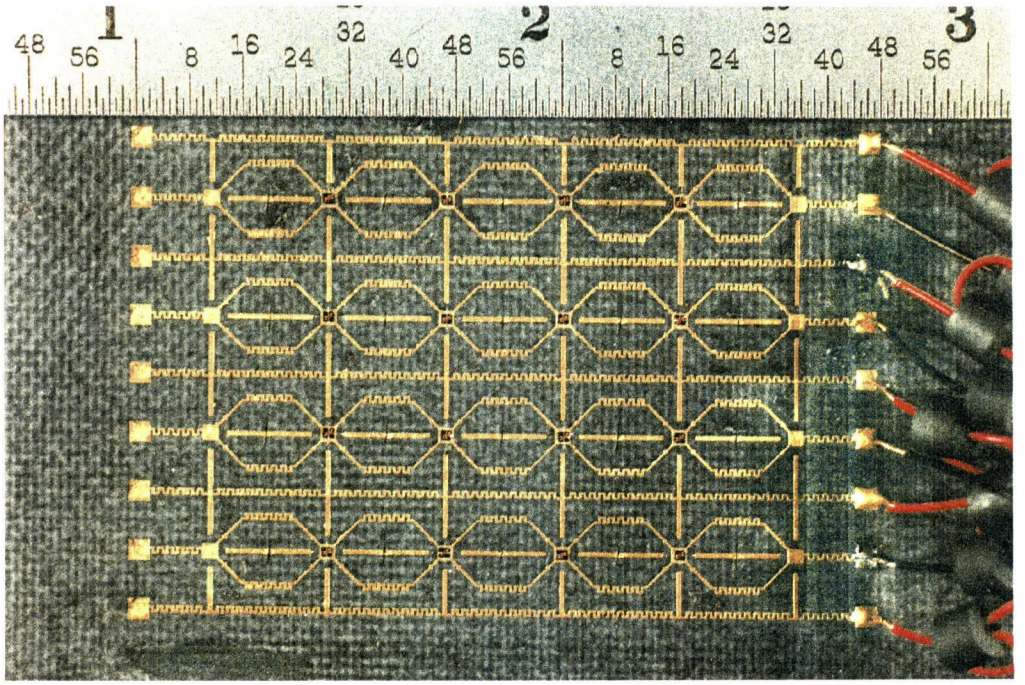

Figure 3.9. Picture of the entire grid amplifier.

3.3.2. GAIN MEASUREMENT

Fig. 3.10 shows how the gain is measured. First the two horns are co-polarized and the system is calibrated. A signal generator transmits a vertically polarized beam from the input horn. P_c is the calibrated power measured at the output using the configuration shown in Fig. 3.10(a). Then the grid is placed in between two cross-polarized horns, Fig. 3.10(b). The signal generator transmits a beam that is horizontally polarized. This beam is incident to the grid. The output horn receives the vertically polarized output beam from the grid. The

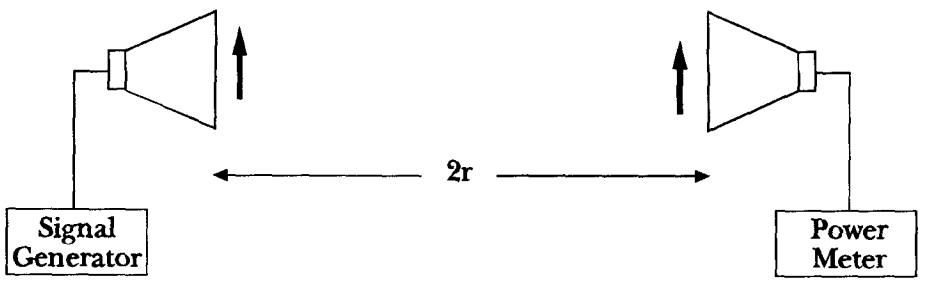

(a)

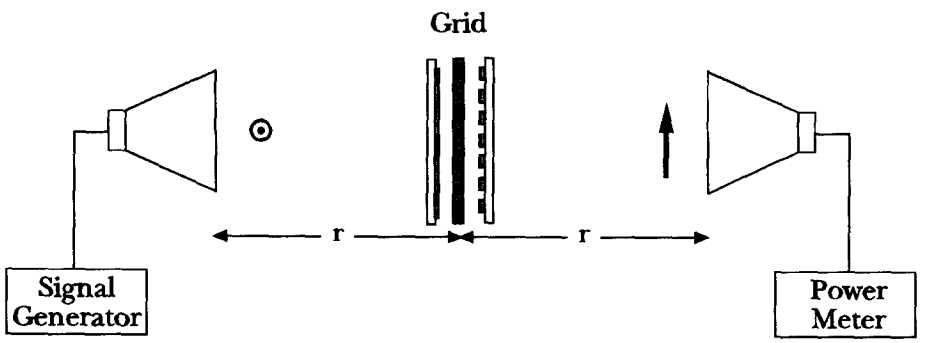

(b)

Figure 3.10. Amplifier gain measurement setup. (a) Calibration measurement without the grid. The horns are co-polarized. (b) Measuring the gain with the grid in place. The horns are cross-polarized.

signal P_r is measured by a power meter. The gain G is defined by the equation:

$$G = \frac{P_r}{P_c}\left(\frac{\lambda r}{2A}\right)^2, \tag{3.1}$$

where P_r is the received power from the second measurement (Fig. 3.10(b)), P_c is the calibrated power from the first measurement (Fig. 3.10(a)), λ is the free-space wavelength, r is the spacing between the horn and the grid, and A is the physical area of the grid [13].

Fig. 3.11 shows the actual setup used to do the gain measurement for the grid. The setup is computer-controlled. The input is generated from a 8350B sweeper, and the output is measured with a HP8592A spectrum analyzer. A HP437B power meter monitors the output power of the sweeper through a 10 dB directional coupler. The software for this setup was developed by Cheh-Ming Liu, at Caltech.

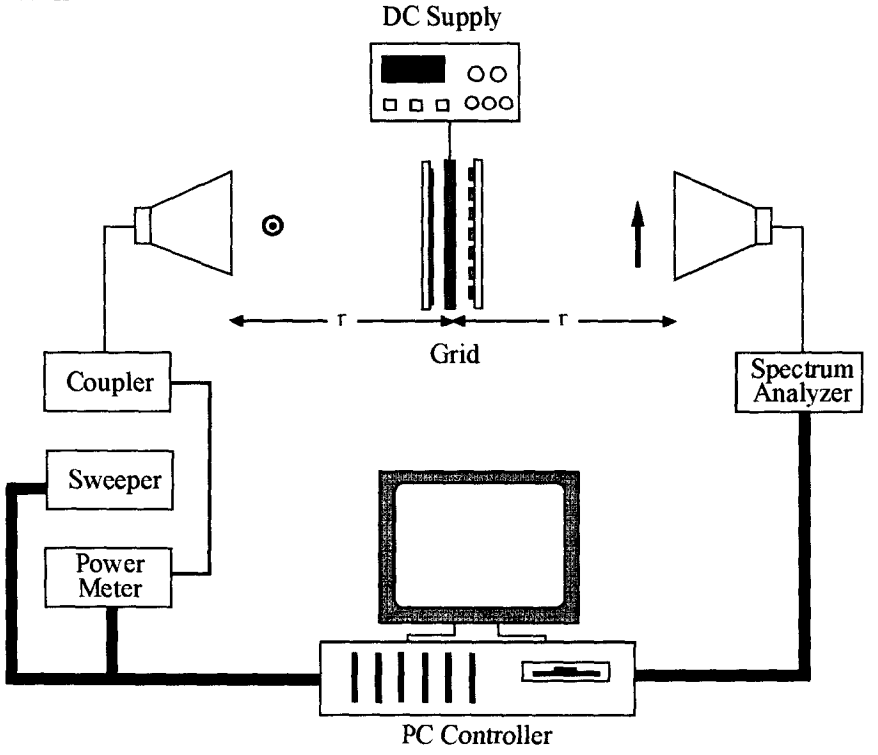

Figure 3.11. Gain measurement setup for the grid amplifier.

Fig. 3.12(a) shows the assembled grid amplifier. The active grid and both polarizers are built on Duroid substrates with a relative dielectric constant of 2.2. The input and output tuners are also Duroid slabs with a relative dielectric constant of 2.2. These tuners are used to improve the input and output impedance matching and thereby increase the gain. Fig. 3.12(b) is the transmission-line equivalent circuit model for the grid assembly at 10 GHz. Since half of a unit cell is modelled the characteristic impedance of free space appears as 189 Ω instead of 377 Ω. The dielectric substrates and the free space between them are modelled as transmission lines with characteristic impedance of $189/\sqrt{2.2} = 127\,\Omega$ for the substrates and 189 Ω for free space. The electric lengths of these transmission lines represent the thicknesses of the substrates or the spacing between them. Depending on polarization, the polarizers are modelled as inductors or capacitors. For the horizontal polarization, the input polarizer appears as a capacitor with reactance of 530 Ω. For the vertical polarization, the same polarizer appears as an inductor with reactance of 20 Ω. Since the output polarizer is identical to the input polarizer the same values also apply to the output polarizer. The input and output leads in the unit cell of the active grid are shown as 100-Ω inductors. The triangle represents half of the HEMT chip in a unit cell. The 40-Ω inductor in the model represents the bias lines [10].

Fig. 3.13 shows the measured gain of the grid. The grid is biased at 3 V and a total drain current of 90 mA. It has a maximum gain of 7 dB at 10 GHz with a 3-dB bandwidth of 800 MHz, which corresponds to 8%. The theory for the gain using the transmission-line equivalent model is also shown. The measured gain agrees well with the theory at low frequencies. At higher frequencies theory predicts more gain. This might be due to the inaccurate modelling of the HEMT's, that predicts higher gain for the devices at frequencies above 10 GHz. To insure that the grid is working properly the gain of the grid with no bias is also measured. This gain is always below –3 dB.

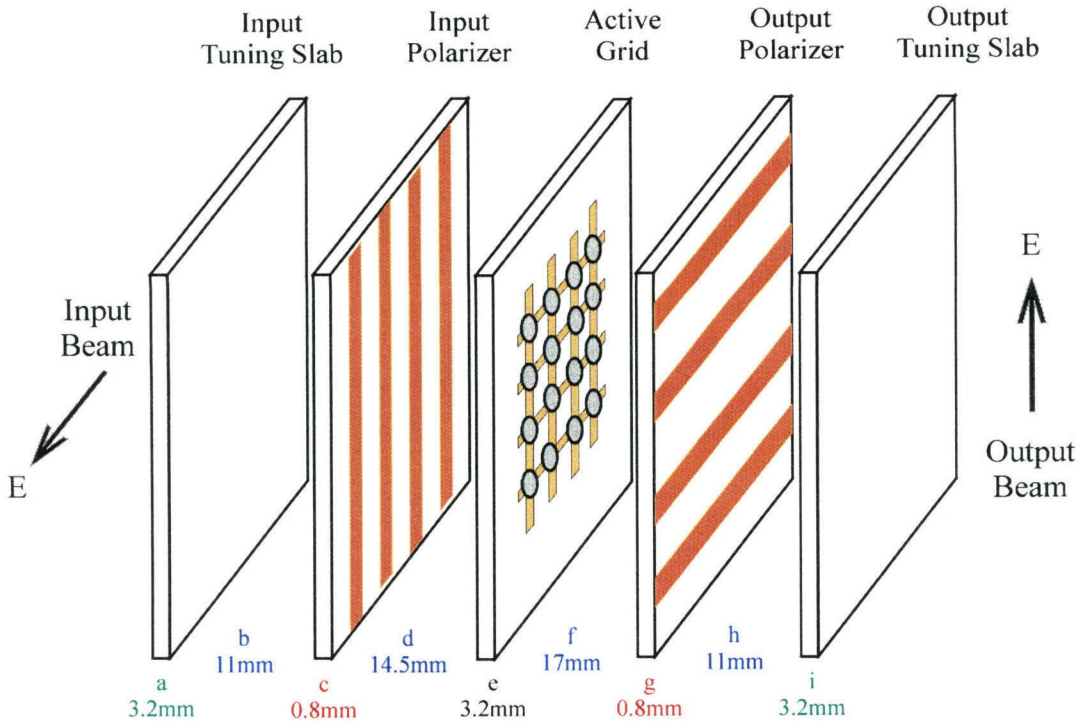

(a)

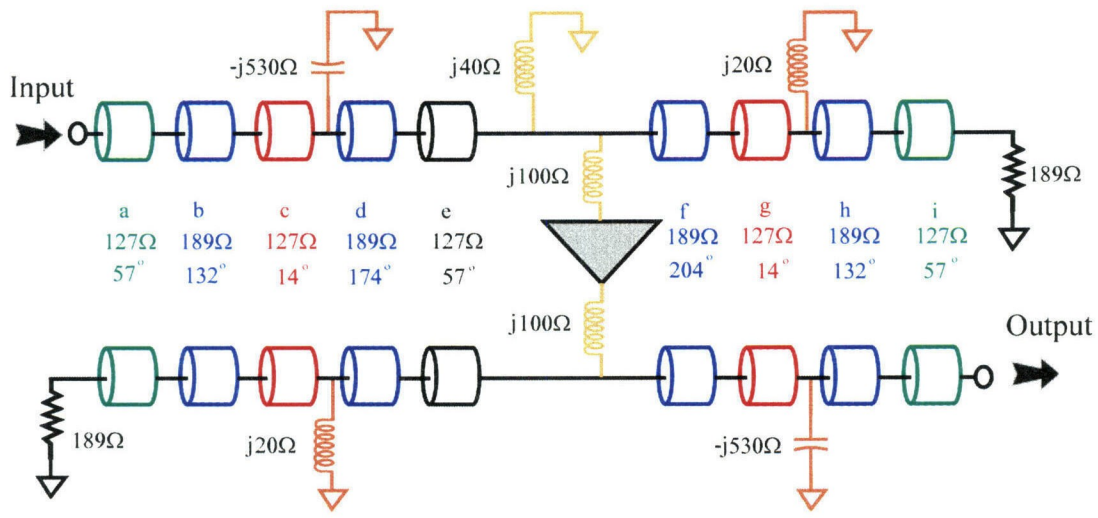

(b)

Figure 3.12. (a) The assembled HEMT grid amplifier. (b) The 10 GHz transmission-line equivalent circuit model.

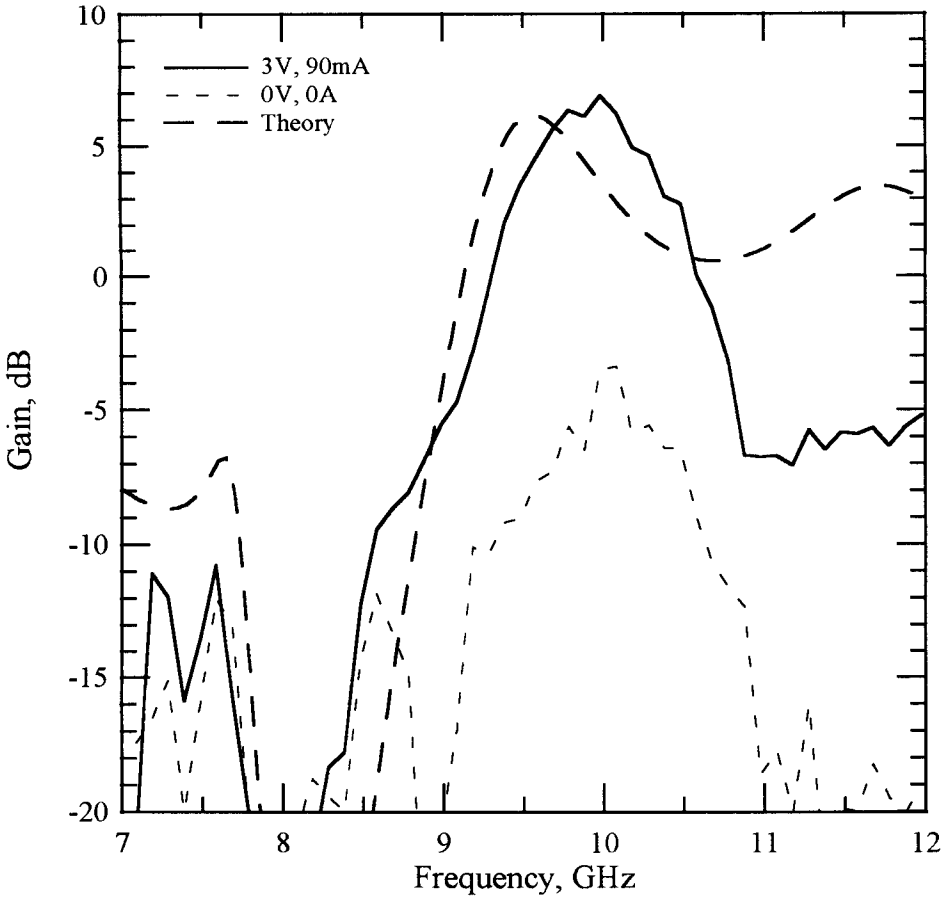

Figure 3.13. Gain response of the grid amplifier.

3.4. SECOND GRID

A second grid was designed and fabricated using a new batch of differential-pair HEMT chips also provided by Dr. Peter Smith at JPL. The gates of the HEMT chips used in the first grid were self-biased. The design of the chips for the second grid were altered so that the gates can be biased directly.

3.4.1. DESIGN

The fabrication process used for these HEMT's are very similar to the first grid (Section 3.3.1). The HEMT's used for this chip have 0.15-μm gates with a finger width of 75 μm. Fig. 3.14 shows the layout and the equivalent circuit for

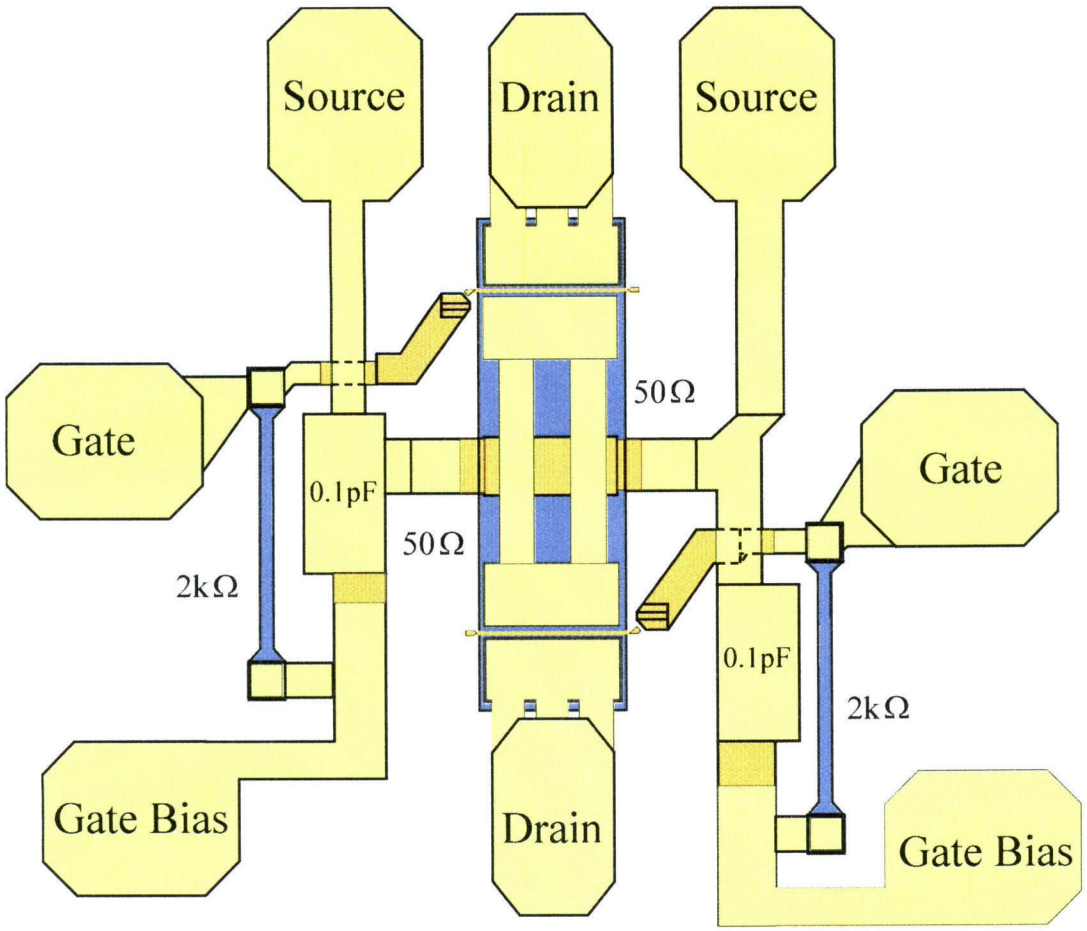

(a)

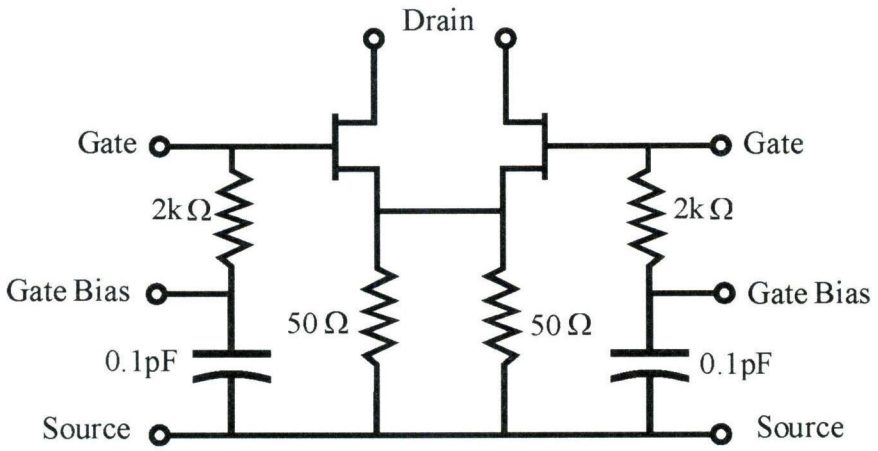

(b)

Figure 3.14. (a) HEMT differential-pair chip layout. (b) Equivalent circuit for the chip.

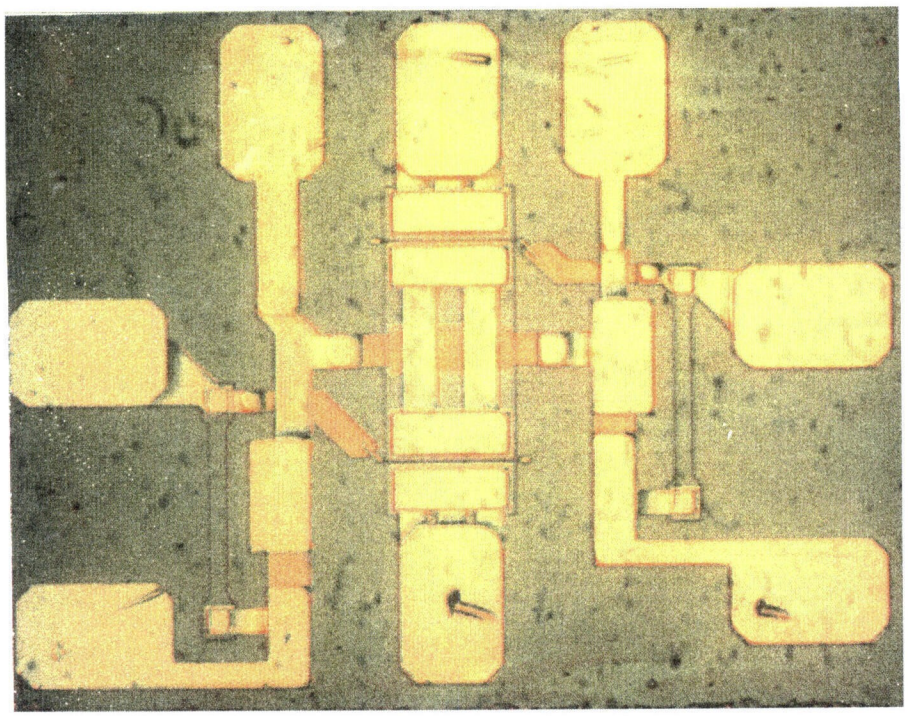

Figure 3.15. Photograph of the differential-pair chip taken under a microscope.

the new differential-pair HEMT chips. The RF inputs to the gates are separated from the bias inputs to the gates by 2-kΩ resistors. The bias inputs to the sources are isolated from the gate bias inputs by 0.1-pF capacitors. The 50-Ω resistors increase the common-mode rejection ratio of the differential-pair and insure that the grid is operating in the differential mode. Fig. 3.15 shows a photograph of the chip.

Measured current-voltage relations of a typical chip is shown in Fig. 3.16. This measurement is done using a HP4145A semiconductor parameter analyzer. The theoretical maximum stable gain of the HEMT chip is shown in Fig. 3.17. The MSG for the chip is 15 dB at 10 GHz.

The unit cell of the grid amplifier is shown in Fig. 3.18. In order to bias the gates, the unit-cell design is changed from the previous grid. Similar to the grid discussed earlier, the outer top and bottom meandering lines provide the drain

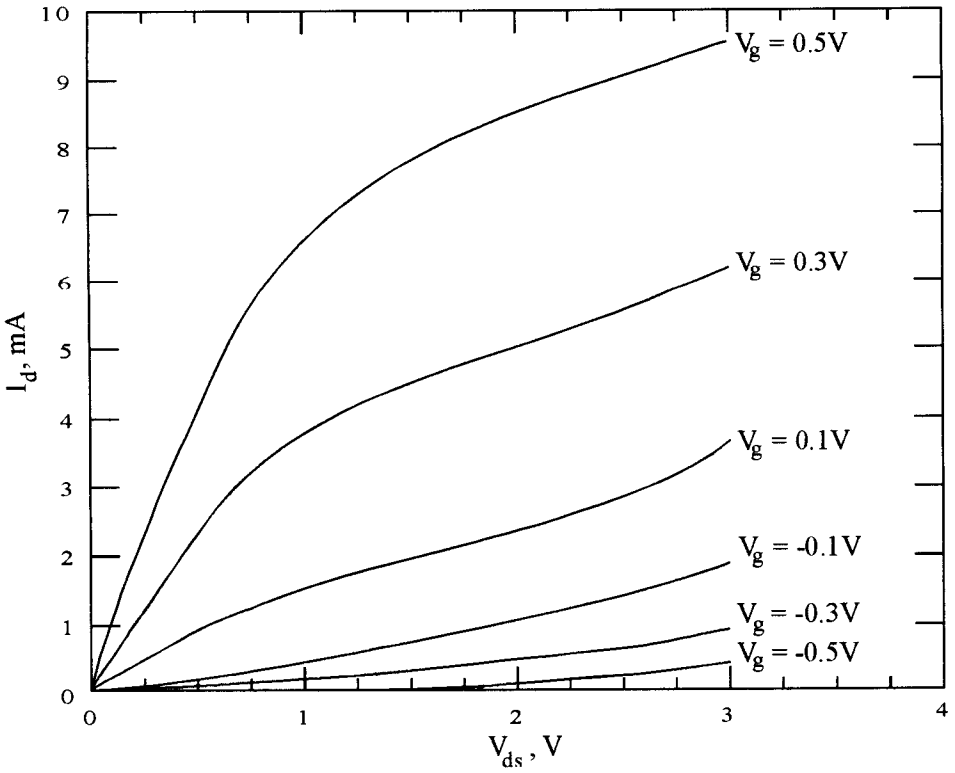

Figure 3.16. Measured drain current versus drain-source voltage for gate voltages of −0.5 V to 0.5 V, in steps of 0.2 V.

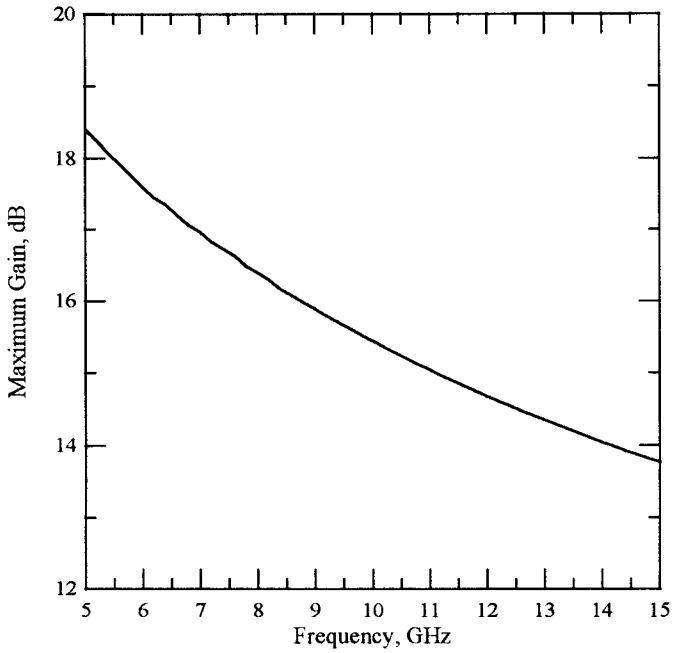

Figure 3.17. Maximum stable gain of the differential-pair chip.

bias. Unlike the previous design, the top and bottom inner meandering lines are not connected. The top inner bias line is used to bias the gate and the bottom line is for biasing the source. The unit cell size is 7.3 mm on each side. The input and output antennas are 0.45-mm thick, and the width of the meandering lines are 0.15 mm. The 20-Ω resistors at the end of the input antennas are to suppress oscillations, and will be discussed in Section 3.4.2.

3.4.2. STABILITY

A grid using the unit-cell design of Fig. 3.18 was fabricated on a 15-mil Duroid substrate with a relative dielectric constant of 2.2. The fabrication process is similar to the first grid. The Duroid substrate was then placed on top of a 3.2-mm-thick substrate with the same dielectric constant. The grid was originally fabricated with no oscillation suppressing resistors. Fig. 3.19 and Fig. 3.20

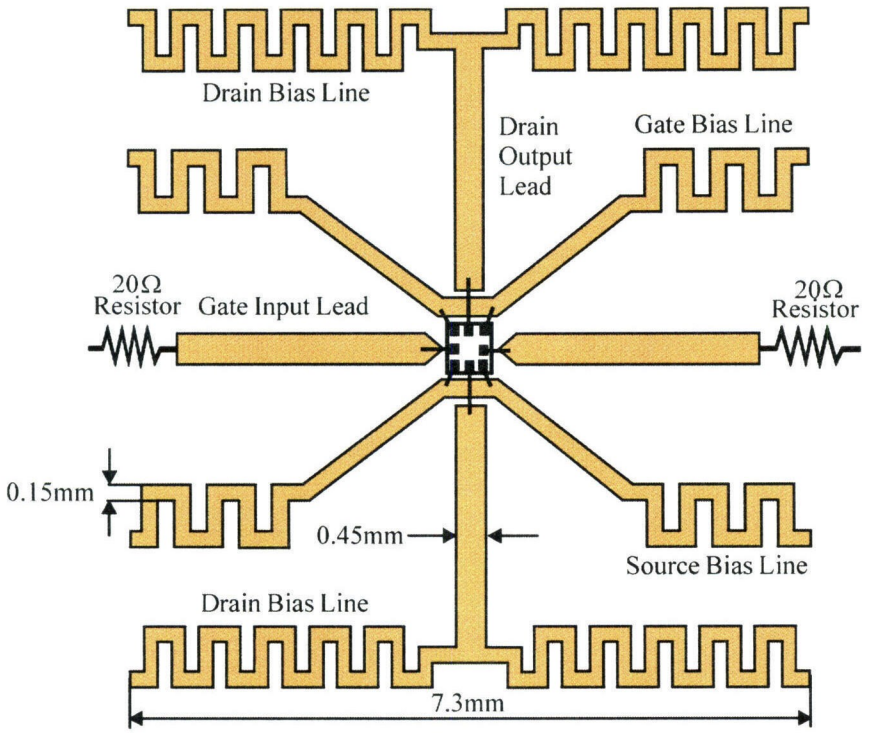

Figure 3.18. Unit cell of the grid amplifier. The gates and sources are biased through the inner meandering lines. The drains are biased through the outer meandering lines.

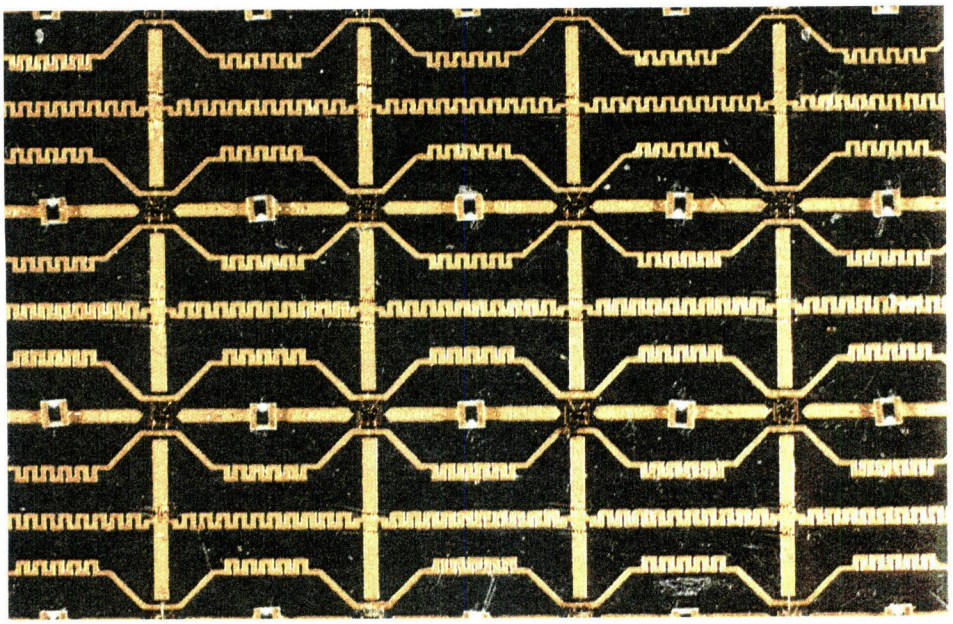

Figure 3.19. Photograph of a few unit cells of the grid.

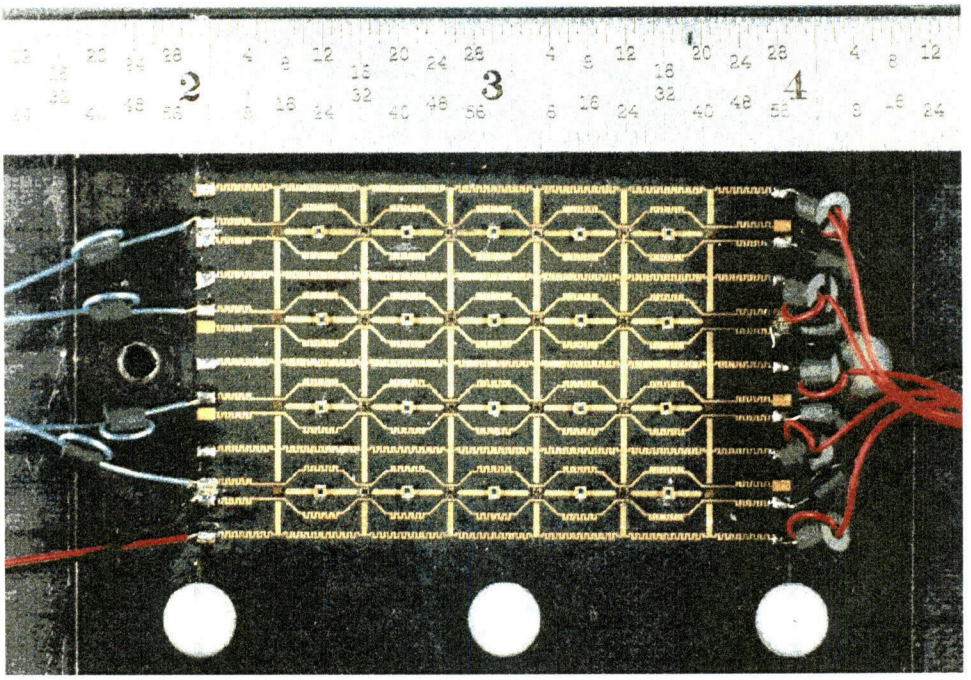

Figure 3.20. Photograph of the entire grid.

show pictures of this grid. The photographs were taken after the oscillation suppressing resistors were attached. These resistors are clearly visible halfway between two chips on the input leads of the grid (Figs. 3.19 and 3.20). The wires on the left hand side of the grid provide the bias for the gates. The sources and drains are biased through wires connected to the right side of the substrate. The thickness and dielectric constant of the substrate was chosen to maximize the gain of the amplifier.

The grid originally suffered from oscillations around 9–10 GHz. The oscillation occurred at currents of less than 5 mA per device. This is much lower than the maximum gain current for the device. The oscillation was independent of the polarizer position, and thickness of the grid substrate. A model for this oscillation was developed by Cheh-Ming Liu at Caltech [14,15]. By measuring the far field patterns of this oscillation for different polarizations it was concluded that the oscillation is a common-mode one. Fig. 3.21 shows the current distribution for this oscillation for part of a grid. Due to the symmetry of this distribution we can use a quarter of a unit cell for the analysis of the oscillation. Fig. 3.22(a) shows the quarter cell and Fig. 3.22(b) is the equivalent circuit model for this quarter cell. According to Martinez-Compton theory [16], a circuit is potentially unstable if the circular function has a phase of zero when the magnitude of the circular function exceeds unity. The frequency where this occurs is the frequency where the circuit is potentially unstable. To measure the circular function a circulator is inserted in the equivalent circuit of Fig. 3.22.

The 50-Ω source resistors were originally placed in the chip to suppress common-mode oscillations. However, the model for the common-mode oscillation predicts that these resistors might actually be contributing to the instability of the grid. According to this theory, shorting these resistors will suppress the oscillation. In order to investigate this, the 50-Ω resistors in the chip were shorted using bond wires. Fig. 3.23 shows a picture of the chip with a bond wire shorting

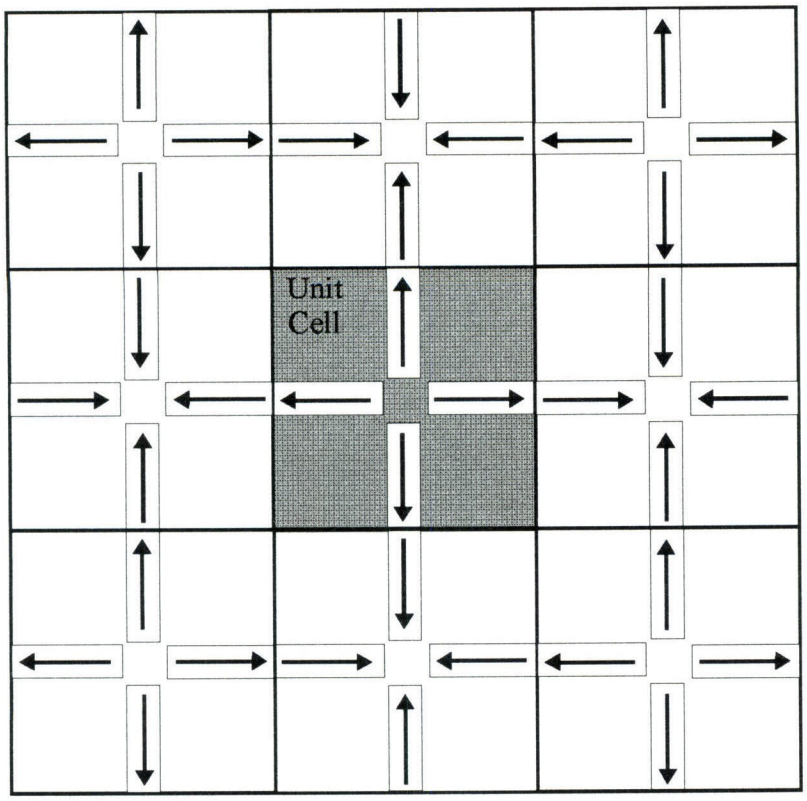

Figure 3.21. Current distribution for the common-mode oscillation for part of a grid.

the 50-Ω resistors. This approach reduced the output power of the oscillation by about 10 dB but it did not totally suppress it. Furthermore, instead of one frequency the grid began oscillating at 8.7 GHz, 9.3 GHz, and 11.5 GHz frequencies. If we assume that the bond wire is not a perfect short and that we have a small resistance in the source we can then predict these new oscillations using current distributions in Fig. 3.24(a) for 8.7-GHz oscillation and Fig. 3.25(a) for 11.5-GHz oscillation. Due to the symmetry of these current distributions we can use the quarter of the unit cell and the equivalent circuits in Figs. 24(b) and 3.25(b) to model the oscillations. The 9.3 GHz oscillation has a current distribution similar to Fig. 3.21 with an equivalent circuit shown in Fig. 3.22. It is also possible that using a wire bonder to short the 50-Ω resistors damaged the chip and changed its behavior in an unknown way. To test this idea for future grids, fabrication of

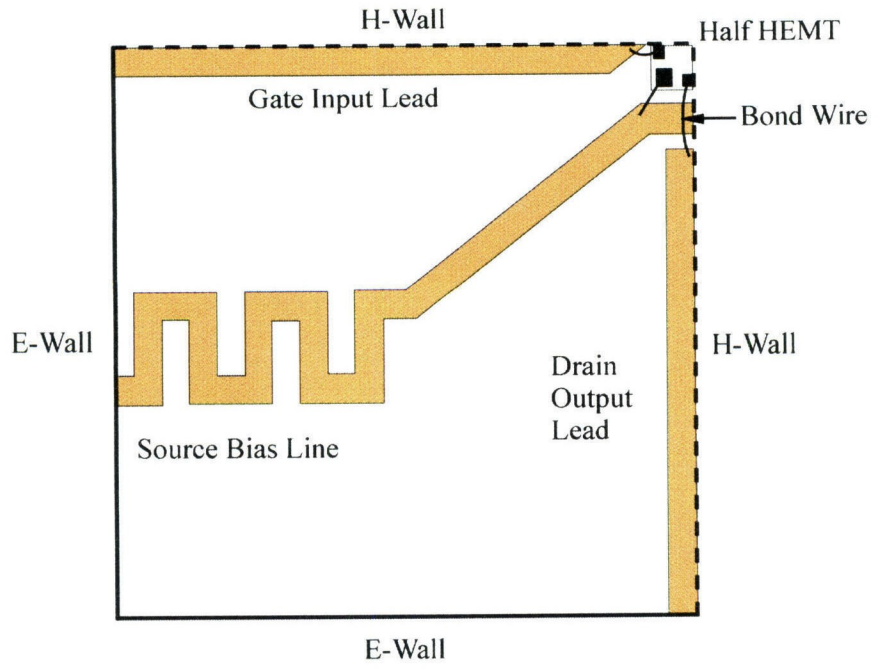

(a)

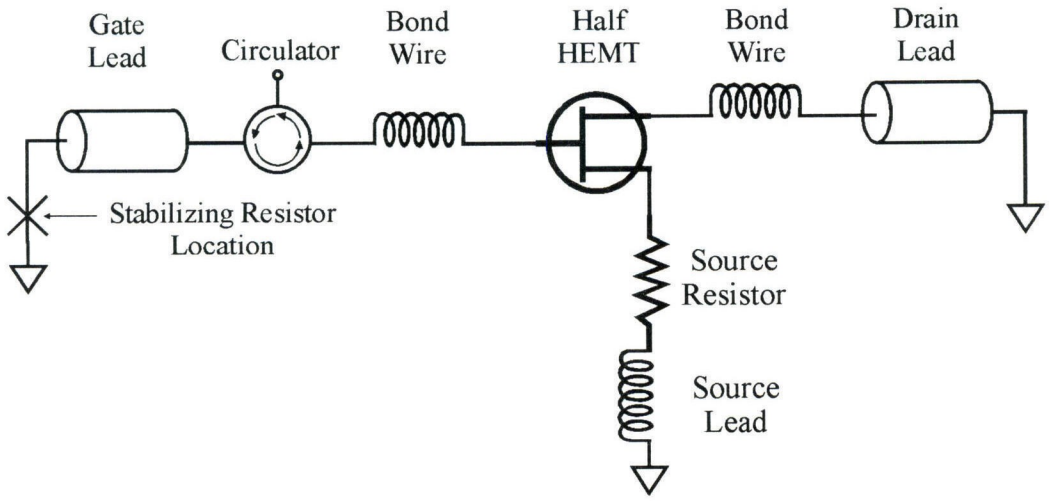

(b)

Figure 3.22. (a) Quarter cell. Due to the symmetry of the current distribution and the imposed boundary conditions by it a quarter cell can be used to model the oscillation. (b) The equivalent circuit for the common-mode oscillation.

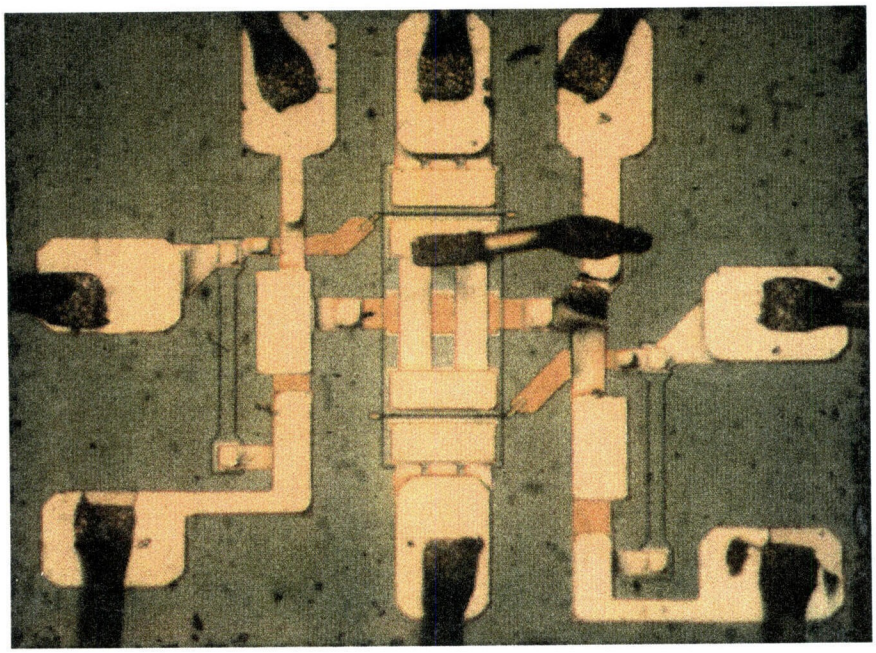

Figure 3.23. Picture of a differential-pair chip with bond wire shorting the 50 Ω source resistor.

chips without the common-mode suppressing resistors is suggested. This could not only result in a stable grid, but it could also increase the efficiency of the grid.

Next, to stabilize the grid, we tried adding 20-Ω resistors at the end of the input radiating leads in a unit cell, halfway between two transistors. Fig. 3.26 is the circular function for the circuit in Fig. 3.22 assuming a source resistance of 5 Ω for the quarter cell, with and without the gate oscillation suppressing resistors. Without these resistors the circular function predicts an oscillation frequency of 9.3 GHz which is equal to the observed oscillation frequency. The circular function with these 20-Ω resistors is inside the unit circle, indicating that the grid is stable. The same resistors also suppress the 8.7 and 11.5-GHz oscillations modelled by equivalent circuits in Fig. 3.24(b) and Fig. 3.25(b). These resistors are visible in Fig. 3.19 and Fig. 3.20.

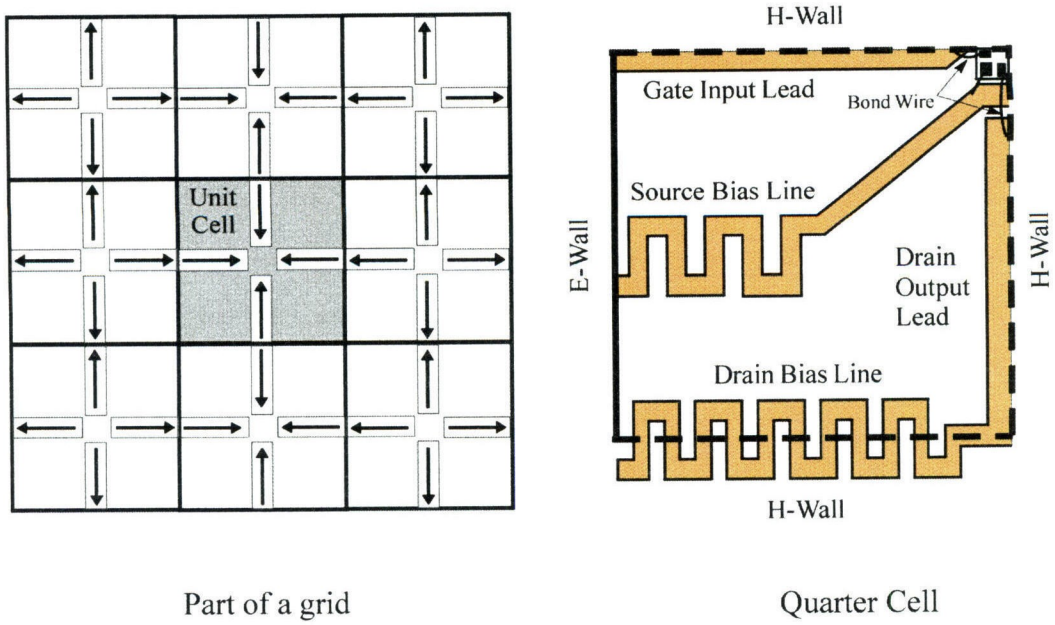

(a)

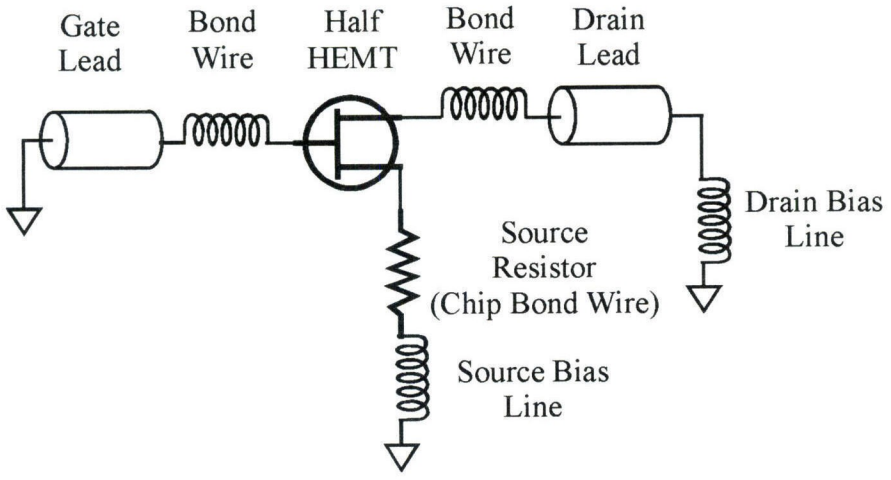

(b)

Figure 3.24. (a) Current distribution for part of a grid and the quarter cell for the 8.7 GHz oscillation. (b) The equivalent circuit.

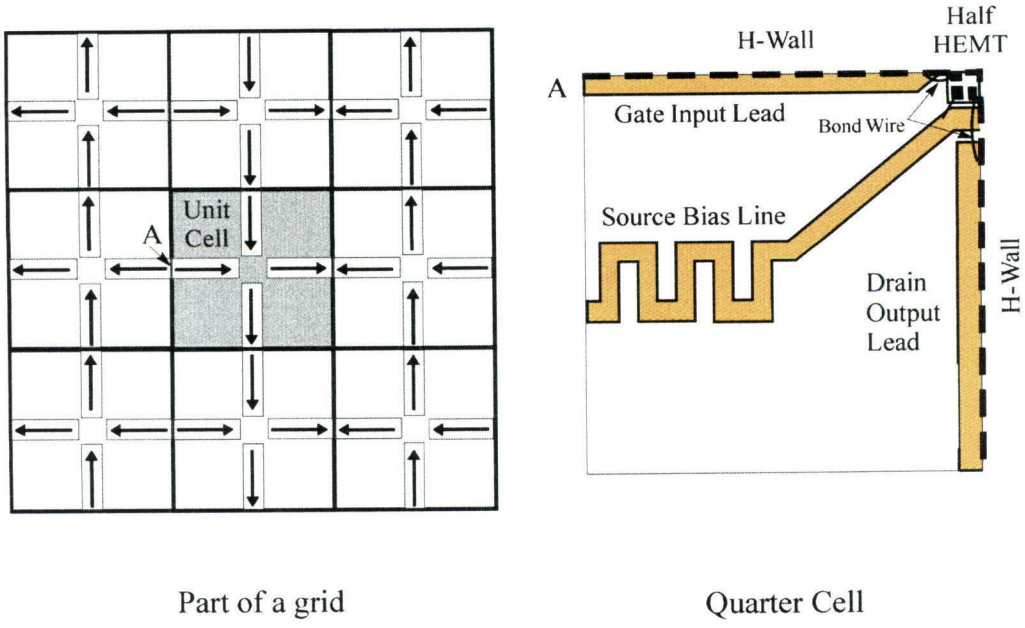

(a)

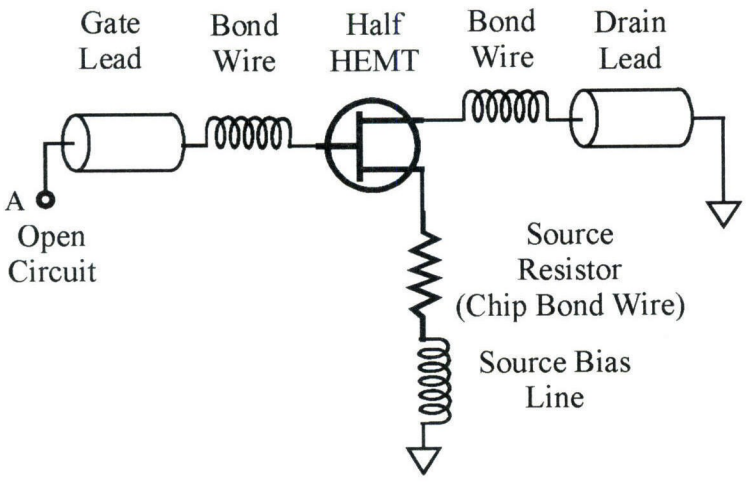

(b)

Figure 3.25. (a) Current distribution for part of a grid and the quarter cell for the 11.5 GHz oscillation. (b) The equivalent circuit.

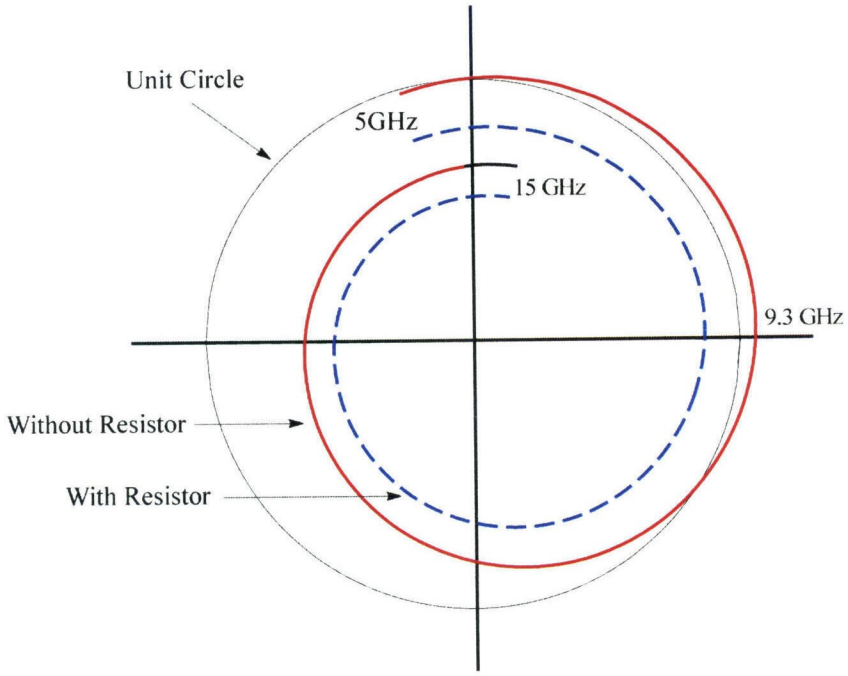

Figure 3.26. The grid circular function for the common-mode oscillation modelled in Fig. 3.22 with and without the oscillation suppressing resistors. Without these resistors the grid is unstable with a predicted oscillation frequency of 9.3 GHz.

3.4.3. GAIN MEASUREMENT

The gain measurement technique is similar to the method discussed in Section 3.3.2. The assembled grid is shown in Fig. 3.27(a). The polarizers are built on Duroid slabs with a relative dielectric constant of 2.2. The input and output tuners are also from the same material. The position of the polarizers and the tuners are optimized to improve the gain of the amplifier. The transmission-line equivalent circuit model of the grid at 10 GHz is shown in Fig. 3.27(b). Since the 20-Ω stabilizing resistor is shared between two cells, only half of it appears in the model. As discussed earlier this is a half-cell model, so free space appears as 189 Ω. The rest of the components in the model are similar to those described in Section 3.3.2.

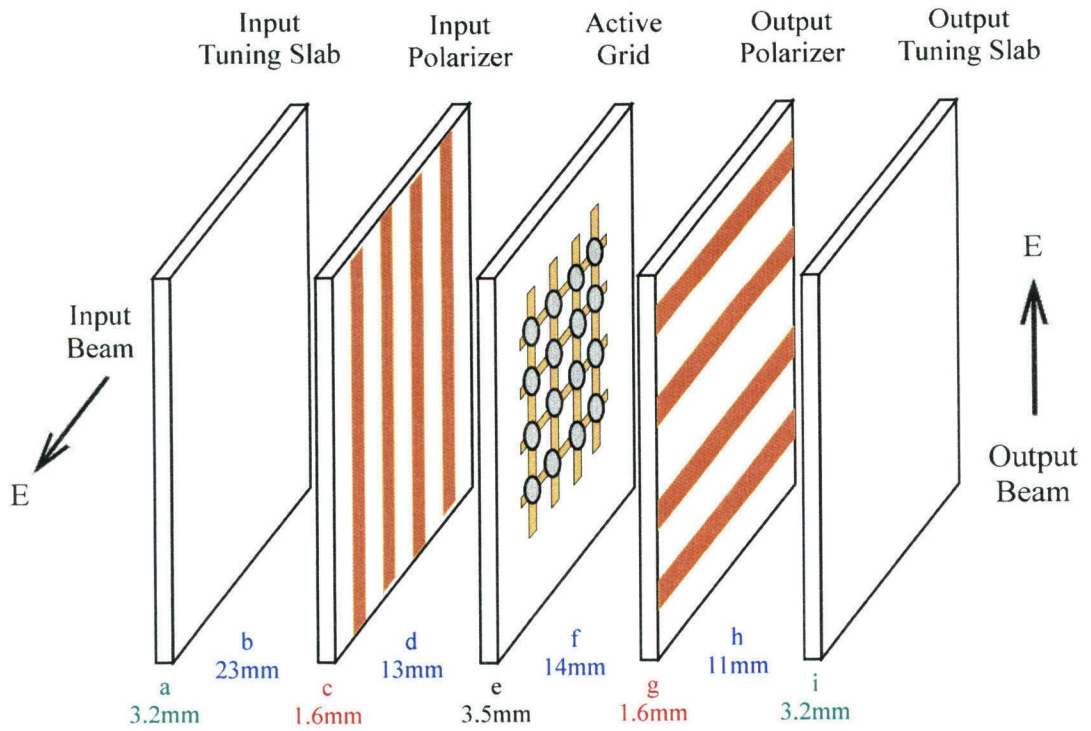

(a)

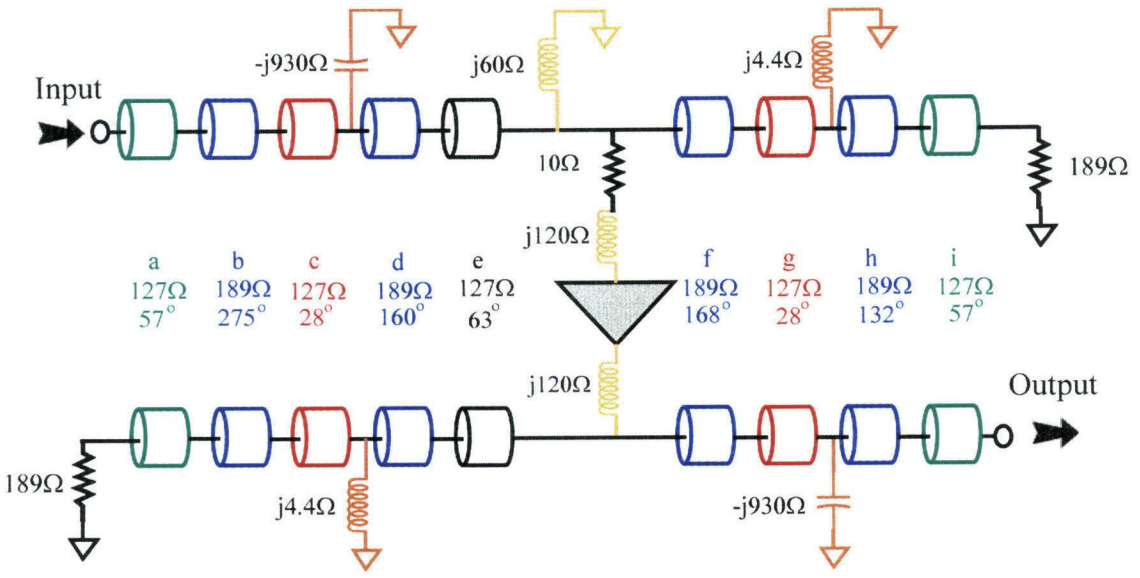

(b)

Figure 3.27. (a) The assembled HEMT grid amplifier. (b) The 10 GHz transmission-line equivalent circuit model.

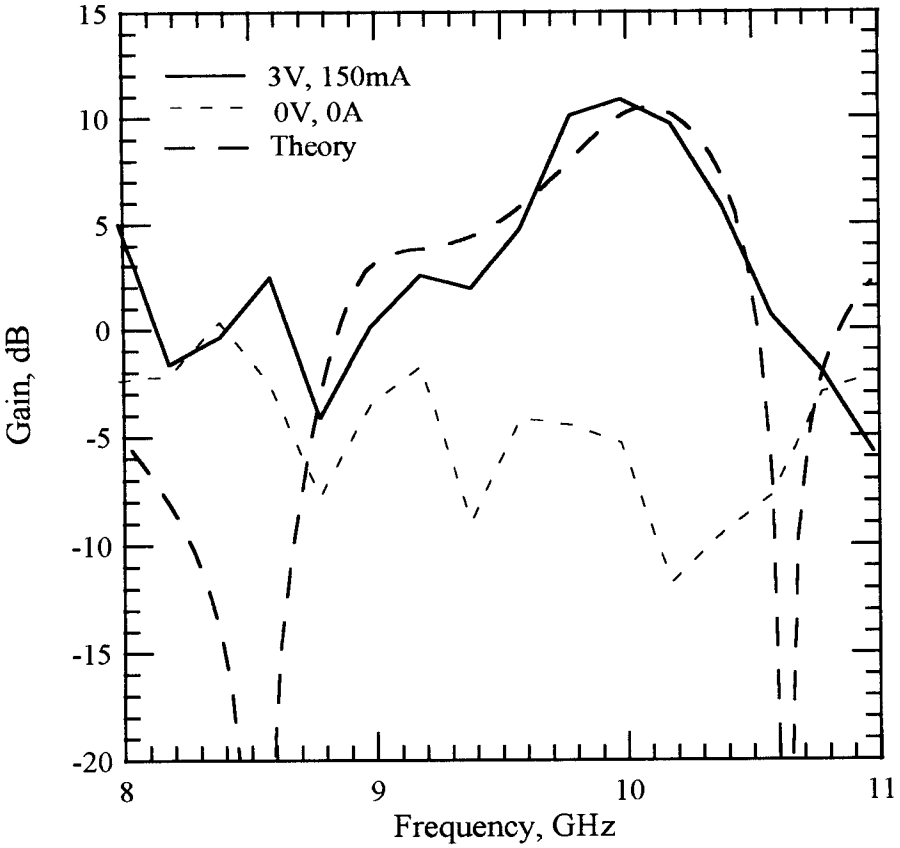

Figure 3.28. Gain response of the grid amplifier.

Fig. 3.28 shows the gain of the amplifier. The peak gain is 11 dB at 10 GHz, with a 3-dB bandwidth of 500 MHz, which corresponds to 5%. The grid is biased at a voltage of 2 V and a total drain current of 106 mA. The gates are biased at a voltage of 0.156 V. The theoretical gain of the amplifier using the transmission-line equivalent circuit shown in Fig. 3.10(b) is also plotted in the same figure. This theory agrees well with the measured gain. The zero-bias gain of the amplifier is also shown. This gain is about –5 dB at 10 GHz where the grid has its maximum gain.

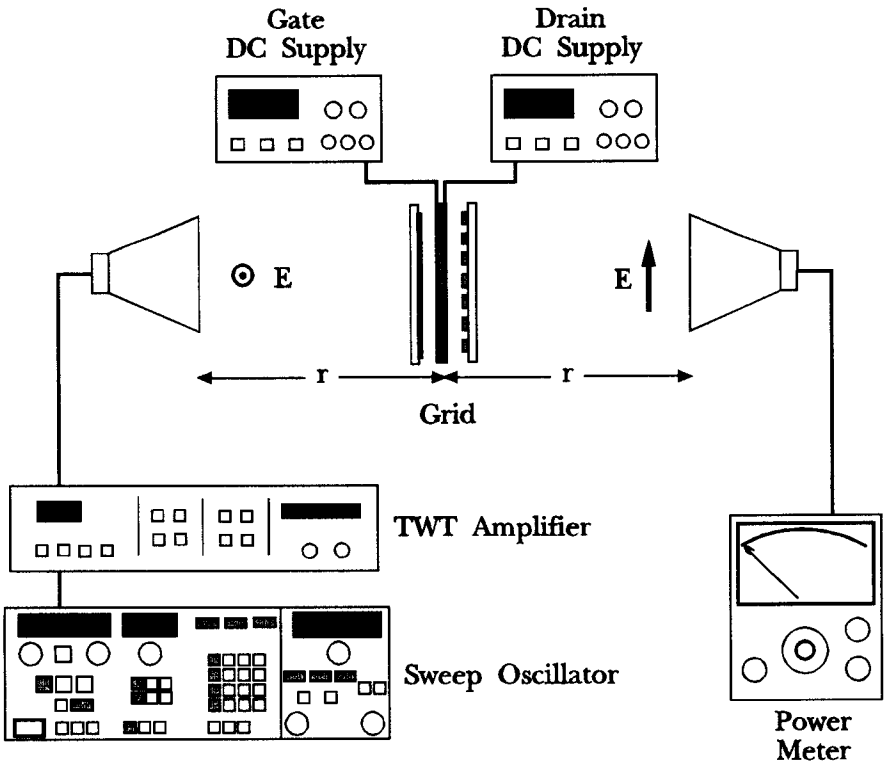

Figure 3.29. The power measurement setup.

3.4.4. POWER MEASUREMENT

The power saturation measurement was done using the setup shown in Fig. 3.29. A Hughes 1177H03 Travelling-Wave Tube Amplifier amplifies the output of a HP8350B sweep oscillator. A HP435B power meter was used to measure the output signal. Fig. 3.30 shows the output power of the grid versus the input power at 10 GHz for a drain bias of 3.5 V, total drain current of 130 mA and gate voltage of –0.061 V. The maximum output power is 166 mW for an input power of 76 mW.

Fig. 3.31(a) shows the power-added efficiency versus the input power for the same bias conditions. The grid has a maximum efficiency of 22.5% for an input power of 52 mW at 10 GHz. Fig. 3.31(b) is a plot of the power-added

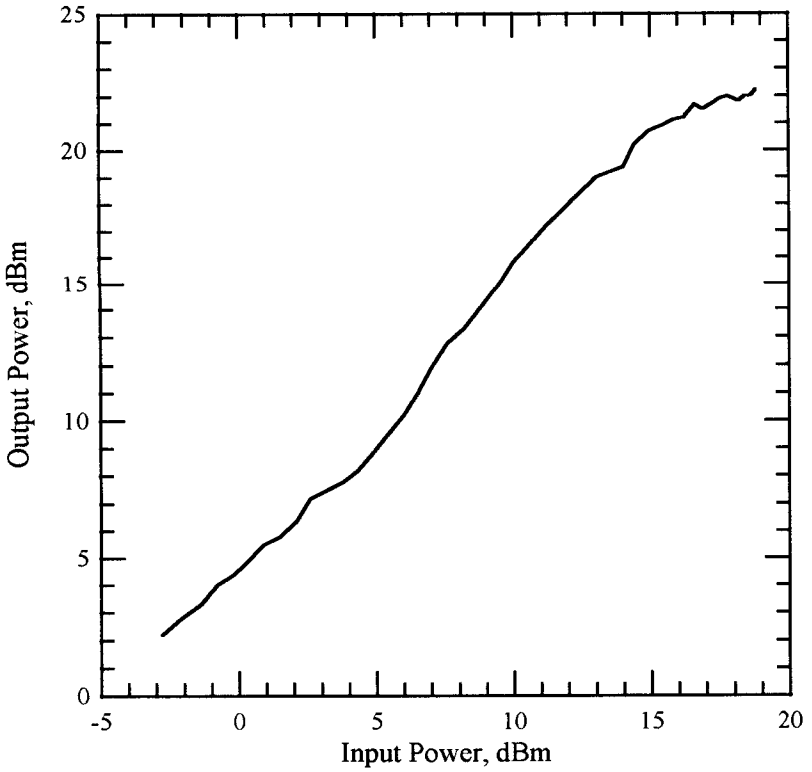

Figure 3.30. Output power versus the input power of the grid amplifier.

efficiency as a function of the output power. The peak efficiency is for an output power of 148 mW. This an improvement over the results of a previous X-band grid amplifier with a peak efficiency of 12% [4]. The improvement in efficiency is probably due to the shorting of the source resistors in this grid. The 12% efficiency reported in the previous grid is with the source resistors. Calculations indicated that in the case of that grid discounting the DC loss in the source resistors results in an efficiency of 20%, which is compareable to the results presented here.

Fig. 3.32 shows the gain of the grid versus the input power. The gain of the grid for these measurements is degraded to about 6 dB compared to its original gain of 11 dB at 10 GHz. It is possible that the devices in the grid are damaged because of operating in high powers and therefore the gain is dropped to 6 dB.

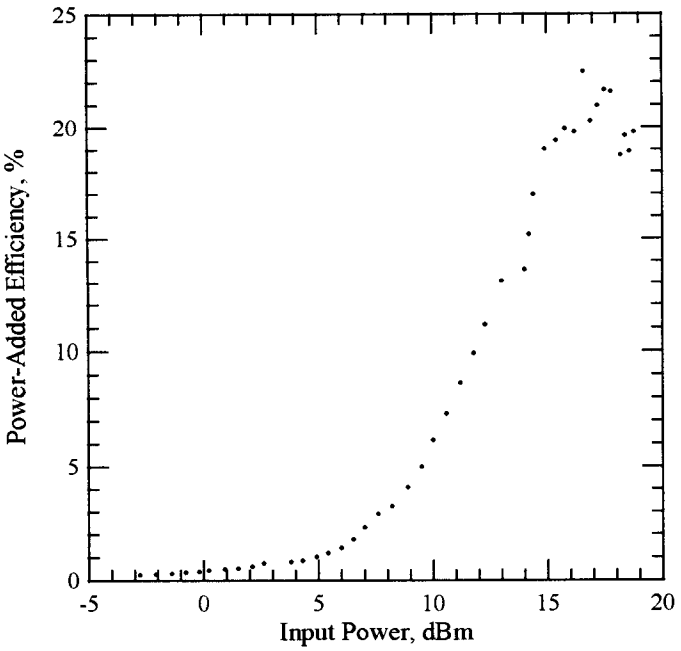

(a)

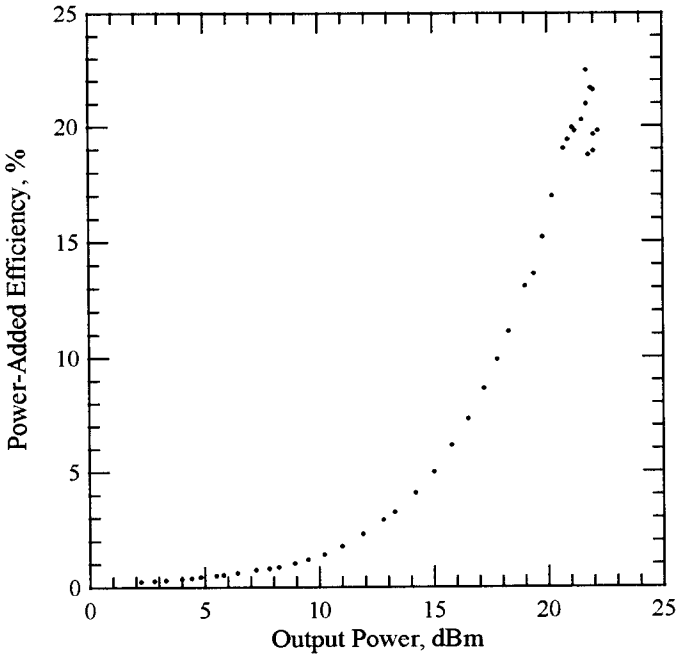

(b)

Figure 3.31. Power-added efficiency versus the input power (a), and the output power (b). The measurements were for a bias voltage of 3.5 V and current of 130 mA at 10 GHz.

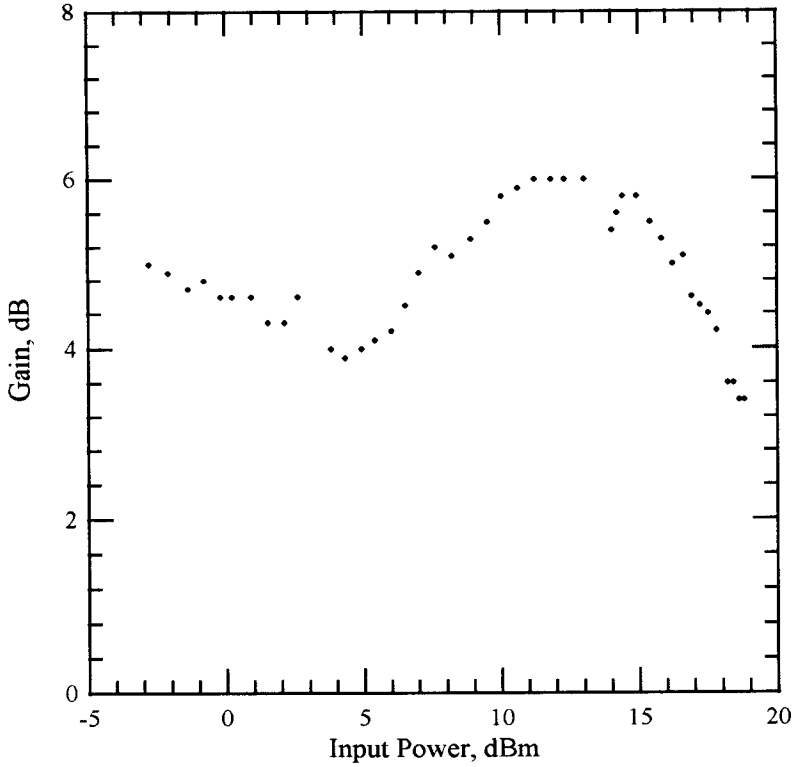

Figure 3.32. Gain of the grid amplifier versus the input power.

References

[1] M. Kim, J.J. Rosenberg, R.P. Smith, R.M. Weikle, J.B. Hacker, M.P. De Lisio, D.B. Rutledge, "A Grid Amplifier," *IEEE Microwave Guided Wave Lett.*, vol. 1, pp. 322–324, Nov. 1991.

[2] M. Kim, E.A. Sovero, J.B. Hacker, M.P. De Lisio, J.-C. Chiao, S.-J. Li, D.R. Gagnon, J.J. Rosenberg, D.B. Rutledge, "A 100-Element HBT Grid Amplifier," *IEEE Trans. Microwave Theory Tech.*, vol. 41, pp. 1762–1771, Oct. 1993.

[3] D.B. Rutledge, A. Moussessian, M.P. De Lisio, C.-M. Liu, J.J. Rosenberg, "Modelling of Transistor Grid Amplifiers," *1994 IEEE MTT-S Int. Microwave Symp.*, Workshop Notes, WFFA: Circuit Level Design and Modelling of Quasi-Optical Circuits and Systems, pp. C.1–C.16, 1994.

[4] M.P. De Lisio, S.W. Duncan, D.-W. Tu, C.-M. Liu, A. Moussessian, J.J. Rosenberg, D.B. Rutledge, "Modelling and Performance of a 100-Element pHEMT Grid Amplifier," *IEEE Trans. Microwave Theory Tech.*, vol. 44, pp. 2136–2144, December 1996.

[5] J.A. Higgins, E.A. Sovero, W.J. Ho, "44-GHz Mpnolithic Plane Wave Amplifiers," *IEEE Microwave Guided Lett.*, MGWL-5, pp. 347–348, October 1995.

[6] E.A. Sovero, Y. Known, D.S. Deakin, A.L. Sailer, J.A. Higgins, "A PHEMT-Based Monolithic Plane Wave Amplifier for 42 GHz," *1996 IEEE MTT-S Int. Microwave Symp.*, pp. 1111–1114, 1996.

[7] C.-M. Liu, E.A. Sovero, W.J. Ho, J.A. Higgins, D.B. Rutledge, "A Millimeter-Wave Monolithic Grid Amplifier," *Int. J. Infrared Millimeter Waves*, vol. 16, pp. 1901–1910, Nov. 1995.

[8] C.-M. Liu, E.A. Sovero, W.J. Ho, J.A. Higgins, M.P. De Lisio, D.B. Rutledge, "Monolithic 40-GHz 670-mW HBT Grid Amplifier," *1996 IEEE MTT-S Int. Microwave Symp.*, pp. 1123–1126, 1996.

[9] M.P. De Lisio, S.W. Duncan, D.-W. Tu, S. Weinreb, C.-M. Liu, D.B. Rutledge, "A 44-60 GHz Monolithic pHEMT Grid Amplifier," *1996 IEEE MTT-S Int. Microwave Symp.*, pp. 1127–1130, 1996.

[10] M.P. De Lisio, "Hybrid and Monolithic Active Quasi-Optical Grids," Ph.D. Thesis, California Institute of Technology. Pasadena, CA, 1996.

[11] R.S. Carson, *High-Frequency Amplifiers*, second ed., John Wiley & Sons, Inc., New York, 1982, pp. 228–268.

[12] G. Gonzalez, *Microwave Transistor Amplifiers*, Prentice-Hall, Inc., Englewood Cliffs, NJ, 1984, pp. 91–138.

[13] M. Kim, "Grid Amplifiers," Ph.D. Thesis, California Institute of Technology. Pasadena, CA, 1993.

[14] C.-M. Liu, E.A. Sovero, M.P. De Lisio, A. Moussessian, J.J. Rosenberg, D.B. Rutledge, "Gain and Stability Models for HBT Grid Amplifiers," *1995 IEEE AP-S Int. Symp. Dig.*, pp. 1292–1295, 1995.

[15] C.-M. Liu, "Monolithic Grid Amplifiers," Ph.D. Thesis, California Institute of Technology. Pasadena, CA, 1996.

[16] R.D. Martinez, R.C. Compton, "A General Approach for the S-Parameter Design of Oscillators with 1 and 2-Port Active Devices," *IEEE Trans. Microwave Theory Tech.*, vol. 40, pp. 596–574, March 1992.

Chapter 4

Electronically Tunable Grid Oscillator

This chapter discusses a tunable grid oscillator using a grid amplifier with external feedback. A combination of a varactor grid and a mirror $\lambda/4$ away from the varactor grid is used as the external positive feedback. The oscillator frequency is tuned by changing the bias voltage of the varactor grid. The theory for designing a varactor grid as a positive feedback element for an electronically tunable grid oscillator is discussed and the reflection measurements showing a tuning range of approximately 1.2 GHz are presented. This work was done in collaboration with Professors Jim Rosenberg and Michael De Lisio.

4.1. INTRODUCTION

As discussed in Section 1.3, in previous grid oscillators the frequency of oscillation was mainly determined by the passive structure containing the transistors. Since this passive structure cannot be altered after the grid is built, the phase delay in the feedback path is difficult to change, and frequency tuning is very limited [1,2].

A grid amplifier can be converted to a grid oscillator by adding a positive feedback circuit. Since a grid amplifier has cross-polarized input and output this positive feedback has to provide the necessary conversion between the two polarizations. By adjusting the phase delay in the feedback path a wider oscillation frequency range can be achieved than is possible with previous grid oscillators.

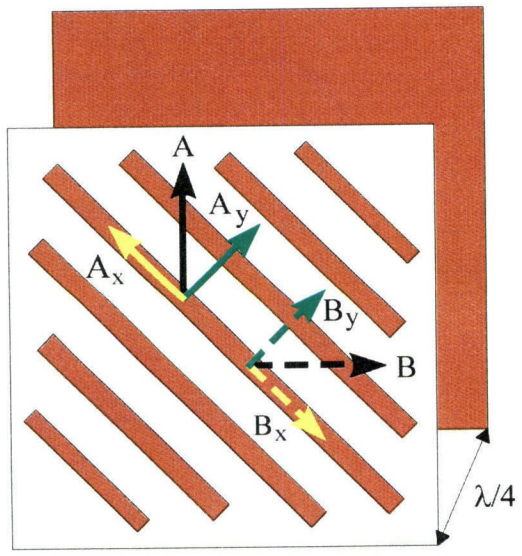

Figure 4.1. The feedback circuit consists of a 45° tilted polarizer and a mirror $\lambda/4$ away from the polarizer. The solid lines represent the input and the dashed lines represent the output beams and their components. The figure shows how the vertical input beam is converted into a horizontal beam.

To convert a grid amplifier to a grid oscillator, Moonil Kim used a 45° tilted polarizer with a mirror $\lambda/4$ away from the polarizer as the positive feedback [3,4]. This mirror and polarizer combination is similar to a half-wave plate in optics [5]. This half-wave plate converts the incident vertical polarization to horizontal polarization. Fig. 4.1 shows the input and the output beams and their components. The incident beam (A) is divided into two components: one component parallel to the tilted polarizer metal strips (A_x) and the other normal to the strips (A_y). The parallel component is reflected back (B_x). The normal component transmits through the polarizer, travels a distance of $\lambda/4$, reflects off the mirror and travels the same distance of $\lambda/4$ back towards the tilted polarizer. At this point the phase of the normal component is changed by 360°. Therefore the resulting component (B_y) returns in the same direction as the normal component of the input (A_y). Combination of B_x and B_y results in a horizontal output beam (B). This feedback circuit converts the incident beam into a cross-polarized beam with almost no loss over a large frequency range [3].

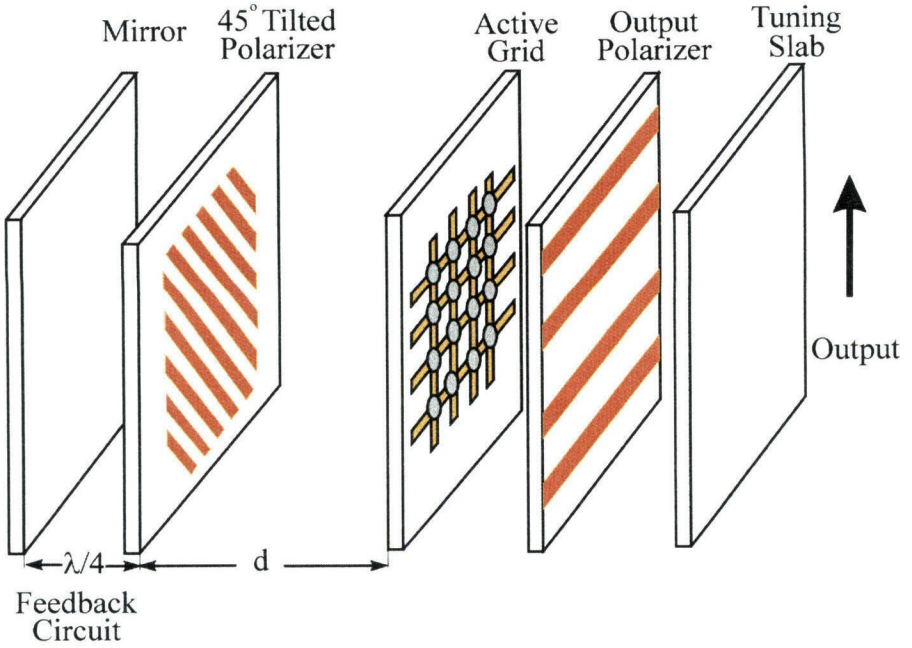

Figure 4.2. Moonil Kim's external feedback oscillator. The half-wave plate feedback circuit replaces the input polarizer and provides positive feedback. To tune the oscillation frequency of the oscillator the distance between the half-wave plate and the active array is varied.

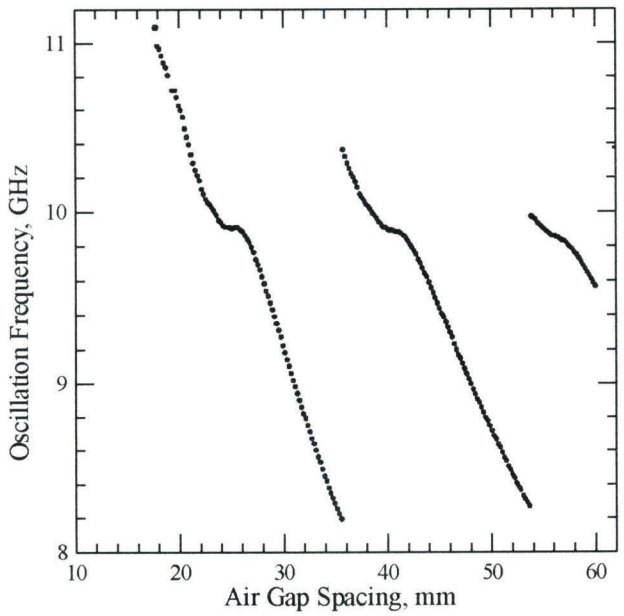

Figure 4.3. Oscillation frequency versus the air-gap spacing between the half-wave plate and the active array.

The input polarizer of an HBT amplifier grid arrangement, similar in design to the HEMT grid amplifiers discussed in Chapter 3, was replaced by a half-wave plate circuit [3,4]. Fig. 4.2 shows the arrangement. The oscillation frequency was tuned smoothly from 8.2 GHz to 11 GHz by varying the distance between the half-wave plate and the active array. As the air gap is varied the appropriate phase delay in the feedback path that initiates sustaining oscillations occurs at a different frequency. Fig. 4.3 shows the frequency of the oscillation versus the air-gap distance.

Instead of changing the air-gap spacing to tune the frequency of the oscillation, it is more desirable to electronically tune the frequency. The goal of this project is to accomplish this.

4.2. IMPLEMENTATION

Varactor diode grids have shown varying phase delays for quasi-optical RF beams [6,7]. A varactor grid in the feedback path of a grid oscillator was used to build a Voltage Control Oscillator (VCO) with a tuning range of 10% [8]. A varactor grid can also be used in the feedback path of a grid amplifier with external positive feedback to accomplish electronic frequency tuning. Because of the broadband gain of grid amplifiers, a much wider tuning range is expected than has been possible with previous oscillator grids. Fig. 4.4 shows the concept. The tilted polarizer of Fig. 4.2 is loaded with varactor diodes. Instead of changing the air-gap spacing between the polarizer and the amplifier grid the phase delay in the feedback path is changed by varying the bias voltage of the varactor grid. The 45° tilted metal structure of the varactor grid not only converts the vertical polarization to a horizontal polarization but also provides biasing for the diodes in the grid.

A possible design for the unit cell and its equivalent circuit are shown in Fig. 4.5. A varactor diode is mounted in the gap between two fingers in each cell. The equivalent circuit consists of an inductor (L) in series with the diode and a

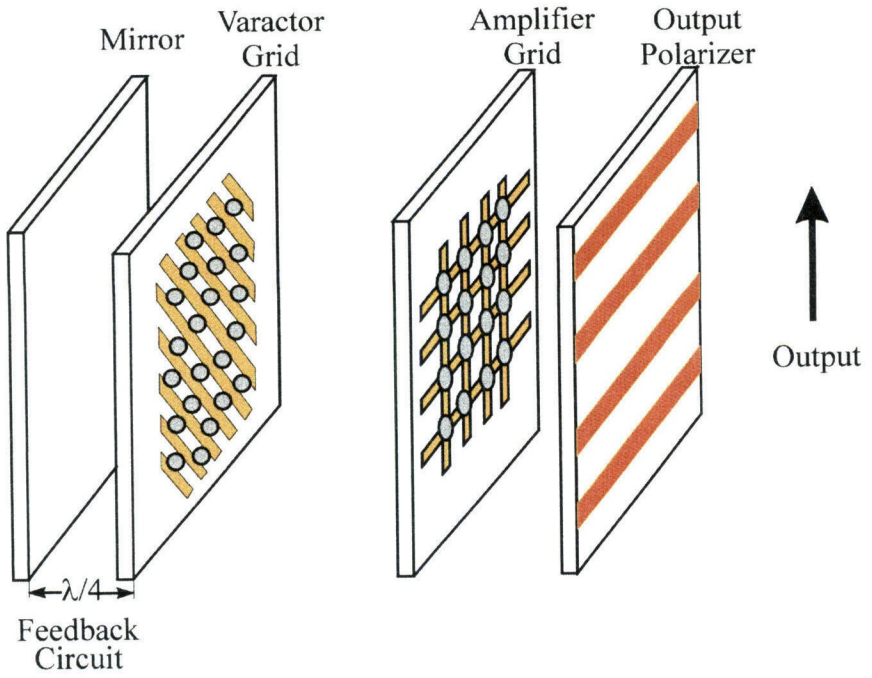

Figure 4.4. Electronically tunable grid oscillator. Varactor diodes are placed in the tilted polarizer. Tuning is achieved by changing the bias voltage of the diodes.

parallel capacitance (C_g). The inductor is due to the fingers in each cell and the capacitor is due to the gap between the two halves of the unit cell. The varactor diode can be modelled as a variable capacitor (C_v) in series with a resistor (R).

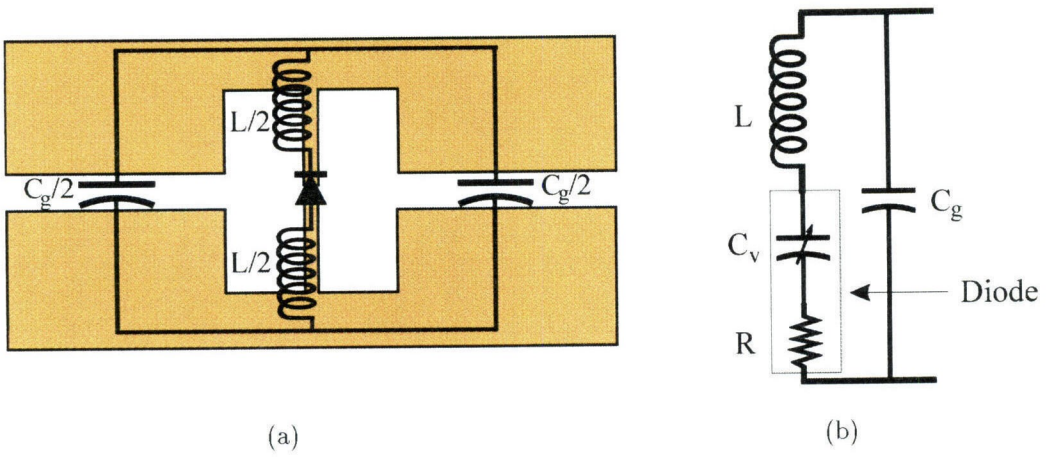

Figure 4.5. (a) The varactor grid unit cell. (b) The unit cell equivalent circuit.

The resonant frequency of the circuit in Fig. 4.5(b) is given by:

$$f_r = \frac{1}{2\pi\sqrt{LC_{eff}}}, \tag{4.1}$$

where C_{eff} is the series combination of the grid capacitance C_g and the varactor capacitance C_v and is given by:

$$\frac{1}{C_{eff}} = \frac{1}{C_g} + \frac{1}{C_v}. \tag{4.2}$$

As the bias voltage of the varactor grid is varied the capacitance of the varactor diode (C_v) and thereby the grid resonant frequency is varied. To initiate oscillation the signal fed back from the varactor grid must return to the amplifier grid with a multiple of 360° phase delay. This phase delay is provided by the variable phase of the varactor grid, the transistors in the amplifier grid, and the air gap in between. As shown in Fig. 4.6, for small values of R (diode effective resistance) the phase of the varactor grid has a sharp transition from +90° to –90° at resonance. If the phase necessary to complete the total required multiple of 360° phase delay is in this range the varactor grid can provide this phase at a frequency very close to its resonance frequency. Moreover, at resonance the varactor grid acts similar to the half-wave plate shown in Fig. 4.1. At resonance

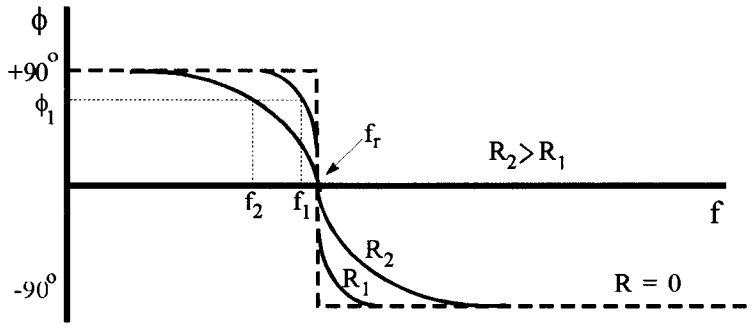

Figure 4.6. Varactor grid phase versus frequency. At resonance ($f = f_r$) the phase transitions from +90° to –90°. As R gets larger this transition spans a larger frequency. For a grid with a larger effective loss ($R = R_2$) the same phase shift (ϕ_1) happens at a frequency that is farther away from resonance (f_2 as opposed to f_1 for $R = R_1$).

the grid is an open circuit for the component of the signal normal to the 45° tilted bias lines of the grid (similar to A_y in Fig. 4.1), providing close to a 100% transmission for that component. These bias lines act as a short for the component of the signal along the strips (similar to A_x in Fig. 4.1). Therefore the varactor grid not only provides the appropriate phase change for initiating oscillation but also converts the vertical output polarization of the amplifier grid to a horizontal polarization that is fed back to the amplifier. To achieve a large tuning range for the oscillator grid the varactor grid must be designed to resonate at a large range of frequencies as the bias voltage of the grid varies.

4.3. VARACTOR GRID DESIGN AND CONSTRUCTION

Fig. 4.7(a) shows a 5×5 varactor grid. The diode orientation in each cell and the bias for each row are shown in the figure. Hewlett-Packard's High Frequency Structure Simulator (HFSS) [9], a 3-D finite-element electromagnetic-wave solver, is used to find the equivalent circuit model for the varactor-grid unit cell (the area darkened in Fig. 4.7(a)). As discussed in Section 4.1 only the component of the signal normal to the 45° metal structure is transmitted through the varactor grid. Therefore this is the only component taken into account when modelling the unit cell. The current distribution due to this signal is also shown in Fig. 4.7(a).

Due to the symmetry of the cell and for simplicity only one fourth of this unit cell as shown in Fig. 4.7(b) is used in HFSS simulations. The current distribution on the grid allows the top and bottom waveguide walls to be replaced by electric walls, and the right and left walls with magnetic walls. To further simplify the problem it is assumed that the metal finger extends all the way to the electric wall. This neglects the capacitance between the two fingers in a cell which is assumed to be small compared to C_g.

Fig. 4.8 shows the gain curve versus frequency for Moonil Kim's HBT grid amplifier. We were interested in designing a varactor grid to use as a tuning element for this grid amplifier which had gain at the frequency range of 8 GHz

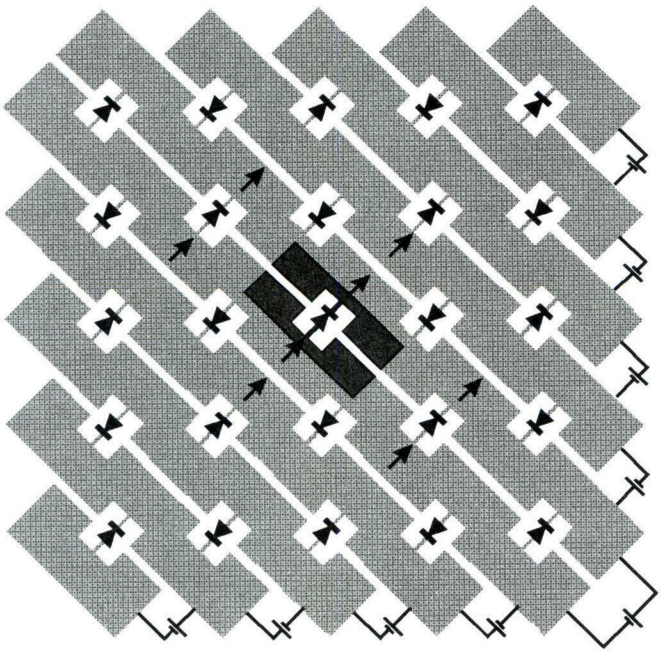

(a)

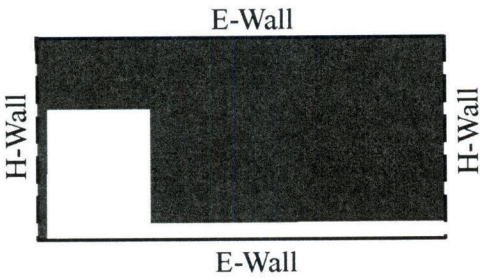

(b)

Figure 4.7. (a) The darkened area on the varactor grid shows the varactor grid unit cell. (b) By symmetry the unit cell can be reduced to one fourth of the entire cell for use in HFSS simulation and the symmetry planes can be replaced by electric and magnetic walls.

to 11 GHz. Therefore the varactor grid was designed to provide tuning in this range. Fig. 4.9 shows the dimensions of the varactor-grid unit cell that was selected for this design. The values for the equivalent circuit components are $L = 1.7\,\text{nH}$ and $C_g = 340\,\text{fF}$ for the full unit-cell equivalent circuit shown in Fig. 4.5(b). The varactor diode is M/A-Com's MA46471-277. The capacitance of the diode varies from 1 pF at a bias voltage of 0 V to 0.2 pF at 20 V. The loss of

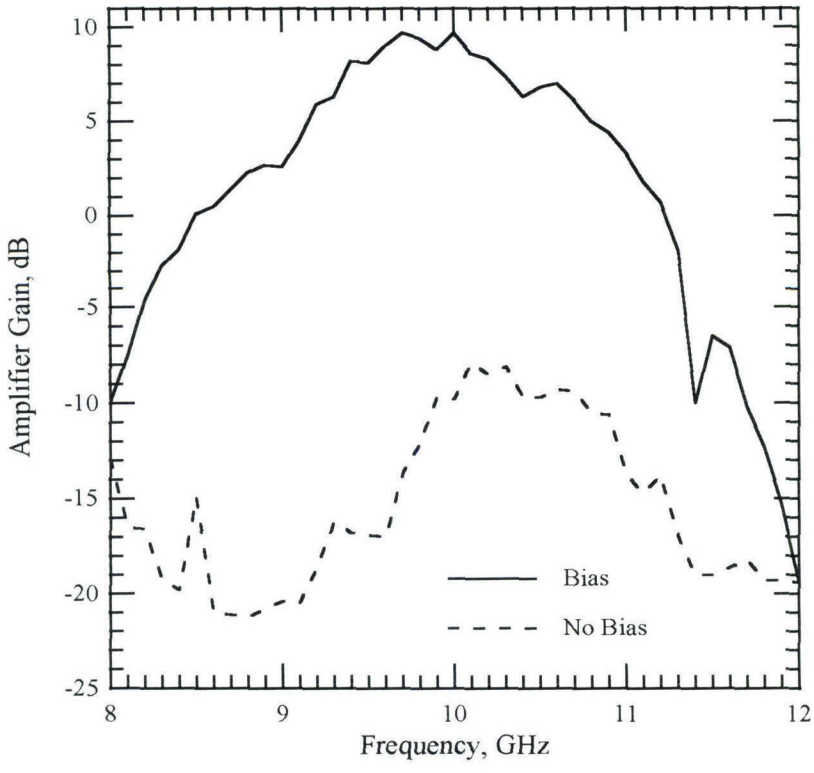

Figure 4.8. Gain versus frequency for the 100-element HBT grid amplifier [2].

the diode is modelled as a 0.55-Ω resistor in series with the capacitance C_v. The equivalent circuit S-parameters and the HFSS results are plotted in Fig. 4.10. For the frequency range of interest there is good agreement between the HFSS simulated results and the equivalent circuit.

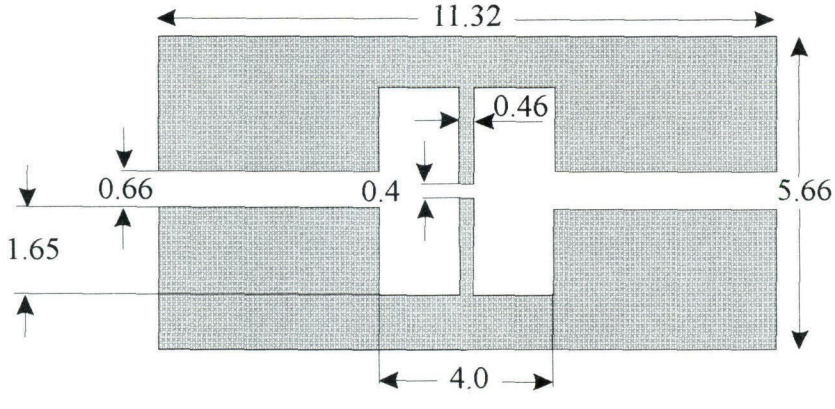

Figure 4.9. The unit cell of the varactor grid. All the dimensions are in millimeters.

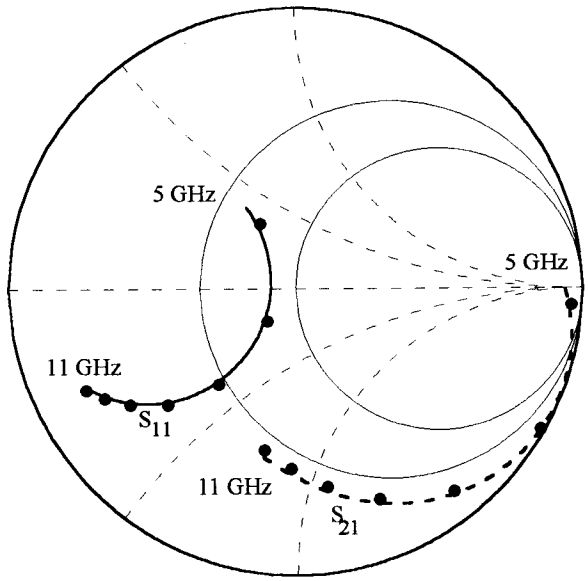

(a)

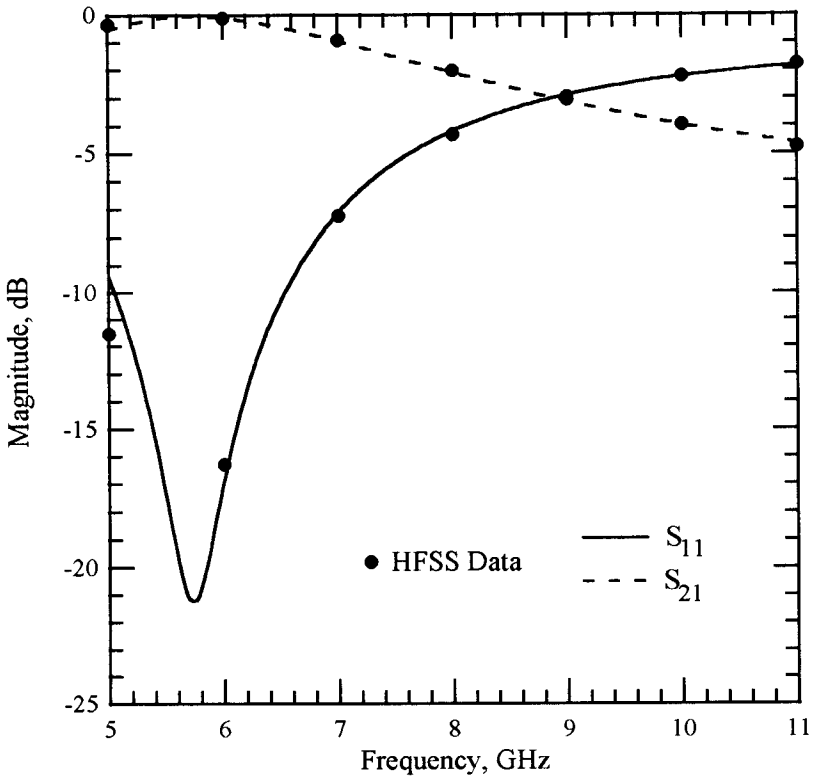

(b)

Figure 4.10. The varactor grid unit-cell S-parameters derived from HFSS compared to the lumped element equivalent circuit. (a) Smith chart plot. (b) Magnitude.

To model the positive feedback circuit, consisting of the varactor grid and a mirror $\lambda/4$ away from the front of the grid, a 45° rotation matrix is defined. The four ports are defined as: vertical polarization for port 1, horizontal for port 2, port 3 is the polarization in the direction along the strips of the 45° tilted metal structure of the varactor grid, and port 4 has a polarization normal to the metal strips. The 45° rotation matrix is given by:

$$S = \begin{pmatrix} 0 & 0 & -\frac{\sqrt{2}}{2} & \frac{\sqrt{2}}{2} \\ 0 & 0 & \frac{\sqrt{2}}{2} & \frac{\sqrt{2}}{2} \\ -\frac{\sqrt{2}}{2} & \frac{\sqrt{2}}{2} & 0 & 0 \\ \frac{\sqrt{2}}{2} & \frac{\sqrt{2}}{2} & 0 & 0 \end{pmatrix}. \tag{4.3}$$

Fig. 4.11 shows the positive feedback circuit and its transmission-line equivalent circuit model. Because of the symmetry of the cell only half of the unit cell shown in Fig. 4.5(a) needs to be modelled. The vertically polarized beam from the grid amplifier approaches the varactor grid (port 1 of S in Fig. 4.11(b)) after traveling the air gap spacing between the amplifier and the positive feedback circuit (c). As discussed in Section 3.2 this air gap (not shown in Fig. 4.11(a)) is modelled as a transmission line with an impedance of 377 Ω. The electrical length of the transmission line is assumed to be 62° at 10 GHz and will be discussed later. Ideally the bias lines of the varactor grid act as a short for the component of the beam along the metal strips of the grid. This is shown as a short at port 3 of the rotation matrix S. The component normal to the bias strips (port 4 of S) is transmitted through the varactor grid, its substrate (a), the free space behind it (b), and reflects off the mirror that is modelled as a short. Similar to transmission line c this substrate (a) and the free space (b) are modelled as transmission lines. An equivalent circuit similar to the one shown in Fig. 4.5(b) is used to model the varactor grid. However, the values of the circuit components are for half the unit cell and are represented with primed letters. The horizontal output from port 2 of S travels the air gap spacing (c) and reaches the amplifier.

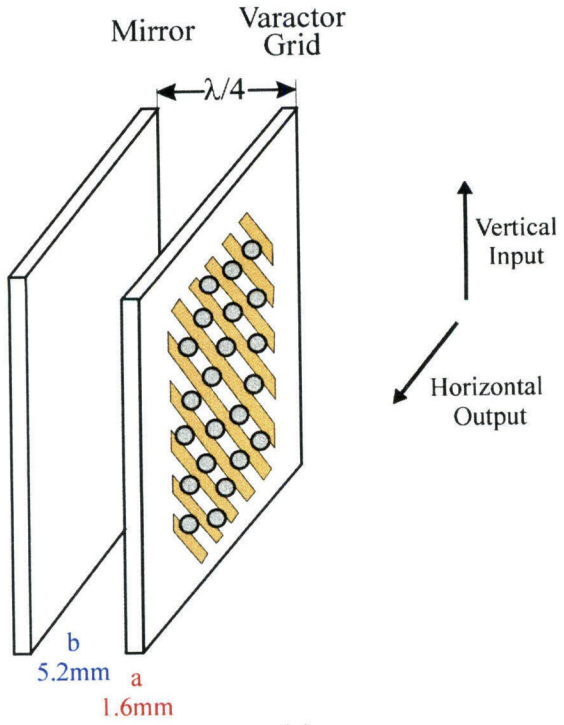

(a)

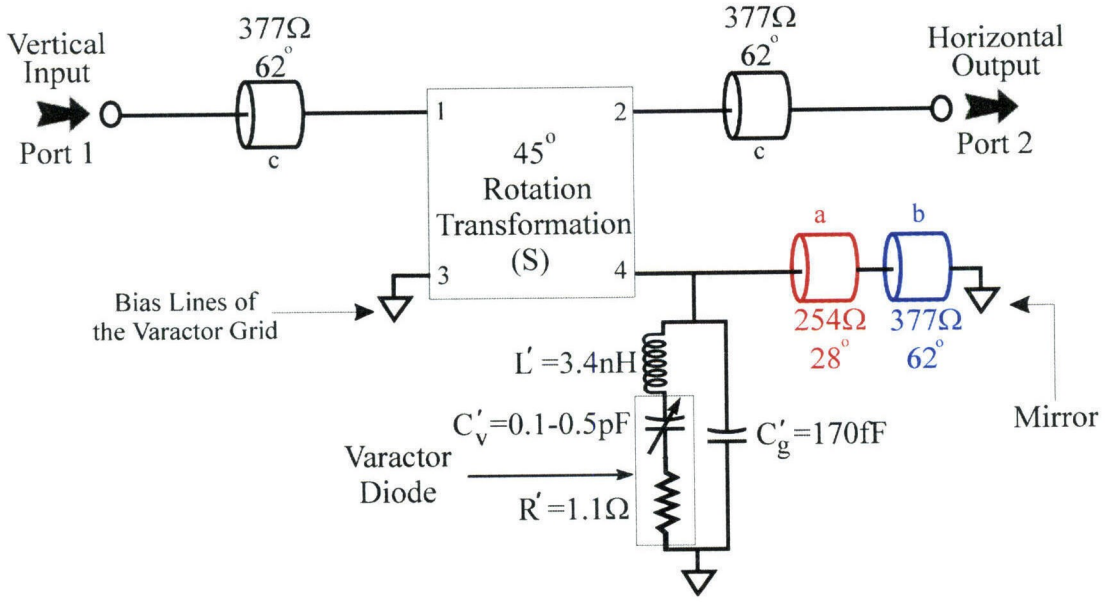

(b)

Figure 4.11. (a) The positive feedback circuit. (b) The half-cell equivalent circuit model of (a) at 10 GHz.

As previously mentioned, to initiate sustaining oscillations we require a multiple of 360° phase delay for the fed back signal which is provided by the varactor grid, the transistors in the amplifier grid, and the air gap in between. Since our model does not include the phase delay contributed by the transistors in the grid amplifier, we have no knowledge of the S_{21} phase requirement for the feedback circuit of Fig. 4.11(b) which models the varactor grid and the air gap between the varactor and the amplifier grids (c). This also means that we have no knowledge of the length requirement for the transmission line c in Fig. 4.11(b). Therefore an arbitrary length of 5.2 mm (equivalent to an electrical length of 62° at 10 GHz) is chosen for c. Figs. 4.12 to 4.14 show the S-parameters of the feedback circuit for 3 different values of C_v' when c is 5.2 mm. Changing the length of the transmission line c has no effect on the magnitude of the S-parameters, however, the phases of the S-parameters change with this distance. We assume that a phase delay of −110° for S_{21} is the criteria for oscillation. The frequency where S_{21} has a phase delay of −110° is marked with a × in Figs. 4.12 to 4.14. As shown in Fig. 4.12 the resonant frequency of the feedback circuit is close to 8 GHz for the unbiased grid ($C_v' = 0.5\,\text{pF}$). This resonant frequency increases as the grid bias voltage is increased, until it reaches a resonant frequency close to 10.5 GHz for the grid bias voltage of 20 V ($C_v' = 0.1\,\text{pF}$) as shown in Fig. 4.14. Therefore a total tuning range of 8 GHz to 10.5 GHz is achieved. Fig. 4.13 shows the phase and the magnitude of S_{21} and S_{11} when C_v' is 0.25 pF. For this C_v' the phase requirement for oscillation occurs right at resonance (8.6 GHz). As the bias voltage is varied the phase criteria of −110° for S_{21} can always be found near resonance. For values of C_v' smaller than 0.25 pF the phase requirement for oscillation occurs before resonance and for C_v' larger than 0.25 pF the phase criteria is fulfilled at a frequency above the resonance. Operating close to resonance is important to achieve the required phase delay for initiating oscillations; moreover, from Figs. 4.12 to 4.14 it is obvious that at frequencies near resonance the magnitude of S_{21} is close to

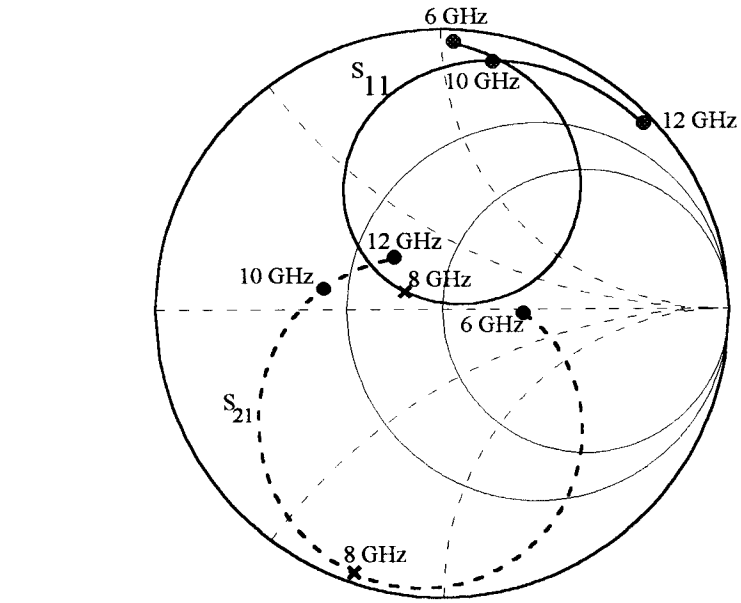

(a)

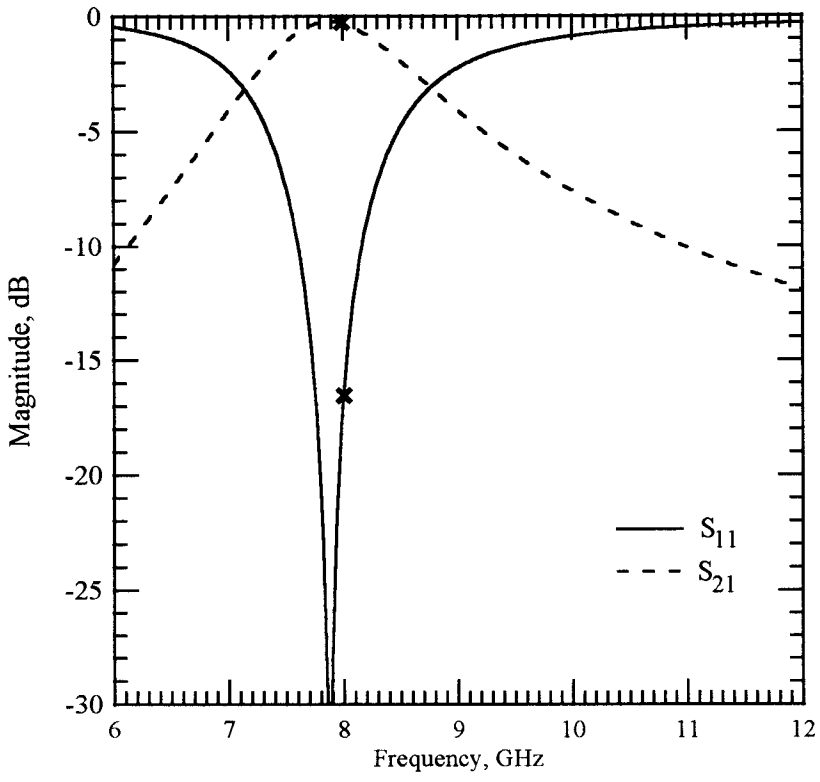

(b)

Figure 4.12. S_{11} and S_{21} for the positive feedback circuit at 0 V of bias. $\times$ shows the frequency where S_{21} has a phase of $-110°$. (a) Smith chart plot. (b) Magnitude.

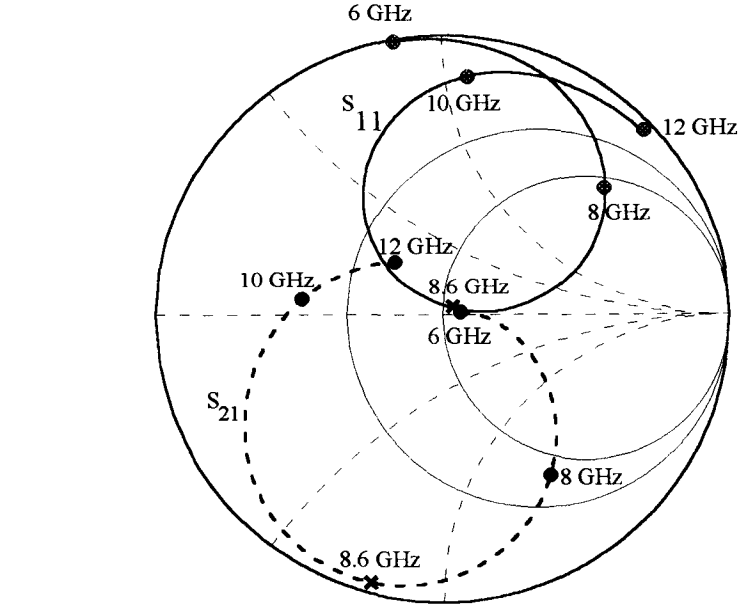

(a)

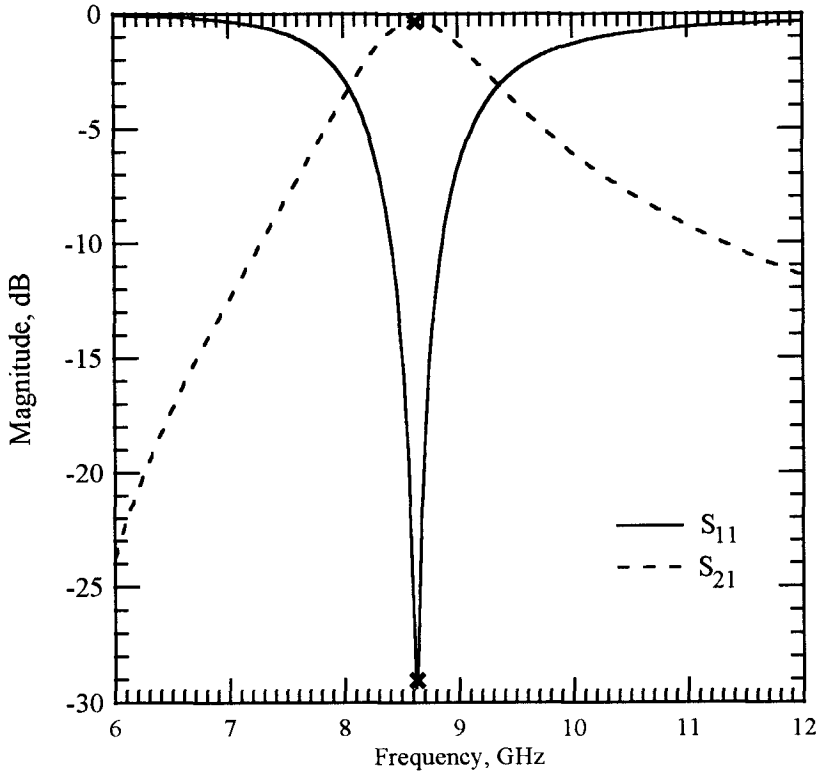

(b)

Figure 4.13. S_{11} and S_{21} for the positive feedback circuit for $C_v' = 0.25\text{pF}$. $\times$ shows the frequency where S_{21} has a phase of $-110°$. (a) Smith chart plot. (b) Magnitude.

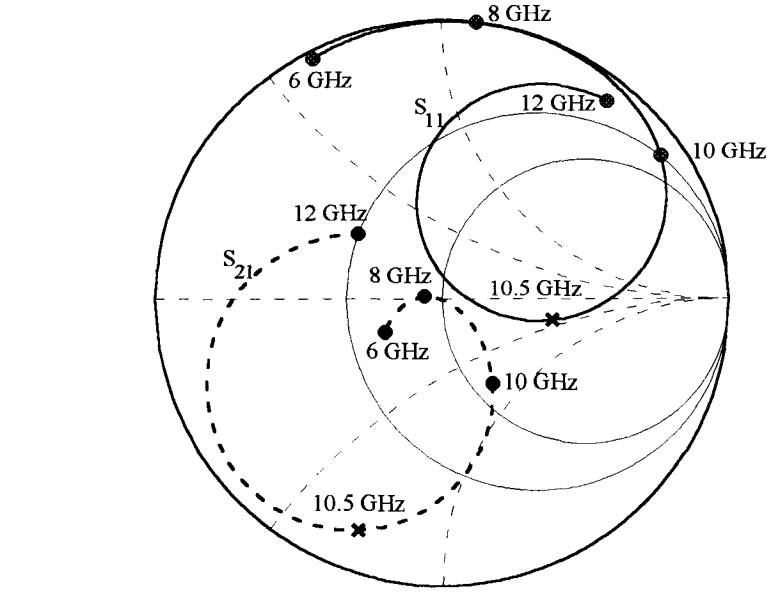

(a)

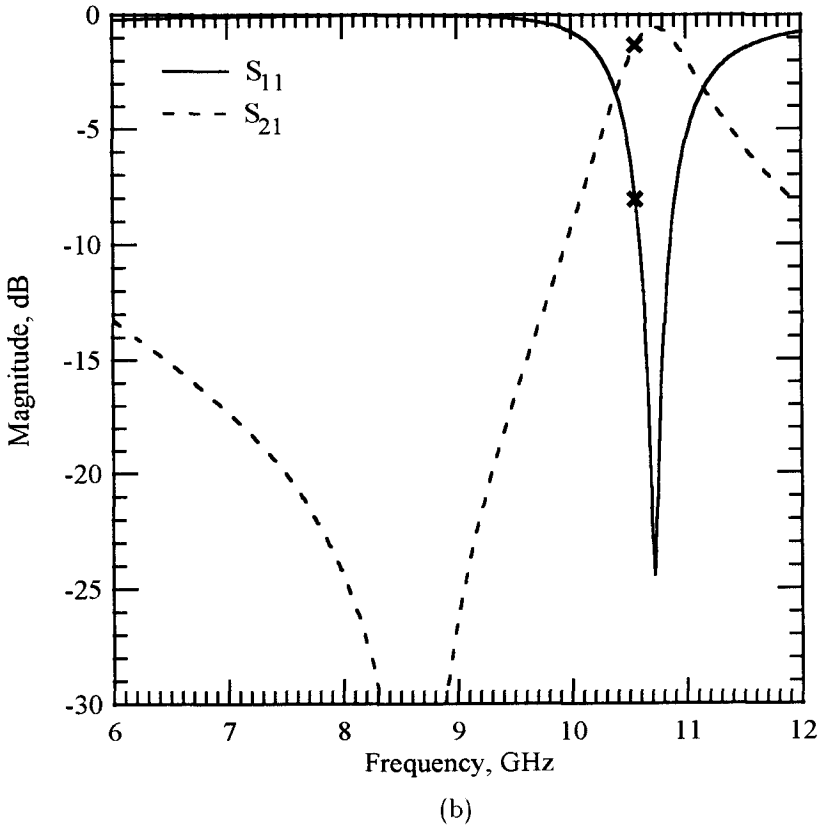

(b)

Figure 4.14. S_{11} and S_{21} for the positive feedback circuit at 20 V of bias. $\times$ shows the frequency where S_{21} has a phase of $-110°$. (a) Smith chart plot. (b) Magnitude.

0 dB. This means that there is good transmission for the component of the signal normal to the varactor grid bias lines.

Using the phase delay of $-110°$ for the oscillation criteria not only assumes that the amplifier grid provides the remaining phase necessary to complete the multiple of 360° phase delay but it also assumes that this phase delay is constant with frequency. In practice transistors have a frequency-dependant phase shift. However, this does not interfere with the operation of the oscillator since near resonance the varactor grid can provide any phase in the range of $-90°$ to $+90°$ that is necessary to complete the total multiple of 360° phase delay. As long as the phase delay of the amplifier transistors are within this range the varactor grid can provide the remaining phase necessary for initiating oscillations.

By choosing different air-gap spacings between the varactor grid and the amplifier grid different tuning ranges can be achieved. In practice the optimum air-gap spacing between the feedback circuit and the amplifier grid is selected to provide tuning in the frequency range of interest. Once this distance is set frequency tuning will occur by changing the varactor bias voltage.

A 5×5 varactor grid with a unit cell shown in Fig. 4.9 was fabricated. Fig. 4.15 shows pictures of this grid that is fabricated by etching the copper cladding of a Duroid substrate with relative dielectric constant of 2.2 and thickness of 1.6 mm. To facilitate wire bonding the grid is gold plated. The metalized back side of each diode which is also the cathode of the device is connected to the grid by soldering it to a finger in each unit cell. The anode connection to the other finger is made with a wire bond.

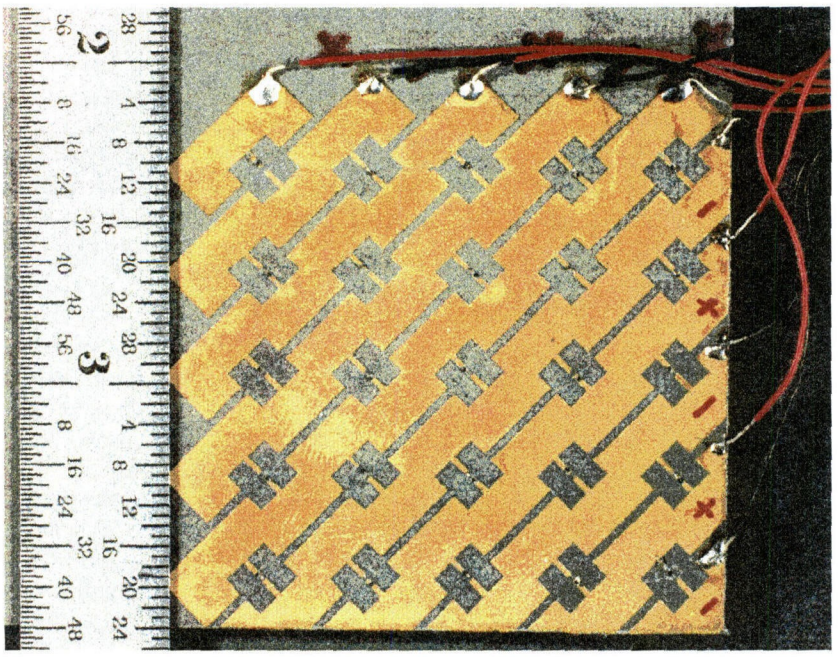

(a)

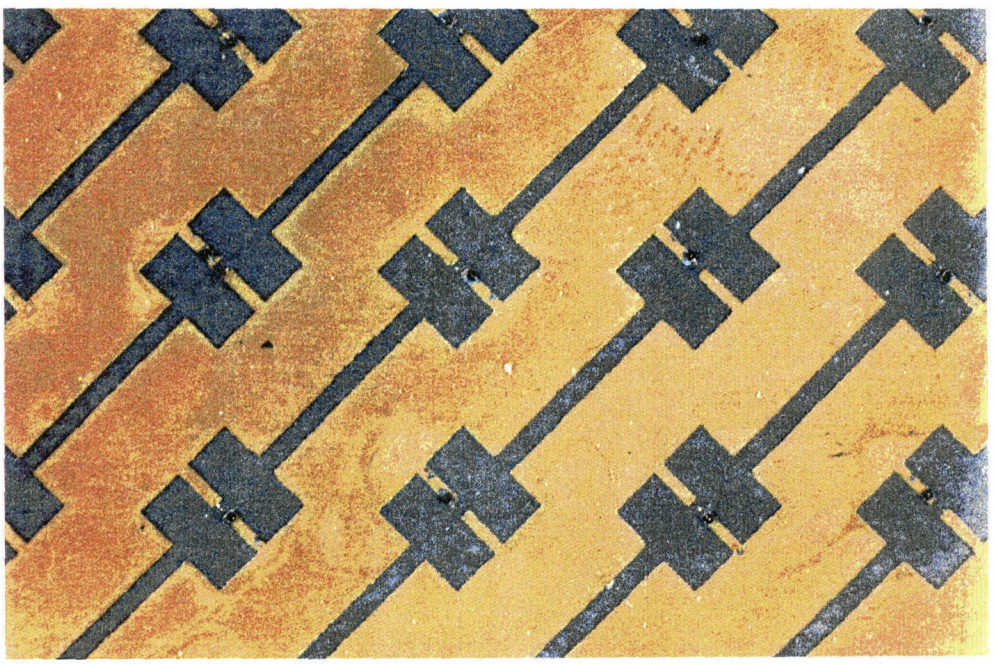

(b)

Figure 4.15. (a) The 5×5 varactor grid . (b) A closeup of the varactor grid.

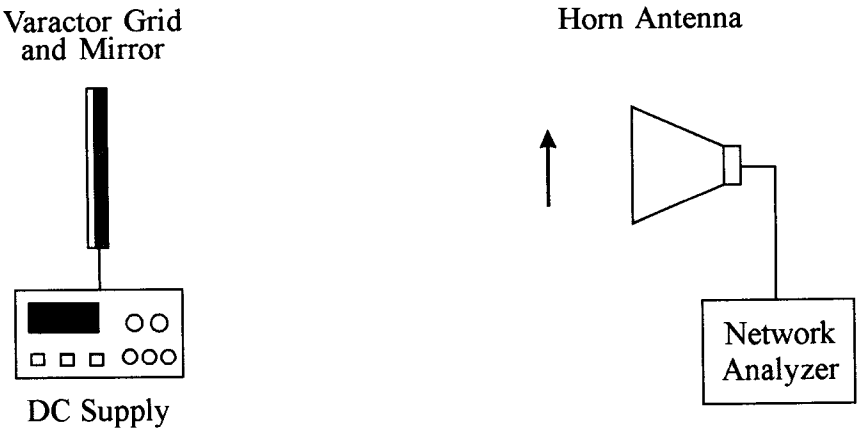

Figure 4.16. Quasi-Optical reflectometer measurement setup.

4.4. MEASUREMENTS

The reflection coefficient of the varactor grid and mirror combination can be measured using a quasi-optical reflectometer [10]. The measurement setup is shown in Fig. 4.16. To calibrate the network analyzer we need three standards that are well separated on the Smith chart. A standard calibration kit for a network analyzer consists of a short, an open and a 50-Ω load. For this quasi-optical reflectometer system a metal sheet can be used as a short and a good absorbing material can be used as the matched load. Since quasi-optical open circuits do not exist a delayed short is used as the third calibration standard. The delayed short in our measurement is a copper sheet translated by 6.3 mm from the reference plane.

Fig. 4.17 shows the results of the reflection measurements. For convenience, instead of an air gap between the varactor grid and the mirror a piece of Duroid with the same dielectric constant as the varactor grid substrate is used to maintain the $\lambda/4$ spacing between the front of the varactor grid and the mirror. Fig. 4.17(a) shows the measured reflection coefficient at a bias voltage of 0 V and Fig. 4.17(b) shows the same measurement for a bias voltage of 20 V. The theoretical curves are also plotted.

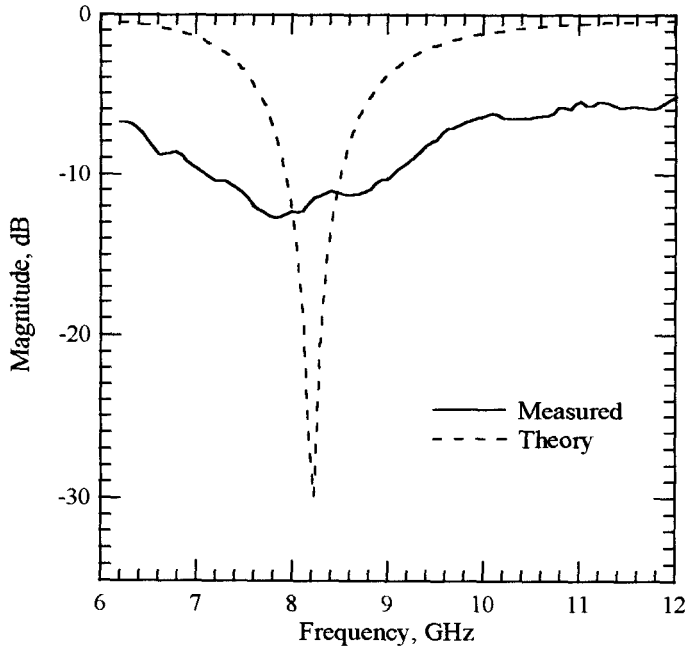

(a)

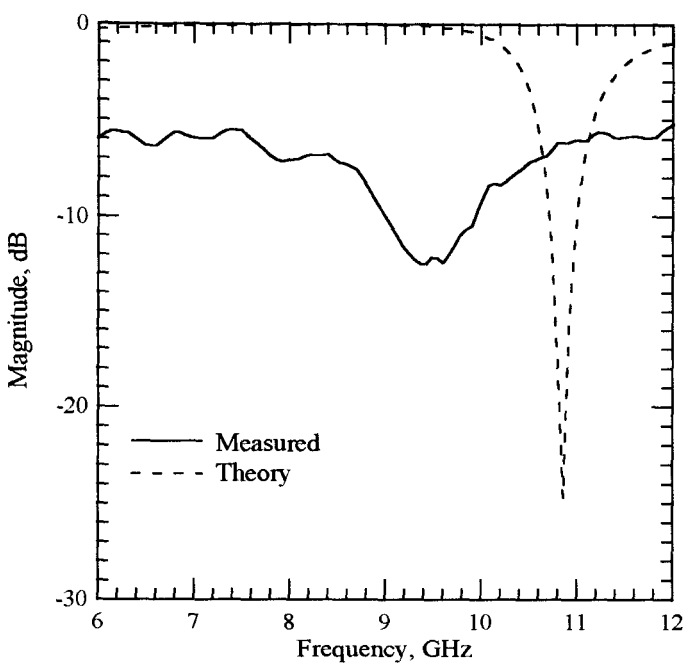

(b)

Figure 4.17. Reflection coefficient of the feedback circuit for a bias voltage of 0 V (a), and 20 V (b).

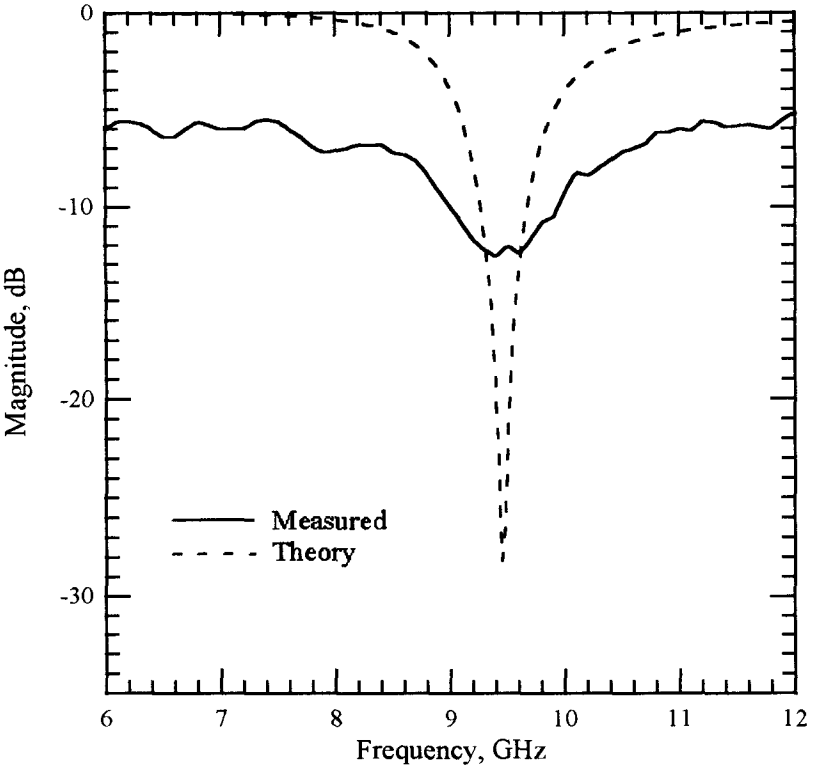

Figure 4.18. Corrected reflection coefficient at 20 V of bias.

The frequency where the measured reflection coefficient of the unbiased feedback circuit has a dip agrees well with the theory (Fig. 4.17(a)). However, when the grid is biased at 20 V there is a discrepancy in the location of the dip between measured and theoretical curves (Fig. 4.17(b)). As shown in Fig. 4.7(b), in the HFSS simulation of the unit cell it was assumed that the finger extends all the way to the E-wall, ignoring the capacitance between the two fingers in a cell. The discrepancy in the measurement shown in Fig. 4.17(b) is a result of ignoring this capacitance in calculating the theoretical curves. Adding a 75 fF capacitance in parallel with the half-cell diode capacitance (C_v') moves the dip of the theoretical curve to the measured result (Fig. 4.18). The addition of this capacitance does not have a major effect on the theoretical curve of the unbiased varactor grid because this capacitance is small compared to the 0.5-pF half-cell capacitance of the unbiased varactor diode.

The dips in the measured curves are not as deep as the theory predicts. This is probably due to diffraction losses in the measurement.

By the time this grid was fabricated, the gain of the HBT grid amplifier had degraded. This was possibly due to a problem with the passivation of the HBT's. Therefore we were not able to make any oscillation measurements.

4.5. FUTURE WORK

Attempts are underway to design and fabricate a new varactor grid that would match the gain curve of the HEMT grid discussed in Section 3.4. As shown in Fig. 3.28 this HEMT grid amplifier has gain in the range of 9 GHz to 10.5 GHz. The measurements with the varactor grid show a tuning range of 8.2 GHz to 9.5 GHz. The overlap between the amplifier gain and the varactor grid tuning range is only 500 MHz from 9 GHz to 9.5 GHz. The amplifier only has a gain of less than 3 dB in this range. To achieve favorable results from the new design this varactor grid has to have a tuning range from 9 GHz to 10.5 GHz, and the effect of the capacitors due to the fingers in each cell should not be ignored.

References

[1] Z.B. Popović, R.M. Weikle, M. Kim, D.B. Rutledge, "A 100-MESFET Planar Grid Oscillator," *IEEE Trans. Microwave Theory Tech.*, vol. 39, pp. 193–200, March 1990.

[2] R.M. Weikle, M. Kim, J.B. Hacker, M.P. De Lisio, D.B. Rutledge, "Planar MESFET Grid Oscillators Using Gate Feedback," *IEEE Trans. Microwave Theory Tech.*, vol. 40, pp. 1997–2003, Nov. 1992.

[3] M. Kim, E.A. Sovero, J.B. Hacker, M.P. De Lisio, J.J. Rosenberg, D.B. Rutledge, "A 6.5 GHz–11.5 GHz Source Using a Grid Amplifier with a Twist Reflector," *IEEE Trans. Microwave Theory Tech.*, vol. 41, pp. 1772–1774, October 1993.

[4] M. Kim, "Grid Amplifiers," Ph.D. Thesis, California Institute of Technology. Pasadena, CA, 1993.

[5] E. Hecht "Optics," pp. 301–303, Second Edition, Addison–Wesley, 1988.

[6] L.B. Sjogren, H–X.L. Liu, F. Wang, T. Liu, W. Wu, X–H. Qin, E. Chung, C.W. Domier, N.C. Luhmann, Jr., J. Maserjian, M. Kim, J. Hacker, D.B. Rutledge, L. Florez, J. Harbison, "Monolithic Millimeter–Wave Diode Array Beam Controllers: Theory and Experiment," *The 3rd Int. Symp. Space Terahertz Tech.*, pp. 45–57, Ann Arbor, Michigan, March 1992.

[7] W.W. Lam, C.F. Jou, H.Z. Chen, K.S. Stolt, N. C. Luhmann, Jr., D.B. Rutledge, "Millimeter-Wave Diode-Grid Phase Shifters," *IEEE Trans. Microwave Theory Tech.*, vol. 36, pp 902-907, May 1988.

[8] S. Bundy, T.B. Mader, Z.B. Popović, "Quasi-Optical Array VCO's," *1992 IEEE MTT-S Int. Microwave Symp.*, pp. 1539–1542, 1992.

[9] "HP 85180A High Frequency Structure Simulator," Hewlett-Packard, Networks Measurements Division, Santa Rosa, CA.

[10] R.M. Weikle, "Quasi-Optical Planar Grids for Microwave and Millimeter-Wave Power Combining," Ph.D. Thesis, California Institute of Technology. Pasadena, CA, 1992.

Chapter 5

Self-Complementary Grid Amplifiers

Using Babinet's principle, Booker presented a simple relationship between the impedances of two 1-port planar complementary structures [1]. In this chapter Deschamps's generalization to Booker's relation for an n-terminal planar structure is reviewed [2]. It is shown that Deschamps's generalization is also true for certain types of bounded structures. Based on this, an extension to Deschamps's theorem for 3-terminal, horizontally symmetrical, self-complementary, bounded structures is presented. It is shown that for these structures a simple relationship between the impedance parameters for the odd mode and the admittance parameters for the even mode exists, and that these modes are orthogonal. The motivation for this work in the design of new grid amplifiers is discussed, and the approach for using the properties of 3-terminal, horizontally symmetrical, self-complementary structures in designing grid amplifiers is presented. The design of a 16-element self-complementary MESFET grid amplifier is presented and suggestions for future improvements are discussed.

5.1. MOTIVATION

As discussed in earlier chapters, to first order, the unit cell of a grid determines the driving-point impedance seen by each device, while power scales with the grid area. This allows the reduction of the problem of the entire grid to that of a single unit cell. In Section 1.2 it is shown how symmetry of some grids allows boundary conditions to be imposed on a unit cell, thus reducing the

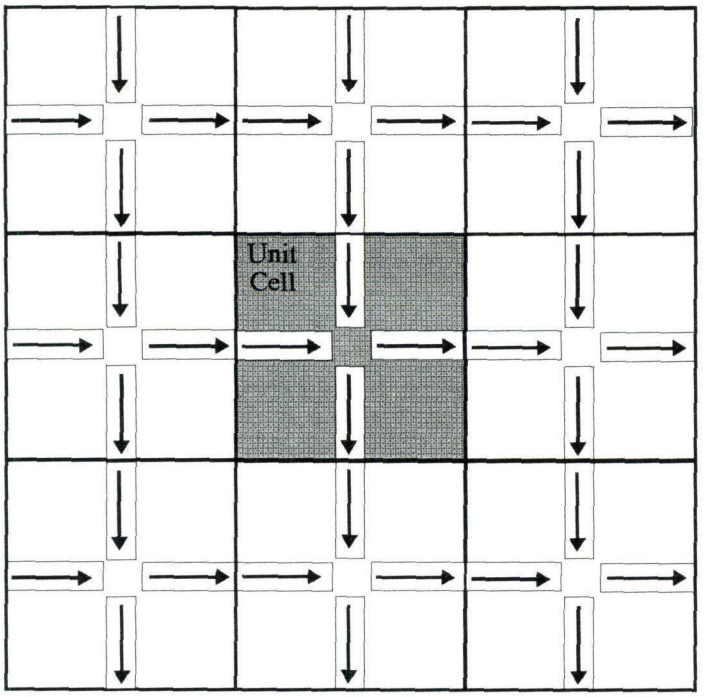

Figure 5.1. Current distribution on a conventional grid amplifier.

problem of solving for the cell to that of solving for a waveguide representing the cell. Fig. 5.1 shows the current distribution on a conventional grid amplifier. The current distribution on the grid does not allow either an E-wall or an H-wall to be imposed at the edges of the cell. Therefore, unlike many other grids, the fields for a grid amplifier cell cannot be easily solved using waveguide solutions. As a result of this, an approximate transmission-line equivalent circuit model was used to model the unit cell of the previous grid amplifiers [3]. Also, due to the use of crossed-dipole antennas for the input and output, these grids require differential-pair transistor chips as active devices [3,4]. The use of differential-pair chips requires the fabrication of custom-made transistor pairs.

Because of these constraints, it is desirable to investigate the possibility of a new design for a grid amplifier. This design should enable us to model the grids directly using microwave CAD tools. Also, a structure using single transistors as active devices for each unit cell is preferable. Similar to the previous grids,

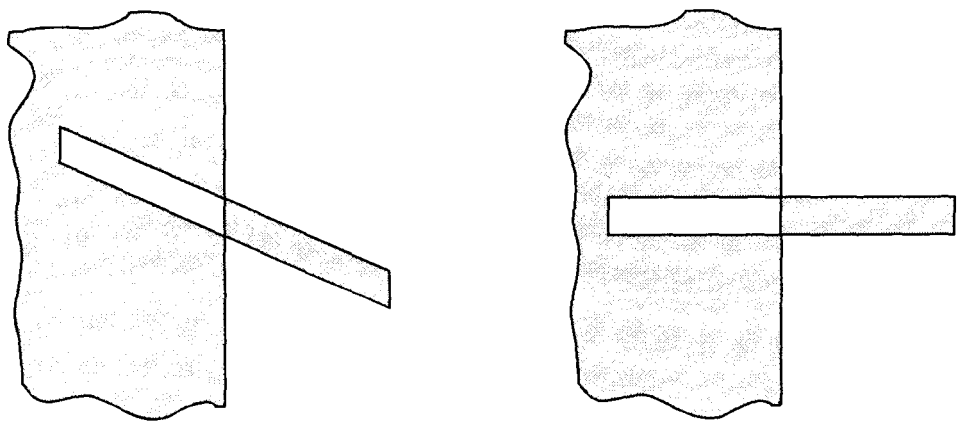

(a) (b)

Figure 5.2. (a) A self-complementary structure. (b) A self-complementary structure with horizontal symmetry.

the design goal is to use cross-polarized input and output beams to prevent the amplifier from oscillating. Self-complementary symmetrical structures offer the possibility of single transistor unit cells with orthogonal input and output.

5.2. PROPERTIES OF SELF-COMPLEMENTARY STRUCTURES

A self-complementary structure is one which looks the same when the metal part is exchanged with the non-metal part. Fig. 5.2 shows two self-complementary structures.

In a 1959 paper, Georges Deschamps presented the impedance properties of multiterminal complementary planar structures [2]. In this section the general form of Deschamps's solution for complementary structures is reviewed and the application of this solution to self-complementary bounded structures with horizontal symmetry is discussed. Fig. 5.2(b) is an example of a horizontally symmetrical self-complementary structure.

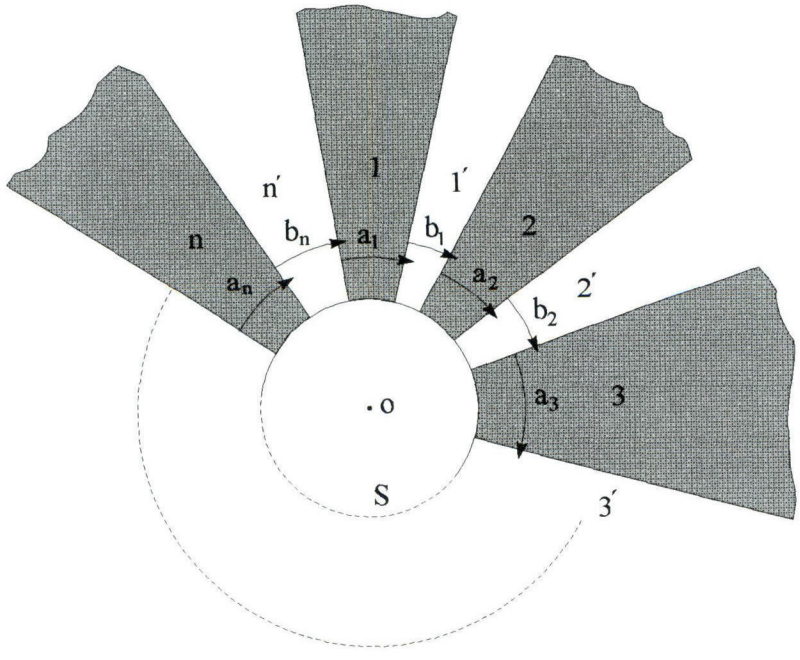

Figure 5.3. An n-terminal structure.

5.2.1. REVIEW OF DESCHAMPS'S THEOREM

Fig. 5.3 shows an n-terminal structure. Assume that a source inside S is connected to some or all of the terminals. The sphere S is small compared to the wavelength of operation. Using Deschamps's notation the integration paths $b_1, b_2, \ldots b_n$ are defined as paths from metal to metal and the paths $a_1, a_2, \ldots a_n$ are defined as integration paths from opening to opening. These paths terminate in the plane of the structure, but otherwise lie in a plane located an infinitesimal distance in front of this plane. The notation $c \cdot U$ is defined to indicate the integral:

$$c \cdot U = \int_c U \cdot ds. \tag{5.1}$$

Assume that $F = (E, H)$ is a field solution for this structure. In other words, F is a field produced about this structure by some configuration of sources inside S. Using the notation of (5.1) the voltage difference between terminals i and $i+1$ is:

$$V_i - V_{i+1} = b_i \cdot E \qquad i = 1, \ldots, n. \tag{5.2}$$

The current I_i flowing into terminal i is given by:

$$I_i = 2a_i \cdot H \qquad i = 1, \ldots, n. \tag{5.3}$$

Now consider the complementary structure of Fig. 5.3, obtained by replacing the metal parts of the original structure with free space and the apertures with metal. Deschamps showed that an acceptable solution for this structure is the dual of F. F' is defined to be the dual field:

$$F' = (E', H') = (-\eta_o H, \frac{1}{\eta_o} E), \tag{5.4}$$

where $\eta_o = 377\Omega$ is the characteristic impedance of free space.

To show that F' is a solution to the complement of the structure we proceed as follows:

First consider the uniqueness theorem. For linear, isotropic media specification of the boundary conditions is sufficient to specify fields uniquely within the region. Therefore two problems with the same boundary conditions will have identical solutions.

Now consider an arbitrary structure as in Fig. 5.4(a) with the assumed field solution F. Continuity of tangential electric field at a boundary requires that the surface tangential electric field be zero just outside the metal surface. Therefore, the E-fields at the plane of the structure approach the metal normal to its boundary and just above the structure the E-fields are normal to the plane of the structure.

The discontinuity in tangential magnetic field requires that the tangential magnetic field be perpendicular to the direction of the surface current and equal to the surface current density. Therefore, the H-fields are parallel to the plane of the structure above and below it and at the metal boundary the fields cross the plane of the structure normal to the surface.

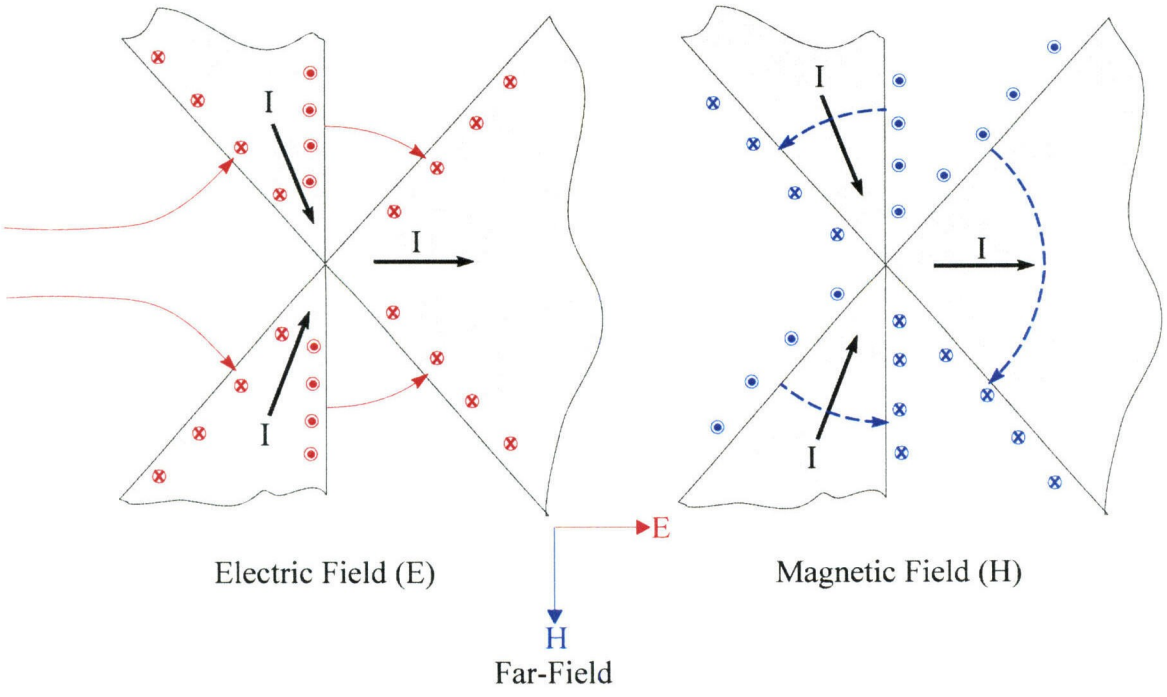

(a)

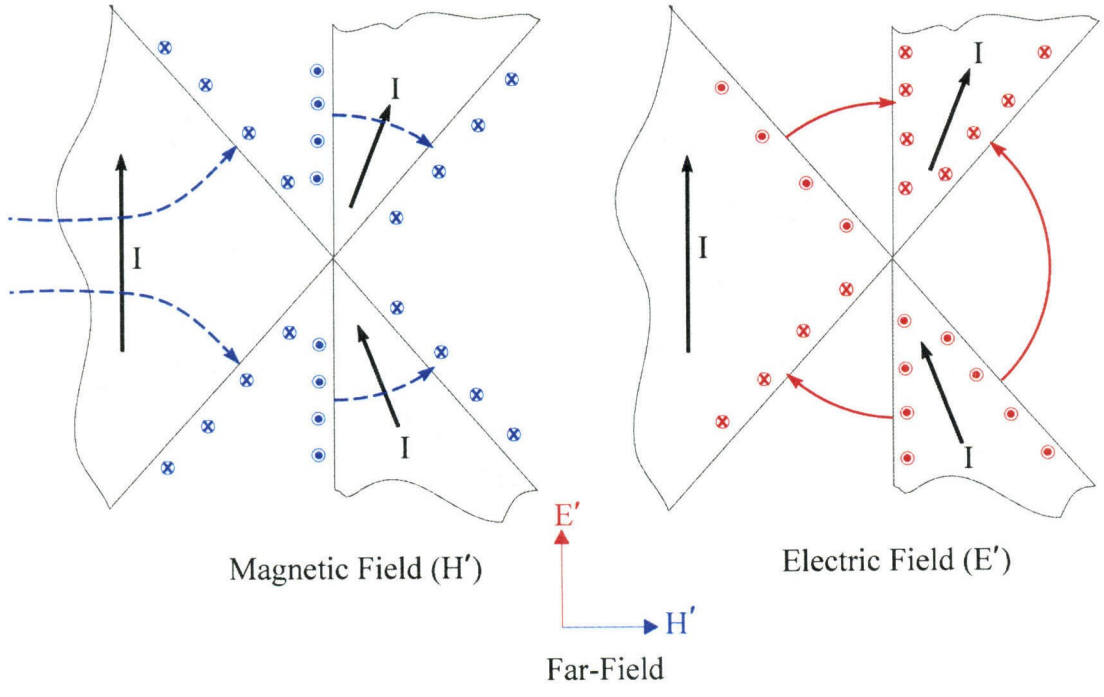

(b)

Figure 5.4. (a) Electric and magnetic fields for an arbitrary structure. (b) The electromagnetic fields for the complement of the structure in (a). The fields in (b) are the duals of the fields in (a).

The electric and magnetic fields about this planar structure are shown in Fig. 5.4(a) for the original structure and in Fig. 5.4(b) for the complementary structure. Note that the boundary conditions for the E-fields in Fig. 5.4(a) are similar to the H-field boundary conditions in Fig. 5.4(b). The same similarity exists between the H-field boundary conditions in Fig. 5.4(a) and the negative of the E-field boundary conditions in Fig. 5.4(b). It is clear that assuming F is the field solution for Fig. 5.4(a), F' (dual of F) not only satisfies Maxwell's equations but also satisfies the boundary conditions of the complementary structure shown in Fig. 5.4(b). Therefore, due to uniqueness theorem F' is the field solution for Fig. 5.4(b). In other words, the field solutions for the complement of a structure is equivalent to the field solution for the dual of that structure.

Similar relations to (5.2) and (5.3) exist for the field F' and the new structure:

$$I_i' = 2b_i \cdot H' \qquad i = 1, \ldots, n \tag{5.5}$$

$$V_i' - V_{i+1}' = a_{i+1} \cdot E' \qquad i = 1, \ldots, n, \tag{5.6}$$

where I_i' is the current flowing into terminal i' of the complementary structure, and $V_i' - V_{i+1}'$ is the voltage difference between terminals i' and $i' + 1$ of this structure.

Deschamps showed that the voltages and currents of the complementary structure can be defined using the voltages and currents of the original structure. This is accomplished by the use of (5.4) in (5.5) and (5.6), and solving the resulting equations with (5.2) and (5.3):

$$I_i' = \frac{2}{\eta_o}(V_i - V_{i+1}) \qquad i = 1, \ldots, n \tag{5.7}$$

$$V_i' - V_{i+1}' = -\frac{\eta_o}{2} I_{i+1} \qquad i = 1, \ldots, n. \tag{5.8}$$

5.2.2. AN EXTENSION TO DESCHAMPS'S THEOREM

This section discusses an extension of Deschamps's theorem for a horizontally symmetrical, 3-terminal (2 port) structure bounded with electric and magnetic walls (Fig. 5.5(a)). The motivation for this analysis is its application in the design and modelling of amplifier grid unit cells which will be discussed later. Assume that a source configuration at the terminals of the structure in Fig. 5.5(a) results in an odd-mode excitation. An odd-mode excitation is defined as the mode where equal voltages with opposite polarity appear at ports 1 and 2 of the structure as shown in Fig. 5.5(a). These two ports are shown with black dots in the figure. This odd-mode excitation for a single-mode (TEM) structure generates a vertically polarized electric field (E_V) at the far-field. The complement of this structure is shown in Fig. 5.5(b). As discussed in Section 5.2.1, boundary conditions for the complement of a planar structure are the duals of the boundary conditions for the original structure. To use Deschamps's theorem for a bounded structure, the E and H-walls of the original structure must be changed to their duals when complementing the structure. Since the dual of an H-wall is an E-wall and vice versa, this is equivalent to interchanging E and H-walls. Fields in Fig. 5.5(b) have to be the duals of the fields in Fig. 5.5(a), therefore the far-field electric field for the new structure is horizontally polarized (E_H) and the excitation generating it is an even-mode excitation as shown in Fig. 5.5(b). An even-mode excitation is defined as the mode where equal voltages with the same polarity appear at ports 1 and 2 of the structure. These ports are also shown with black dots.

As presented in Section 1.2, bounding a planar structure with electric and magnetic walls is equivalent to analyzing this structure inside a waveguide with the same E and H-walls [5]. Figs. 5.6(a) and 5.6(b) show the waveguide representation of the structures in Figs. 5.5(a) and 5.5(b). We define port 1 of Fig. 5.6(a) as the series combination of ports 1 and 2 in Fig. 5.5(a), and port 1 in Fig. 5.6(b)

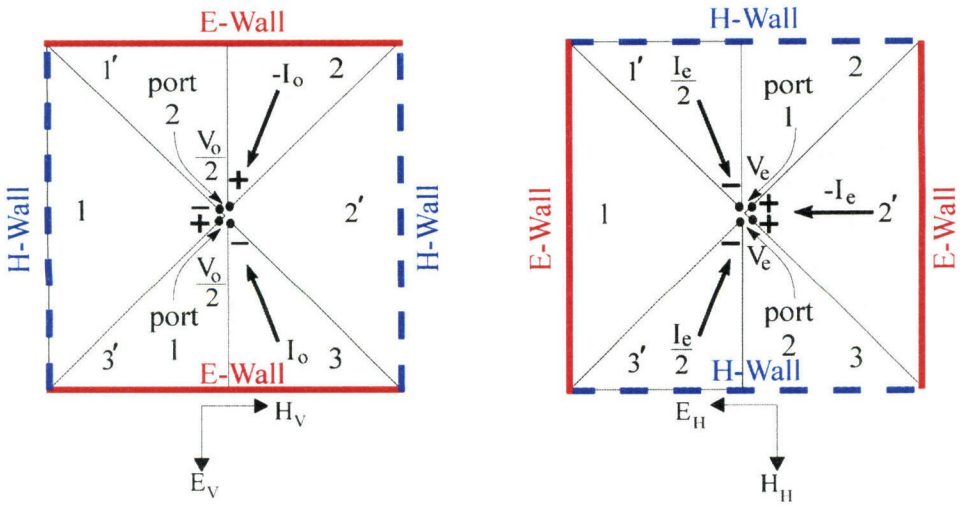

Figure 5.5. A horizontally symmetrical, self-complementary structure. (a) Odd excitation. (b) Even excitation.

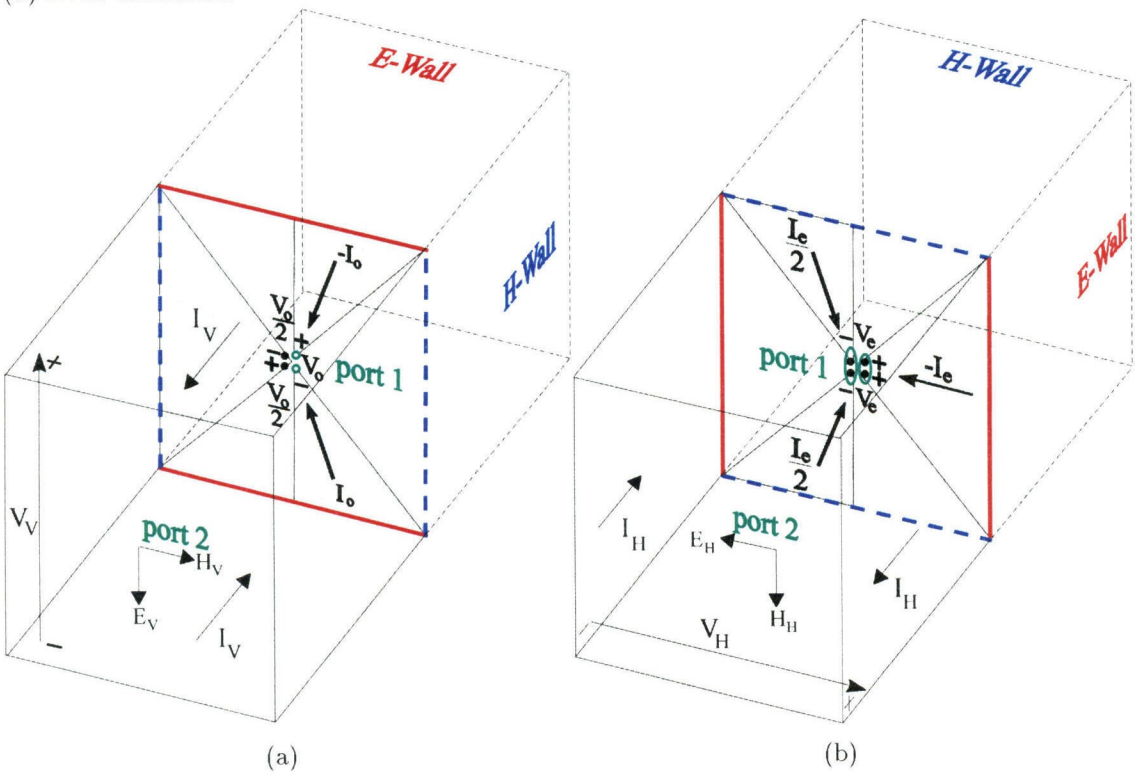

Figure 5.6. Waveguide representation of Fig. 5.5. (a) Odd mode. Port 1 is the series combination of the ports in Fig. 5.5(a), shown by two hollow dots. (b) Even mode. Port 1 is the parallel combination of the ports in Fig. 5.5(b), shown by two ovals. Port 2 in (a) and (b) is the parallel combination of the two ports of the waveguide.

as the parallel combination of these ports in Fig. 5.5(b). Two hollow dots in Fig. 5.6(a) and two ovals in Fig. 5.6(b) show port 1. For the remainder of this chapter we will refer to port 1 of Figs. 5.6(a) and 5.6(b) as the odd and even-mode device ports. The waveguides in Figs. 5.6(a) and 5.6(b) extend to both sides of the self-complementary structures. However, due to reciprocity and to simplify the analysis of this 3-port structure these parallel ports are combined into one port. The new port (port 2 in Figs. 5.6(a) and 5.6(b)) has half the characteristic impedance of free space. For the remainder of this discussion we will refer to the parallel combination of these two ports as the waveguide port. The purpose of this section is to find equations relating the equivalent circuits of the 2-port waveguide structures shown in Figs. 5.6(a) and 5.6(b).

Consider the odd-mode excitation of this horizontally symmetrical, self-complementary structure inside the waveguide (Fig. 5.6(a)). This odd-mode excitation at the device port generates a vertically polarized electric field (E_V) at the waveguide port. Also assume that this two-port structure is represented by a T-equivalent circuit. The components of this T-circuit are related to the Z-parameters of the structure as shown in Fig. 5.7(a). This T-equivalent circuit relates the odd-mode voltage and current (V_o and I_o) at the device port to the waveguide port voltage and current (V_V and I_V). These voltages and currents are shown in Fig. 5.6(a).

Now consider the even-mode excitation for the same structure (Fig. 5.6(b)), which generates fields with horizontally polarized E-field (E_H) at the waveguide port. Even-mode excitation of this structure is equivalent to complementing the structure shown in Fig. 5.6(a). Since this is a self-complementary structure complementing it does not change the structure, instead it changes the odd excitation to even excitation. A Π-equivalent circuit as shown in Fig. 5.7(b) is used to represent the new structure. The relation between the components of this circuit to the Y-parameters of the structure is also shown in this figure. This

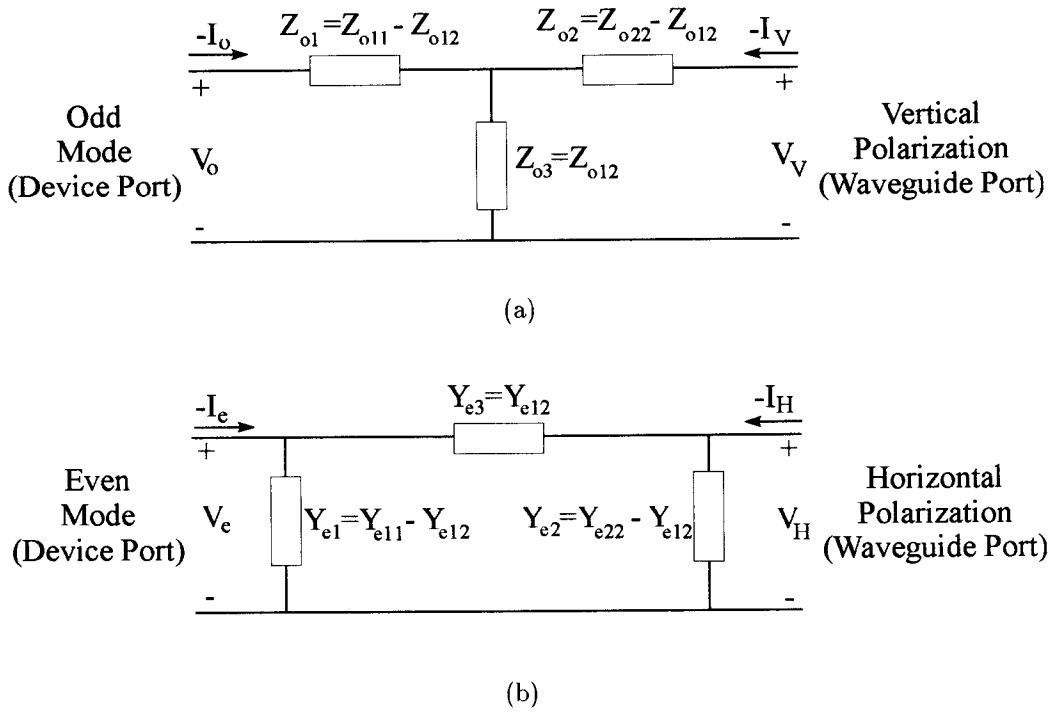

Figure 5.7. (a) The T-equivalent circuit for the structure with odd-mode excitation. Z_{o11}, Z_{o12}, and Z_{o22} are the Z-parameters of this structure. (b) The Π-equivalent circuit for the even-mode excitation. Y_{e11}, Y_{e12}, and Y_{e22} are the Y-parameters of the structure. Due to reciprocity $Z_{o12} = Z_{o21}$ and $Y_{e12} = Y_{e21}$.

Π-circuit relates the device port even-mode voltage and current (V_e and I_e) to the voltage and current at the waveguide port (V_H and I_H) shown in Fig. 5.6(b).

The remainder of this section explains the relations between components of the T-equivalent circuit and the Π-equivalent circuit for odd and even excitation of a horizontally symmetrical, self-complementary structure. To achieve this we start by finding relations between the Z-parameters of this structure for the odd excitation and the Y-parameters for the even excitation.

Using (5.7) and (5.8) for the structures in Figs. 5.5(a) and 5.5(b) and using a numbering scheme similar to Fig. 5.3 we have:

$$I_o = -\frac{2}{\eta_o} V_e \tag{5.9}$$

$$V_o = -\frac{\eta_o}{2} I_e, \tag{5.10}$$

where I_o and V_o are the odd-mode current and voltage as shown in Fig. 5.5(a) and I_e and V_e are the even-mode current and voltage as shown in Fig. 5.5(b).

Using (5.9) and (5.10):

$$\frac{V_o}{I_o} = \frac{\eta_o^2}{4} \cdot \frac{I_e}{V_e}. \tag{5.11}$$

Using Fig. 5.7 the ratio of the device port impedance for the odd excitation (Fig. 5.7(a)) to the device port admittance for the even excitation (Fig. 5.7(b)) when the waveguide ports are terminated to $\eta_o/2$ is:

$$\frac{V_o/I_o}{I_e/V_e} = \frac{Z_{o11} - \dfrac{Z_{o12}^2}{\eta_o/2 + Z_{o22}}}{Y_{e11} - \dfrac{Y_{e12}^2}{2/\eta_o + Y_{e22}}}, \tag{5.12}$$

where Z_{o11}, Z_{o12}, and Z_{o22} are the Z-parameters of the structure with odd-mode excitation and Y_{e11}, Y_{e12}, and Y_{e22} are the Y-parameters of the structure with even-mode excitation. Terminating the waveguide port to $\eta_o/2$ is equivalent to terminating the two ports of the waveguide in Fig. 5.6(a) or Fig. 5.6(b) to the characteristic impedance of free space.

Using the notation in (5.1) the voltage and current at the waveguide port of Fig. 5.6(a) is given by:

$$V_V = -A \cdot E_V \tag{5.13}$$

$$I_V = 2A \cdot H_V, \tag{5.14}$$

where A is the dimension of the waveguide on the side, E_V and H_V are the waveguide port (port 2 in Fig.5.6(a)) electric and magnetic fields, V_V is the waveguide port voltage, and I_V is the current flowing in the E-walls of the waveguide port.

The voltage and current in the waveguide port of Fig. 5.6(b) is similarly given by:

$$V_H = -A \cdot E_H \tag{5.15}$$

$$I_H = 2A \cdot H_H, \tag{5.16}$$

where E_H and H_H are the electric and magnetic fields at the waveguide port, V_H is the voltage between the E-walls of the waveguide port, and I_H is the E-wall current of the same port.

Now consider shorting the device port in Fig. 5.6(a). In order for Fig. 5.6(b) to remain the complement of Fig. 5.6(a) the device port in Fig. 5.6(b) has to be an open. Fields at the waveguide port of Fig. 5.6(a) are related to the waveguide port fields of Fig. 5.6(b) by (5.4):

$$(E_H, H_H) = (-\eta_o H_V, 1/\eta_o E_V). \tag{5.17}$$

Using (5.13) to (5.16) and the relationship between the magnitude of (E_H, H_H) and the magnitude of (E_V, H_V) from (5.17):

$$\frac{\frac{V_V}{I_V}\Big|_{V_o=0}}{\frac{I_H}{V_H}\Big|_{I_e=0}} = \frac{\eta_o^2}{4}. \tag{5.18}$$

The same approach can be used when the device port in Fig. 5.6(b) is shorted. In this case the device port in the complementary structure (Fig. 5.6(a)) has to be an open circuit. Similarly we can derive:

$$\frac{\frac{V_H}{I_H}\Big|_{V_e=0}}{\frac{I_V}{V_V}\Big|_{I_o=0}} = \frac{\eta_o^2}{4}. \tag{5.19}$$

From the circuits in Fig. 5.7 we can also derive:

$$\frac{\frac{V_H}{I_H}\Big|_{V_e=0}}{\frac{I_V}{V_V}\Big|_{I_o=0}} = \frac{Z_{o22}}{Y_{e22}} \tag{5.20}$$

$$\frac{\frac{V_V}{I_V}\Big|_{V_o=0}}{\frac{I_H}{V_H}\Big|_{I_e=0}} = \frac{Z_{o22} - Z_{o12}^2/Z_{o11}}{Y_{e22} - Y_{e12}^2/Y_{e11}}. \tag{5.21}$$

From (5.19) and (5.20):

$$\frac{Z_{o22}}{Y_{e22}} = \eta_o^2/4. \tag{5.22}$$

Solving for (5.11), (5.12), (5.18), (5.21), and (5.22) we can derive:

$$\frac{Z_{o12}}{Y_{e12}} = \eta_o^2/4 \tag{5.23}$$

$$\frac{Z_{o11}}{Y_{e11}} = \eta_o^2/4. \tag{5.24}$$

To summarize, equations (5.22) to (5.24) simply indicate that the Z-parameters of a horizontally symmetrical, self-complementary structure with odd-mode excitation is related to the Y-parameters of the same structure with even-mode excitation by:

$$\frac{Z_{oij}}{Y_{eij}} = \eta_o^2/4 \qquad i = 1,2 \ ; \ j = 1,2. \tag{5.25}$$

Using (5.25) and Fig. 5.7 the impedances of the T-equivalent circuit components (Z_{o1}, Z_{o2}, Z_{o3}) for the odd-mode excitation and the admittances of the Π-circuit components (Y_{o1}, Y_{o2}, Y_{o3}) for the even-mode excitation are also related by:

$$\frac{Z_{oi}}{Y_{ei}} = \eta_o^2/4 \qquad i = 1, \ldots, 3. \tag{5.26}$$

5.3. SELF-COMPLEMENTARY GRID AMPLIFIER MODELLING

This section discusses the design and modelling of grid amplifiers with self-complementary, horizontally symmetrical unit cells. Consider the self-complementary grid amplifier configuration shown in Fig. 5.8(a). Since the dual of a dielectric is a magnetic material which does not exist in nature, to make the active grid a self-complementary structure we cannot build the grid on a dielectric

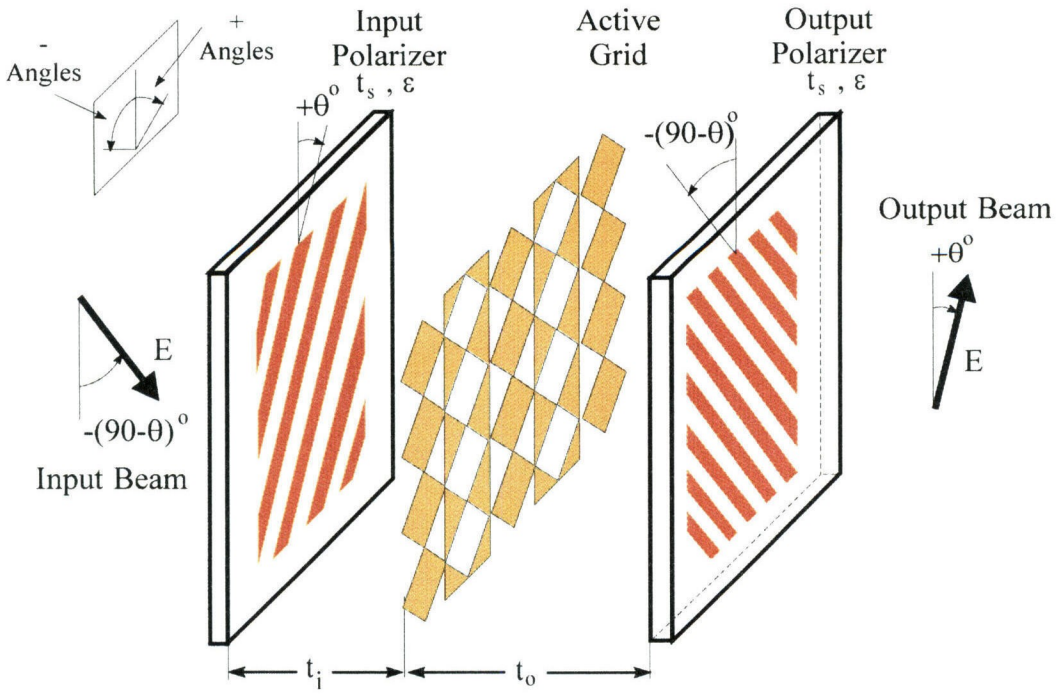

(a)

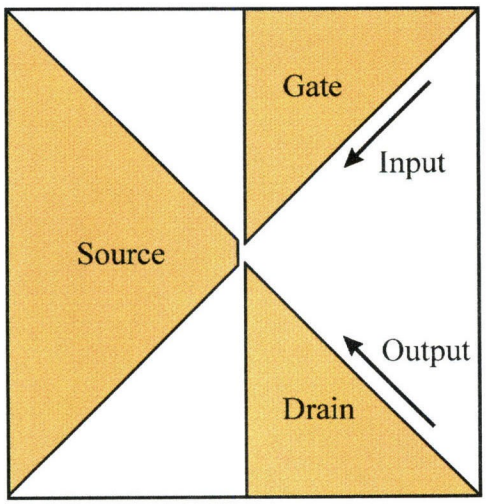

(b)

Figure 5.8. Simplified self-complementary grid amplifier. (a) Perspective view. (b) Unit cell.

material. Therefore we assume that the grid is suspended in free space. In practice this is achieved by constructing the grid on a very thin substrate with a low dielectric constant. The input and output polarizers are metallic gratings built on dielectric substrates with thickness t_s and a relative dielectric constant of ϵ, placed a distance t_i and t_o from the grid. The input polarizer metal strips are θ degrees from the vertical. To keep the input and output signals orthogonal, the output polarizer strips are positioned at an angle of $-(90-\theta)$ degrees from the vertical. A sample unit cell which is a less complicated version of the cell used in the construction of the grid is shown in Fig. 5.8(b). Unlike the previous grid amplifiers, this design allows the use of single transistors in each unit cell. The input signal that is incident from the left enters the tilted input polarizer normal to its strips and generates RF currents on the input gate leads of the grid (Fig. 5.8(a)). Currents on the output drain leads generate an output signal that passes through the output polarizer. Similar to the conventional grid amplifiers, the polarizers provide tuning of the amplifier's input and output circuits.

The solution for a self-complementary grid amplifier can be divided into solving for the odd and even-mode excitations. Figs. 5.9(a) and 5.9(b) show the odd and even excitations for part of a self-complementary grid. For each excitation the current distribution on the grid allows us to define boundary conditions as shown in Figs. 5.9(a) and 5.9(b). As will be discussed later, CAD analysis is only possible for the odd-mode excitation, Fig. 5.9(a). The approach presented in this section is to analyze the odd-mode excitation of the symmetrical self-complementary unit cell using Hewlett-Packard High Frequency Structure Simulator (HFSS) [5], and derive the equivalent T-circuit. The even-mode Π-equivalent circuit can then be calculated using (5.26). By combining the odd and even-mode equivalent circuits the model for the entire cell can be derived.

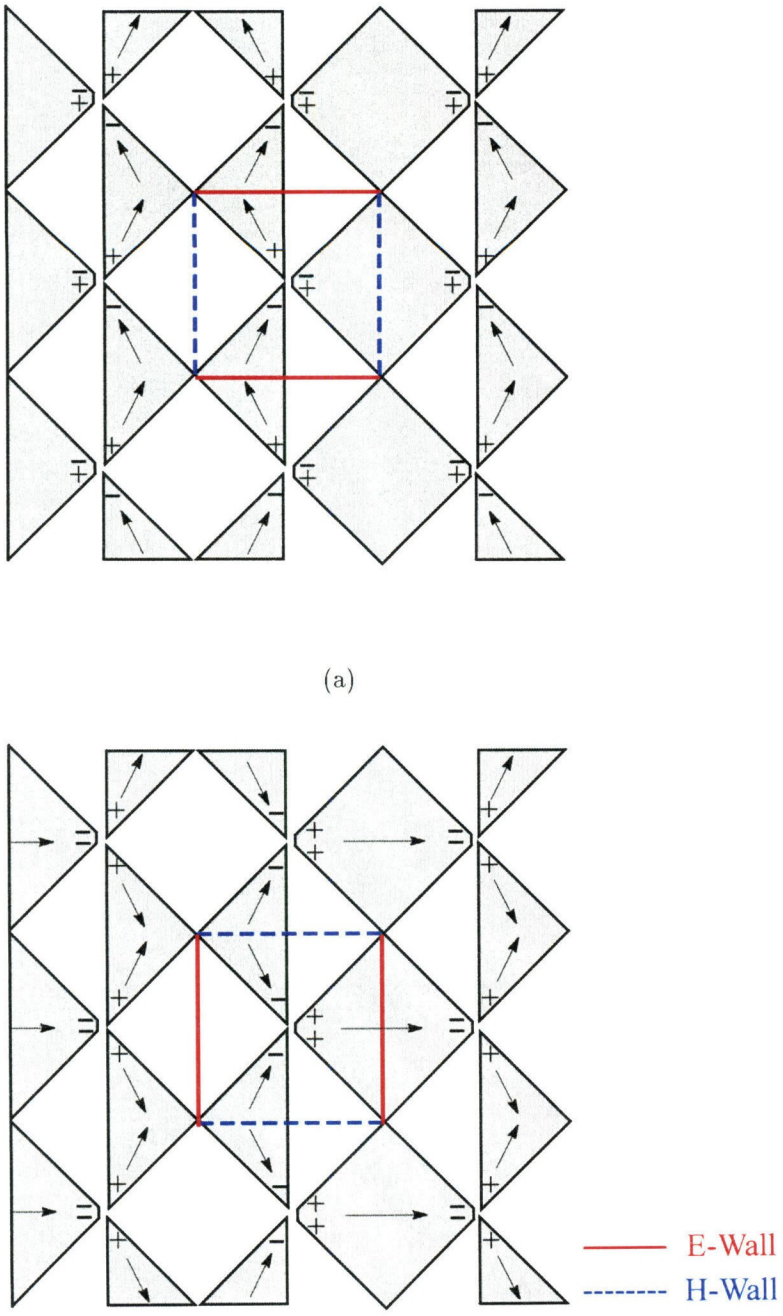

(a)

(b)

Figure 5.9. (a) Odd-mode excitation of a self-complementary grid amplifier. (b) Even-mode excitation of the same structure. Due to the symmetry of the current distribution E and H-walls can be defined for a unit cell.

5.3.1. ODD AND EVEN-MODE CIRCUIT EXTRACTION

To simulate equivalent waveguide structures shown in Figs. 5.6(a) and 5.6(b) it is necessary to excite the internal port 1 shown in these figures. Because of the symmetry of the unit cell this port can be excited by simulating half of the unit cell and connecting a small piece of a coaxial transmission line to this port. Fig. 5.10 shows this approach for the odd-mode excitation of the unit cell. This technique is not applicable to the even excitation of the cell, because for the even mode the waveguide wall at the device port is a magnetic wall and there is no convenient way of inserting a coaxial transmission line at this wall. The 3-port waveguide structure shown in Fig. 5.10 is used for HFSS modelling. Ports

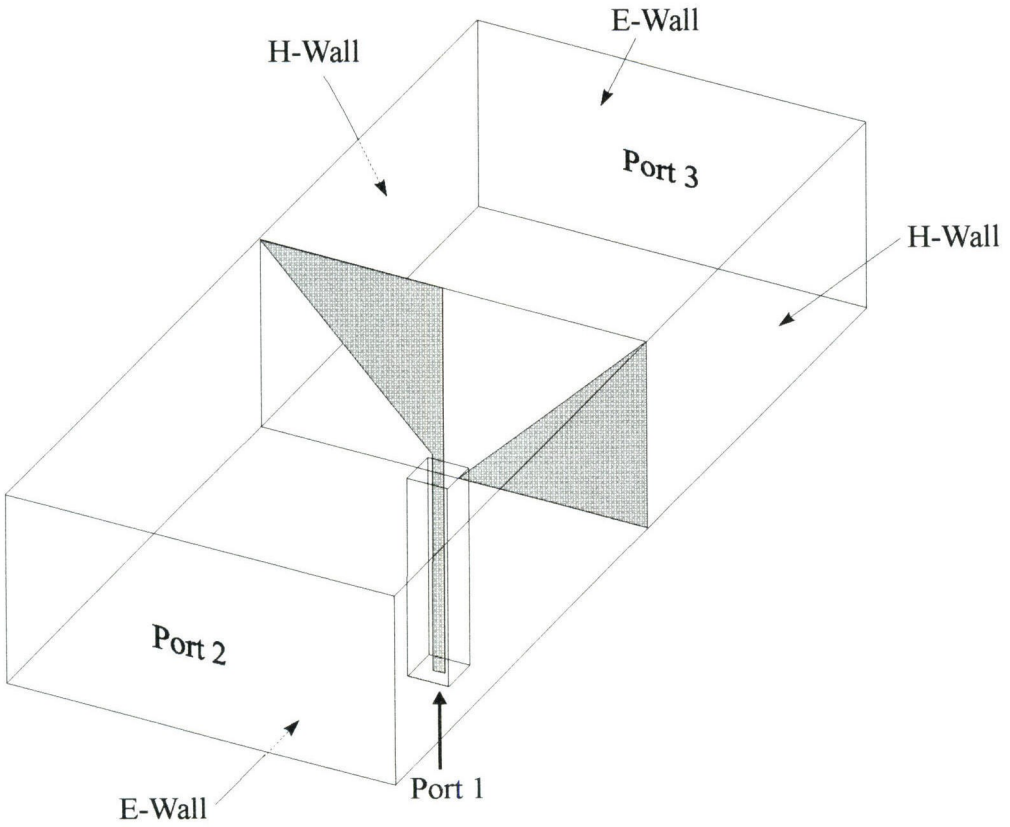

Figure 5.10. Layout of the HFSS half cell used in simulating the odd-mode excitation of the grid unit cell. The coaxial stub used to get access to the internal port of the grid is de-embedded from the final S-parameter file.

2 and 3 are the front and the back of the grid, and port 1 is the internal port on the grid unit cell where the transistor will be attached. The electric and magnetic walls of the waveguide are shown in the figure. The outer walls of the coaxial transmission line are all electric walls. The coaxial transmission line is de-embedded from the final S-parameters.

Due to reciprocity the 3×3 scattering matrix resulting from the HFSS simulation is:

$$S_{3\times3} = \begin{pmatrix} s_{11} & s_{12} & s_{12} \\ s_{12} & s_{22} & s_{23} \\ s_{12} & s_{23} & s_{22} \end{pmatrix}. \tag{5.27}$$

We can combine ports 2 and 3 of Fig. 5.10 and reduce this 3×3 matrix to a 2×2 matrix given by:

$$S_{2\times2} = \begin{pmatrix} s_{11} & \sqrt{2}s_{12} \\ \sqrt{2}s_{12} & 1 + 2s_{22} \end{pmatrix}. \tag{5.28}$$

The port impedance of the combined ports is half the impedance of port 2 and 3 alone.

The Z-parameters of this structure can be calculated from the S-parameters given in (5.28). These Z-parameters are used to calculate the impedances of the components in the T-equivalent circuit as shown in Fig. 5.7(a). Note that the full-cell T-circuit has impedances twice that of the half-cell equivalent circuit. The admittances of the full-cell Π-equivalent circuit shown in Fig. 5.7(b) are derived using (5.26) and the impedances of the T-circuit.

5.3.2. COMBINING THE ODD AND EVEN-MODE CIRCUITS

The equivalent circuit model for the amplifier unit cell is derived by combining the odd and even-mode equivalent circuits. Defining ports 1 and 2 as shown in Figs. 5.11(a) and 5.11(b), port 3 as the odd mode, and port 4 as the even

mode, a four port lossless mode-converter is defined. Fig. 5.11(a) shows that an odd excitation with a voltage of V_o at port 3 of this device should generate voltages equal to $V_o/2$ and $-V_o/2$ at ports 1 and 2. As shown in Fig. 5.11(b) an even excitation with a voltage of V_e at port 4 should generate voltages equal to V_e at ports 1 and 2. To achieve equal voltages at both ports, a lossless mode-converter has to have a $1/\sqrt{2}$ transmission from ports 3 and 4 to 1 and 2 and vice versa. Choosing the proper phase for these transmission coefficients insures that signals at proper ports have the desired polarity. This 4-port S-matrix is defined by:

$$S = \begin{pmatrix} 0 & 0 & 1/\sqrt{2} & 1/\sqrt{2} \\ 0 & 0 & -1/\sqrt{2} & 1/\sqrt{2} \\ 1/\sqrt{2} & -1/\sqrt{2} & 0 & 0 \\ 1/\sqrt{2} & 1/\sqrt{2} & 0 & 0 \end{pmatrix}. \tag{5.29}$$

This mode-converter by itself does not result in the proper voltages described earlier. According to the mode-converter defined in (5.29) an even excitation with

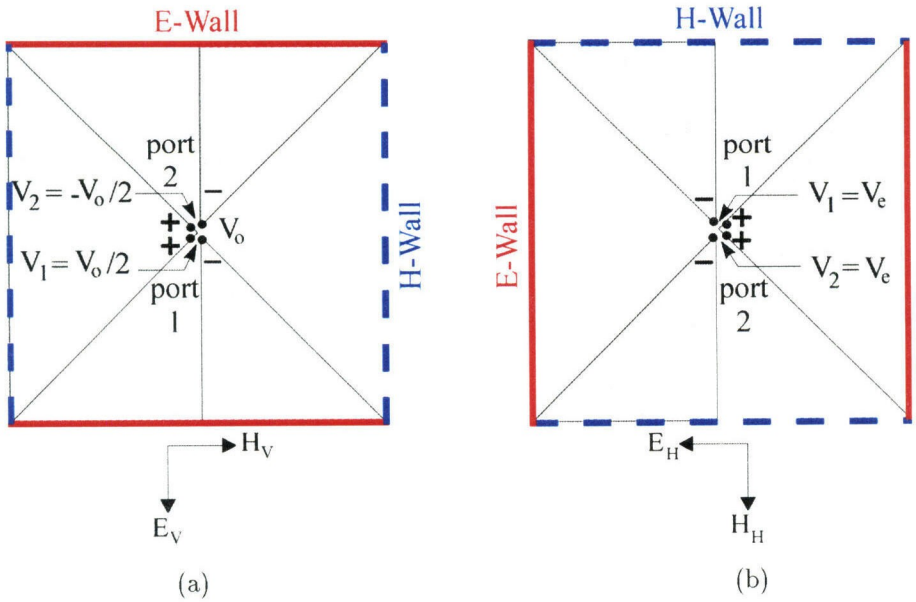

Figure 5.11. Mode-converter port definition. Port one and two are shown in the figures. Port 3 and 4 are the odd and even-mode ports. (a) The odd-mode excitation. (b) The even-mode excitation.

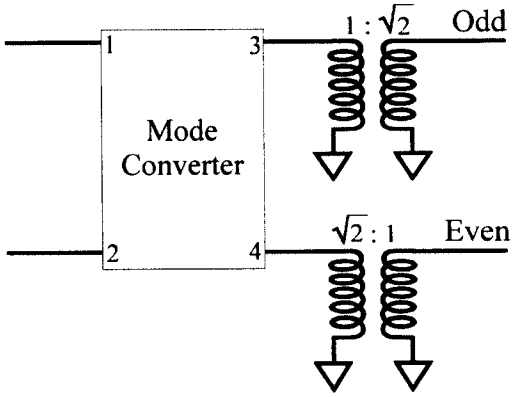

Figure 5.12. The circuit for combining the odd and even modes. It consists of a mode-converter as defined in (5.29) and two transformers.

a voltage of V_e at port 4 results in voltages equal to $V_e/\sqrt{2}$ at ports 1 and 2. However, according to Fig. 5.11(b) voltages at ports 1 and 2 have to be equal to V_e. To make a correction for this error a transformer at port 4 of the mode-converter increases the voltage level of the incoming signal by a factor of $\sqrt{2}$ before it enters the mode-converter. A similar correction is needed for the odd mode. Instead of generating voltages equal to $V_o/2$ and $-V_o/2$ at ports 1 and 2 for an odd excitation of V_o at port 3, the mode-converter generates voltages of $V_o/\sqrt{2}$ and $-V_o/\sqrt{2}$ at these ports. Therefore a transformer at port 3 decreases the voltage of the signal by a factor of $\sqrt{2}$ before it enters port 3. The mode-converter and the transformers are shown in Fig. 5.12. This is the device used to combine the odd and even-mode equivalent circuits to model the unit cell.

5.3.3. AMPLIFIER GRID EQUIVALENT CIRCUIT

Fig. 5.13 shows the transmission-line equivalent circuit for the amplifier configuration of Fig. 5.8. Free space for this square unit cell is represented by a resistor with a characteristic impedance of $\eta_o = 377\,\Omega$. The transmission-line representation of the dielectric substrates and air gaps between them are similar to the discussion in Section 3.2 and will not be repeated here. The polarizers are considered to be perfect and are modelled as a short for a wave polarized along

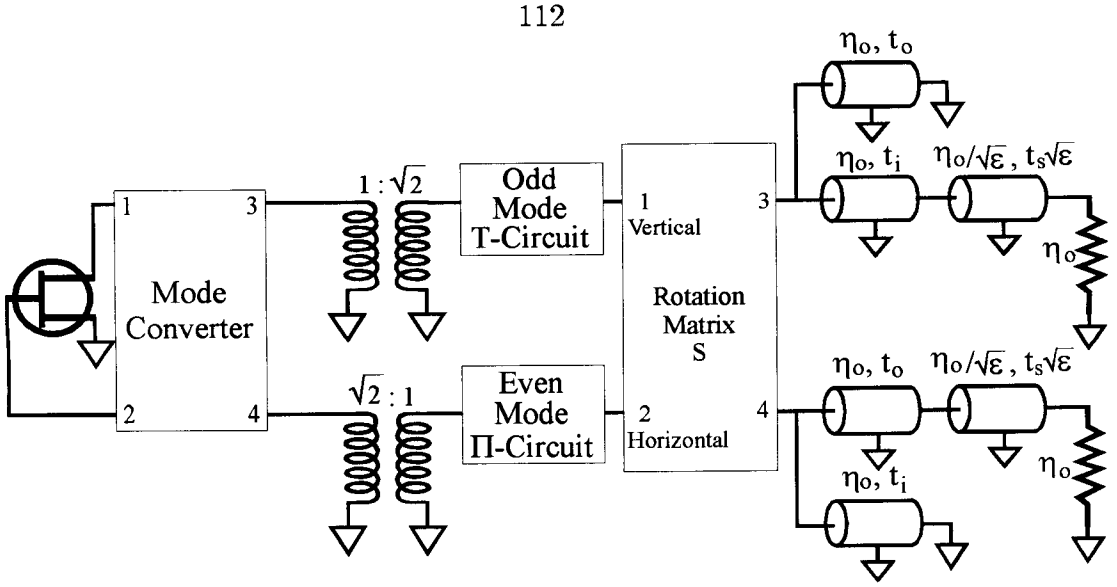

Figure 5.13. Equivalent circuit for the amplifier configuration shown in Fig. 5.8.

the direction of the metal strips and an open for a wave polarized orthogonal to the strips. A rotation transformation matrix is defined to separate the incoming signal to its vertical and horizontal components, and also to combine the vertical and horizontal components of the outgoing signal to form the output. The four ports of this rotation matrix are the vertical and horizontal polarizations for ports 1 and 2, and the input and output signals to the grid amplifier for ports 3 and 4. The S-matrix is defined by:

$$S = \begin{pmatrix} 0 & 0 & -\sin\theta & \cos\theta \\ 0 & 0 & \cos\theta & \sin\theta \\ -\sin\theta & \cos\theta & 0 & 0 \\ \cos\theta & \sin\theta & 0 & 0 \end{pmatrix}, \tag{5.30}$$

where θ is the output signal angle from the vertical as shown is Fig. 5.8(a).

The vertical component of the input signal is connected to the odd-mode T-equivalent circuit of the unit cell, and the horizontal component of the input excites the even-mode Π-equivalent circuit. The even and odd modes are then combined using the mode-converter and the transformers. The transistor assumed to be a FET is connected to ports 1 and 2 of the mode-converter.

5.4. AMPLIFIER DESIGN AND CONSTRUCTION

Using the approach discussed in Section 5.3 different self-complementary unit-cell configurations were analyzed using HFSS and the equivalent circuit in Fig. 5.13. Different input polarization angles for each of these grid designs were also considered. Fig. 5.14 shows the X-band design that was implemented. The unit cell is a self-complementary structure only if it is suspended in free space. Therefore this grid is built on a 10-mil-thick Duroid substrate with a relative dielectric constant of 2.2. The unit cell shown in Fig. 5.14(a) is 8 mm on a side. The input beam is coupled to the gate of the transistor through the gate lead and the output is radiated from the drain lead, orthogonal to the input. In order to provide bias to the transistors a double-sided design is used. The source leads in each column are connected to each other and biased from the front of the grid. A wire bond connects each drain lead to a via-hole that is connected to the back side of the grid. The drain bias leads in one column are connected to each other and biased at the back side of the grid. Each gate is shorted to the source through a bond wire. The inductance of the gate and drain bond wires are important in the design of the grid and will be discussed later. To DC isolate the gate of one cell from the drain of the cell below, a 0.15-mm-slot is used to separate the two. Three 20-pF chip capacitors shown in Fig. 5.14(a) are used to make an RF connection between the gate and drains of neighboring cells. The transistors are Fujitsu FLK012XP MESFET's. Fig. 5.14(b) shows how the unit cells are connected to construct a 4×4 grid and does not include the details of each cell. Each arrow in this figure points to the location of the transistor in a unit cell. The transistors are glued on the source lead and connections to the gate, drain and the source are made with wire bonds.

Instead of the unit cell in Fig. 5.14(a) a simpler structure similar to the unit cell in Fig. 5.8(b) was used for HFSS modelling of this cell. A 3-port structure similar to Fig. 5.10 was used for simulating half the unit cell. The coaxial

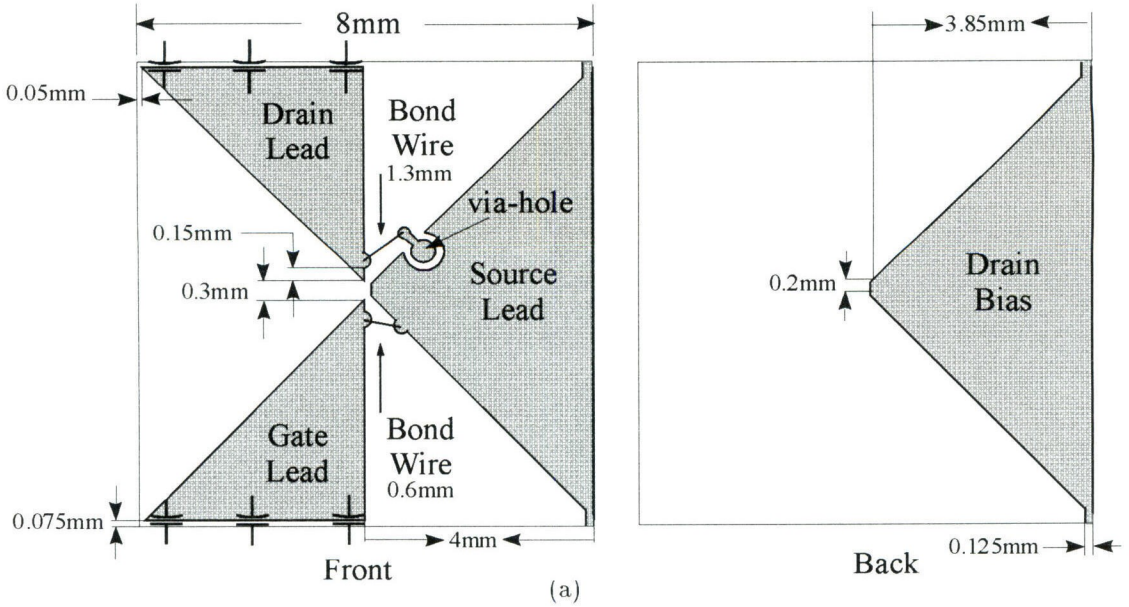

(a)

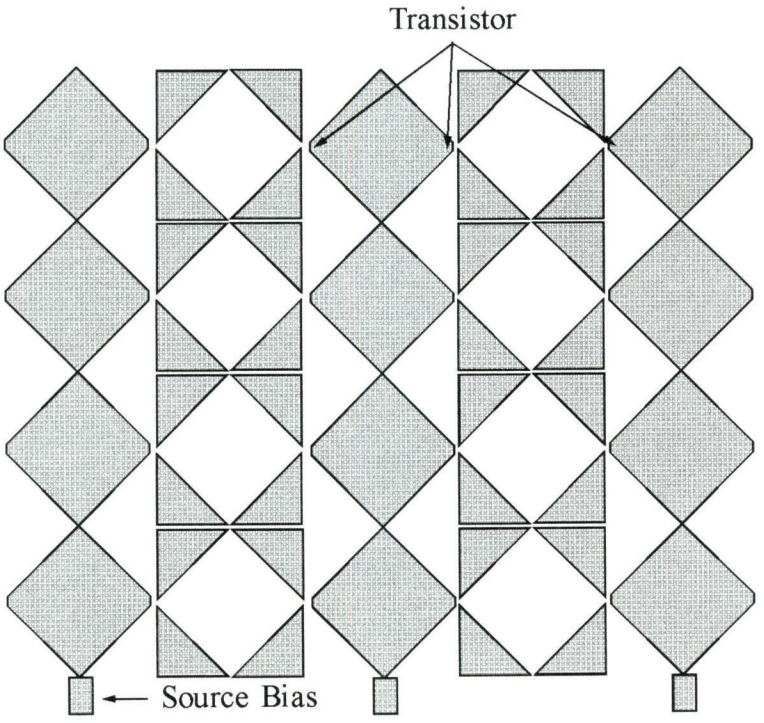

(b)

Figure 5.14. (a) Front and back side of the grid amplifier unit cell. (b) Front view of a 4×4 grid amplifier. The drains are biased from the back side.

transmission line used in this simulation has a square cross section of 0.75 mm and length of 4 mm. The inner conductor of the coaxial transmission line is 0.25-mm wide. A simulation over the frequency range of interest results in an S-matrix similar to (5.27). Post-processing on this S-matrix removes the effect of the transmission-line pieces at each port and normalizes the S-parameters to a convenient impedance. A 2×2 S-matrix representing the odd mode of the unit cell is calculated using this S-matrix and (5.28). The odd-mode Z-parameter matrix is calculated and the even-mode Y-parameter matrix is derived by the use of (5.25). The even-mode S-matrix is calculated from this Y-matrix. Instead of equivalent T and Π-circuits for odd and even modes the odd and even-mode S-parameter matrices are used for simulating the grid. Since the entire unit cell is modelled, the normalizing impedance of 377 Ω is used for the odd and even-mode S-matrices.

Fig. 5.15 shows the amplifier assembly and its equivalent circuit for the proposed design. The dotted rectangle in Fig. 5.15(b) is the passive metal structure of the amplifier unit cell discounting the bond wires shown in Fig. 5.14(a). The input signal enters port $3'$ and the output exits from $4'$. Port $2'$ is connected to the gate of the transistor and the drain is attached to $1'$. For the amplifier to work properly, the transmission coefficients from the input to the gate ($S_{2'3'}$) and the drain to the output ($S_{4'1'}$) have to be large, and the transmission coefficients from the input to the drain ($S_{1'3'}$) and gate to the output ($S_{4'2'}$) have to be small. An equal resistive load at ports $1'$ and $2'$ is found to be the optimum load for accomplishing this. Therefore, bond wires at the gate and the drain of the FET are used to resonate with the input and output capacitance of the FET and present a resistive load at ports $1'$ and $2'$ of the unit cell. The measured inductance of a bond wire with a diameter of 0.7 mil is 1 nH/mm. The required inductance of 1.3 nH and 0.6 nH is achieved by adding 1.3-mm and 0.6-mm bond wires at the drain and the gate of the unit cell respectively. Different angles for

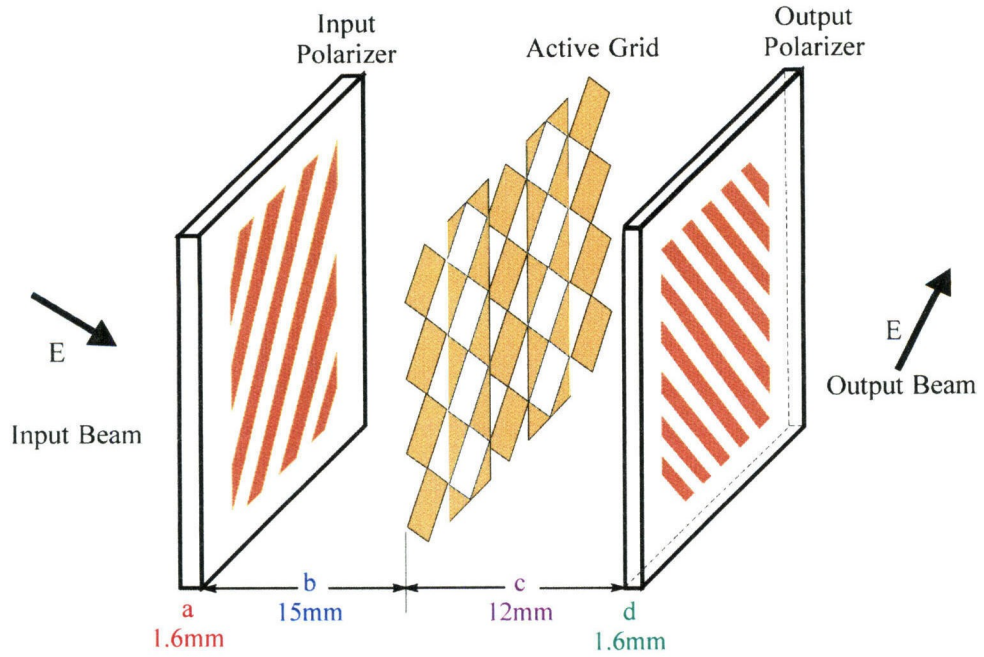

(a)

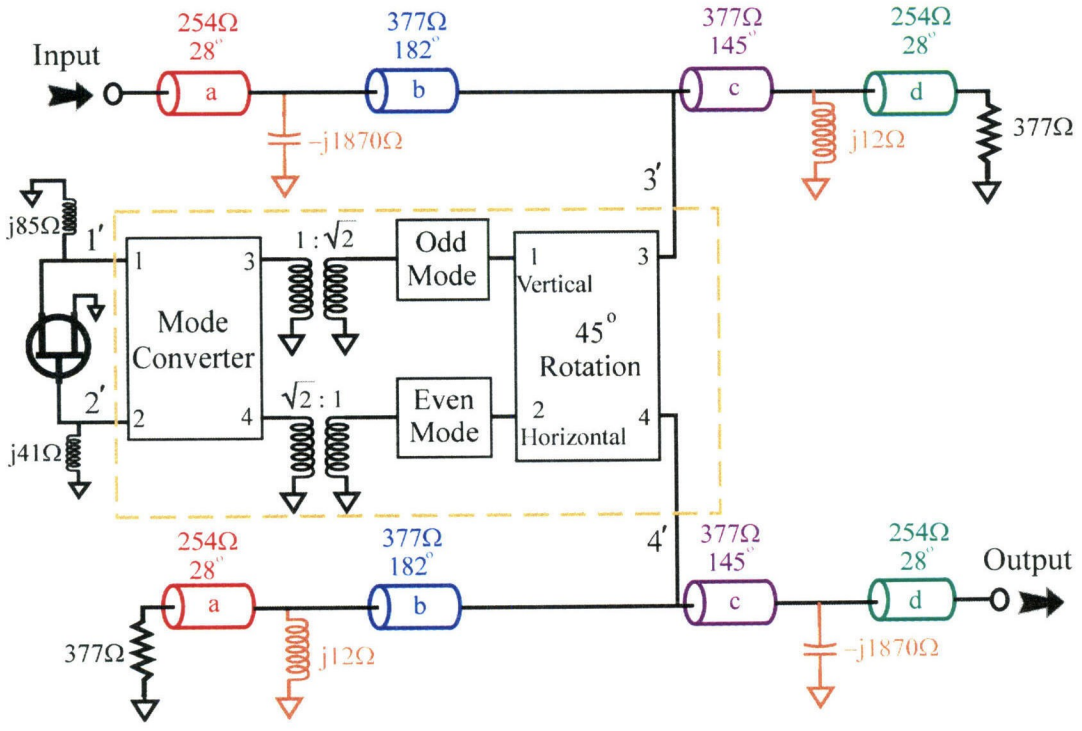

(b)

Figure 5.15. (a) The proposed grid amplifier assembly. (b) The equivalent circuit model for the grid at 10 GHz.

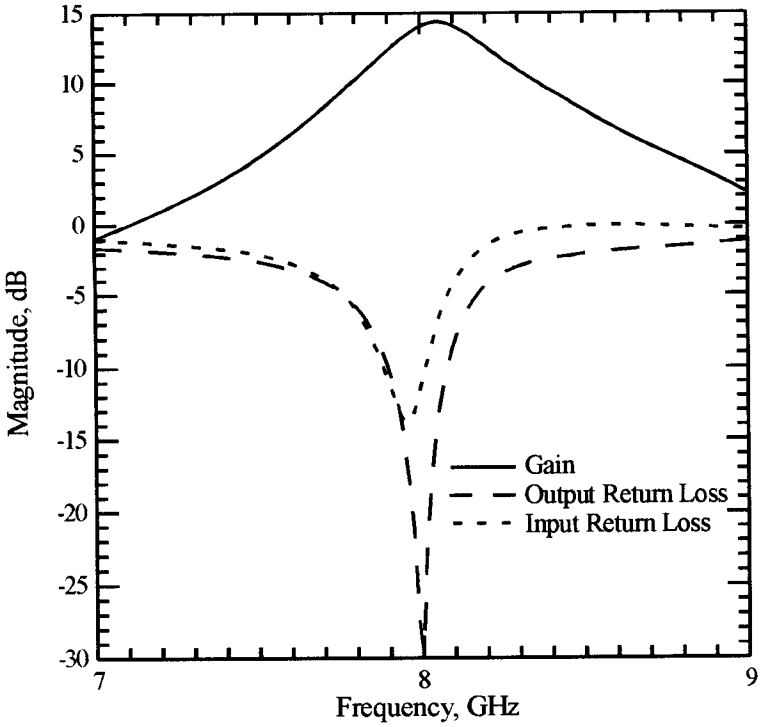

Figure 5.16. Theoretical gain, input return loss, and output return loss of the self-complementary grid amplifier.

the incoming signal were also considered. An input beam with an angle of 45° from the vertical is the optimum. The substrates and the air gap between them are modelled as transmission lines in Fig. 5.15(b). Polarizers are modelled as inductors or capacitors depending on the polarization. To model the transistor, the S-parameters of the FET are normalized to 377 Ω.

Fig. 5.16 shows the theoretical gain of this amplifier for the grid assembly shown in Fig. 5.15(a). The predicted gain is 14 dB at 8 GHz. The input and output return loss are also shown.

The grid is fabricated by etching the patterns on a double sided Duroid substrate with copper cladding. The front and the back patterns are aligned so that the front diamond-shaped source leads are in alignment with the back side drain bias diamonds. Holes connecting the front of the grid to the back side with a diameter of approximately 0.3 mm are made manually using a drill

bit and a pin vise. The holes go through the substrate and stop at the back side copper cladding. The front-to-back drain connection is made by filling the holes with conducting silver epoxy. The substrate is gold plated to facilitate wire bonding. The bottom plates of the capacitors are glued to the copper with conducting silver epoxy and the top plate connections are made using wire bonds. Fig. 5.17(a) shows a picture of the grid inside a holder, and Fig. 5.17(b) is a closeup view of the grid.

5.5. GAIN MEASUREMENT

The grid suffered from random oscillations. The onset of these oscillations were at a drain bias voltage of 1.85 V and a bias current of 850 mA. The oscillation frequency and power were a function of both bias voltage and time. At times the oscillation spectrum of the grid had a few distinct peaks and at other times an oscillation with numerous peaks was visible, and occasionally the grid stopped oscillating. When the grid oscillated, the frequencies of oscillation were at a range from 3–15 GHz. Since the grid oscillation varied with time pattern measurements were impossible. Intuitive techniques used to suppress these oscillations were unsuccessful. These oscillations were insensitive to the polarizer position and to the grid amplifier substrate thickness. Placing resistors between the gate and the drain leads in each unit cell had no effect on the oscillation. These resistors are visible in Figs. 5.17(a) and 5.17(b). They are glued to the substrate adjacent to the transistor in each unit cell. Bond wires connect each resistor to the gate and the drain leads.

The gain of this grid was measured at a bias point where there were no oscillations. The gain measurement method is similar to the measurement explained in Section 3.3.2. In order to use the setup in Fig. 3.11 the grid and the two polarizers shown in Fig. 5.15(a) are rotated by 45°.

The measured gain is shown in Fig. 5.18. This gain is measured for a drain voltage of 1.85 V and a total drain current of 850 mA, the operating point before

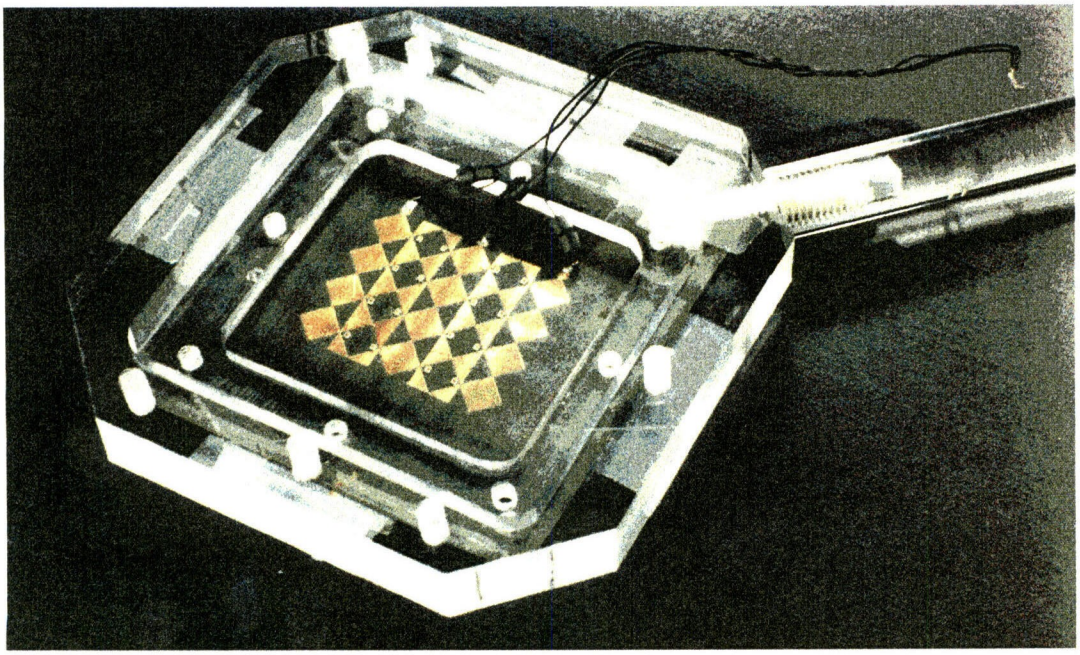

(a)

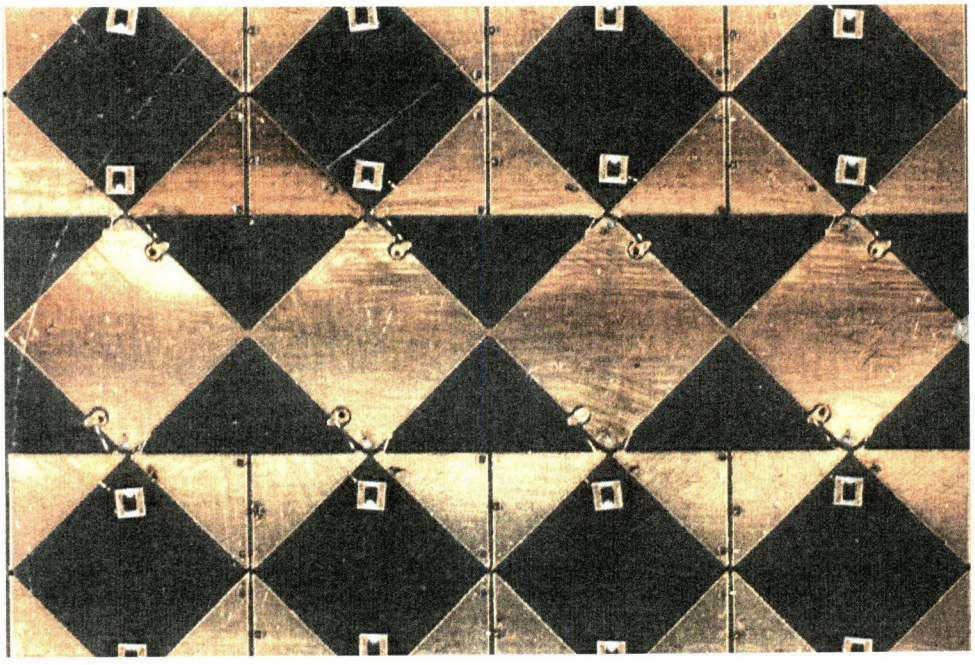

(b)

Figure 5.17. (a) Grid amplifier inside a holder. (b) Closeup view of the front of the grid amplifier.

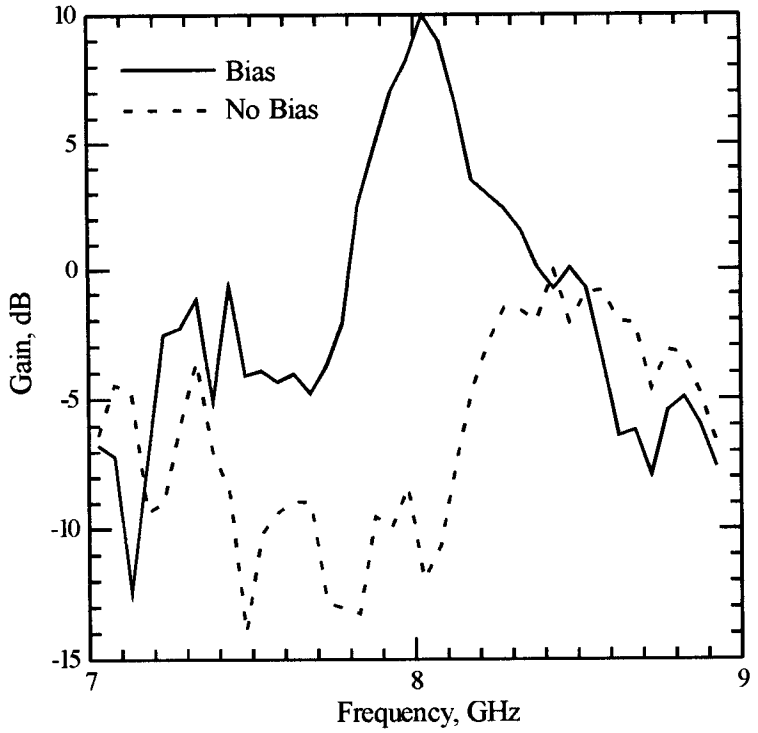

Figure 5.18. Measured gain of the amplifier versus frequency.

the onset of oscillations. The output polarizer in this measurement is 1–2 mm away from the grid. The input polarizer is at a distance of 2.8 cm from the grid. Tuning slabs with a relative dielectric constant of 2.2 are also used at the input and output. The input tuning slab is 1 cm away from the input polarizer and the output tuning slab is 1.8 cm away from the output polarizer. The output polarizer is placed very close to the grid amplifier. Therefore, the assumptions inherent in the simple transmission-line model shown in Fig. 5.15(b), which only considers the propagating TEM mode, are not satisfied [6]. This makes comparison between theory and experiment difficult. The measured peak gain is 10 dB at 8 GHz. The gain of the amplifier when it is not biased is also shown in Fig. 5.18. At peak gain the difference between the biased and unbiased gain is over 20 dB. To insure that the grid is stable at this bias, the output power was measured versus the input power. A linear dependance between the input and the output power indicates that the grid is stable.

The 3-dB bandwidth of this amplifier is 210 MHz. This narrow bandwidth is possibly due to the inductors used at the gate and the drain of the transistor in each unit cell. These inductors are used to resonate with the input and output capacitances of the FET and provide the appropriate input and output impedances for the device.

5.6. FUTURE WORK

The unit cell used for simulating this grid, Fig. 5.8(b), is the simplified version of the cell used in the construction of the amplifier, Fig. 5.14(a). Therefore, none of the details in the unit cell are considered in the simulation. In the future the entire unit cell has to be used in HFSS simulations. Also, using inductors at the gate and drain of the device for matching purposes limits the operating bandwidth of the grid. It is desirable to use devices that are internally matched to the appropriate impedance of the grid. According to Deschamps's paper [2], if one port of a self-complementary structure is terminated to $\eta_o/2$, an impedance of $\eta_o/2$ will be seen from the other port. Therefore, use of devices that are inherently matched to $\eta_o/2$ are ideal for self-complementary structures.

References

[1] H.G. Booker, "Slot Aerials and Their Relation to Complementary Wire Aerials (Babinet's Principal)," *J. IEE*, pt. III-A, pp. 620–627, May 1946.

[2] G.A. Deschamps, "Impedance Properties of Complementary Multiterminal Planar Structures," *IRE Trans. on Antennas and Propagation, AP-7,* pp. 371–378,, December 1959.

[3] M.P. De Lisio, S.W. Duncan, D.-W. Tu, C.-M. Liu, A. Moussessian, J.J. Rosenberg, D.B. Rutledge, "Modelling and Performance of a 100-Element pHEMT Grid Amplifier," *IEEE Trans. Microwave Theory Tech.*, vol. 44, pp. 2136–2144, December 1996.

[4] M. Kim, E.A. Sovero, J.B. Hacker, M.P. De Lisio, J.-C. Chiao, S.-J. Li, D.R. Gagnon, J.J. Rosenberg, D.B. Rutledge, "A 100-Element HBT Grid Amplifier," *IEEE Trans. Microwave Theory Tech.*, vol. 41, pp. 1762–1771, Oct. 1993.

[5] R.M. Weikle, "Quasi-Optical Planar Grids for Microwave and Millimeter-Wave Power Combining," Ph.D. Thesis, California Institute of Technology. Pasadena, CA, 1992.

[6] J.-C. Chiao, J. Bae, K. Mizuno, D.B. Rutledge, "Metal Mesh Couplers Using Evanescent Waves at Millimeter and Submillimeter Wavelengths," *The 19th International Conference on Infrared and Millimeter-Wave,* Sendai, Japan, 1994.

Chapter 6

Terahertz Grid Frequency Doublers

This chapter presents 144-element terahertz quasi-optical frequency doublers. These grids are planar structures with bow-tie-antenna unit cells, each loaded with a planar Schottky diode. These grids are fabricated at the Semiconductor Devices Laboratory at the University of Virginia (UVA), and the measurements are done at the Center for Free-Electron Laser Studies at the University of California, Santa Barbara (UCSB). The maximum output power measured for these grids is 24 mW at 1 THz for 3.1-μs, 500-GHz input pulses with a peak input power of 47 W. To date this is the largest reported output power for a multiplier at terahertz frequencies. Measurements show that this grid can also generate second harmonics at 1.29 THz for an input of 645 GHz, although no power measurements are done for this frequency.

6.1. INTRODUCTION

There is increasing demand for submillimeter-wave sources for use in radio astronomy and remote sensing [1,2]. Conventional sources such as lasers and vacuum-tubes are large and heavy. They need high voltage power supplies and have limited tuning range. Therefore it is desirable to use solid-state diode multipliers to generate higher harmonics from low-frequency tunable signal sources such as Gunn-diode oscillators. Currently most of these diode multipliers are a single device, a pair of devices, or a cascade of several multipliers mounted in a waveguide with a whisker contact. Fig. 6.1 shows the output

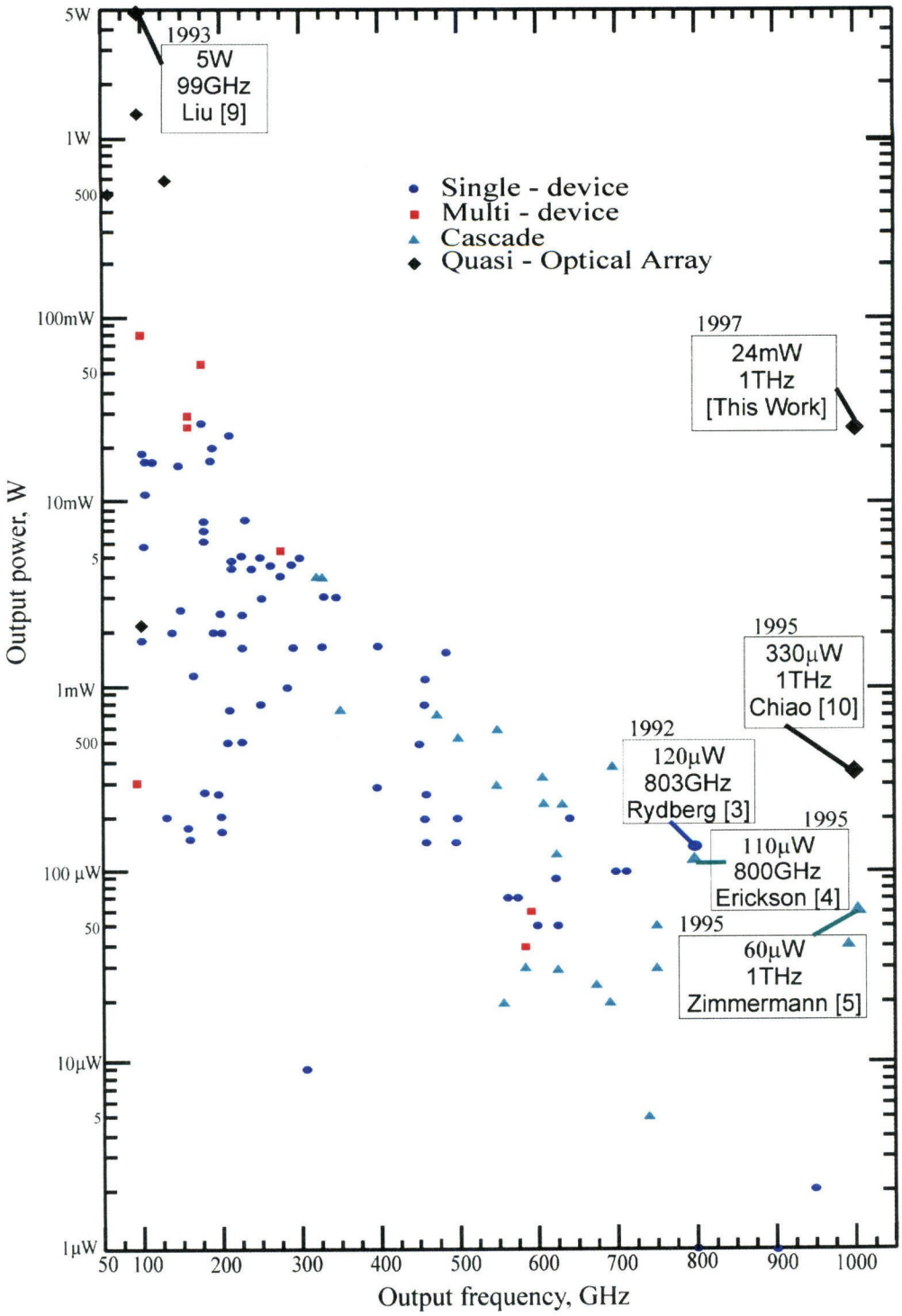

Fig. 6.1. Output power versus frequency for multipliers with output frequencies from 50 GHz to 1 THz. This data is collected and updated by Dr. Jung-Chih Chiao. The reference for some of the data points is given in the figure.

power versus frequency for multipliers with frequencies from 50 GHz to 1 THz. Rydberg *et al.* have demonstrated a Schottky varactor-diode frequency tripler with an output power more than 120 μW at 803 GHz [3]. Erickson and Tuovinen have presented a waveguide tripler with an output power of 110 μW at 800 GHz [4]. Zimmermann *et al.* have demonstrated a cascade of two whisker-contacted Schottky-varactor frequency triplers with an output power of 60 μW at 1 THz [5].

At higher frequencies the losses associated with waveguide structures are high, and machining of single-mode waveguides is complicated. Quasi-optics allows the output powers of many solid-state devices to be combined in free space without transmission-line losses. A number of millimeter-wave quasi-optical multiplier grids have been demonstrated [6–11]. In 1986 Lam *et al.* presented the first diode grid frequency multiplier [6]. A 5-W frequency tripler at 99 GHz was demonstrated by Liu *et al.* [9]. The first terahertz quasi-optical frequency doubler grid was reported by Chiao *et al.* [10]. This was a 6×6 diode-grid doubler with a peak output power of 330 μW at 1 THz .

A diode-grid frequency multiplier is an array of closely spaced planar Schottky diodes. Fig. 6.2 shows the concept. The fundamental beam excites RF currents on the leads of the bow-ties. The diodes act as a nonlinear surface and generate harmonics. The low-pass filter in the input insures that only the fundamental frequency of the laser will illuminate the grid. The high-pass output filter allows the higher harmonics generated by the grid to pass through, but blocks the fundamental. The input and output tuning slabs are for impedance matching of the input and the output.

Diode grids, similar to the 12×12 grids described in this chapter, were originally designed as sideband generators by Jon Hacker at Caltech [12]. These 6×6 grids shown in Fig. 6.3 were tested by Jung-Chih Chiao as multipliers [10]. Since the original design was for sideband generators, certain design features were not appropriate for multiplier use. For example the flipping of the diode polarity

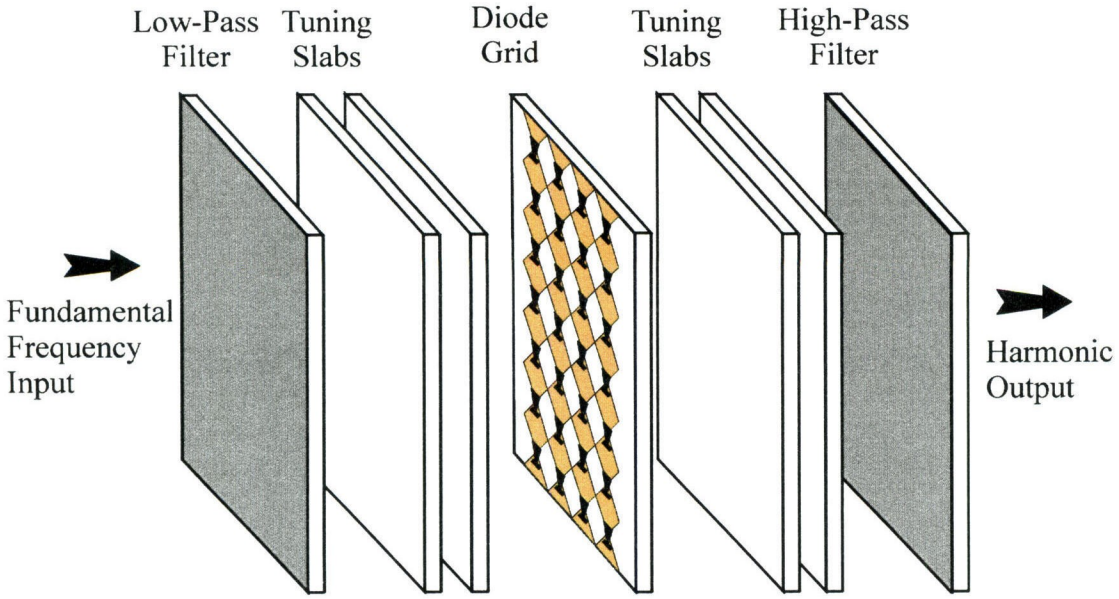

Fig. 6.2. A grid frequency multiplier. The fundamental frequency enters the grid through a low-pass filter. The grid acts as a nonlinear surface and generates harmonics which pass through a high-pass filter.

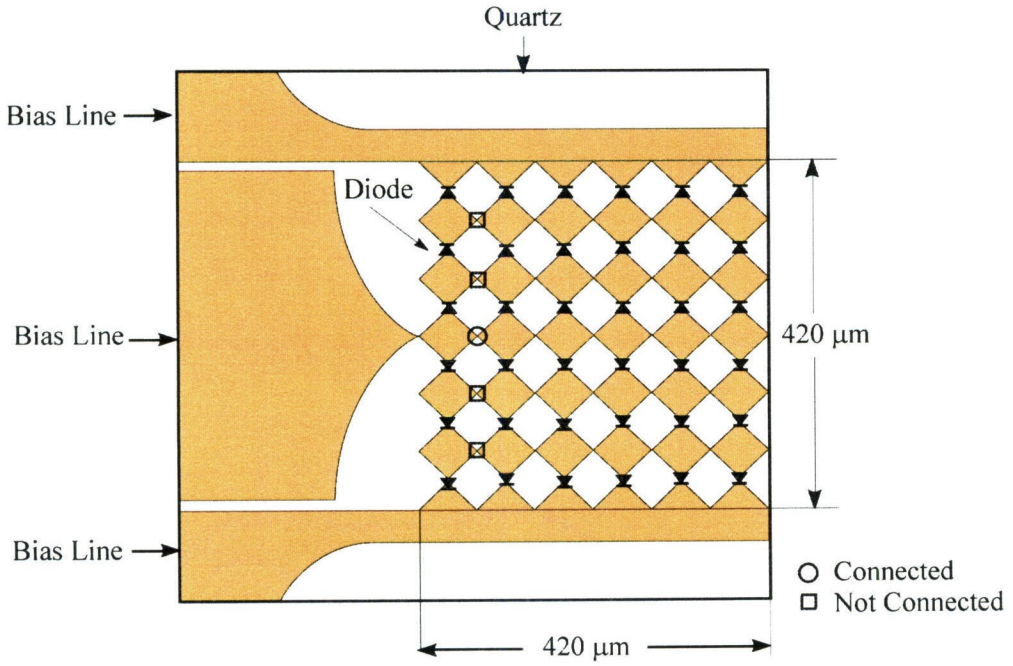

Fig. 6.3. The 6×6 grid frequency doubler presented by Chiao *et al.* The bow-ties are not connected except at the center row. The diodes in the top and bottom halves of the grid have opposite orientation [10].

about the center row of the grid for IF input is not desirable for multiplier use, as the cancellation of fields from the two halves of the grid in the far-field creates a null in the pattern of these multipliers. In the grids presented in this chapter the diode orientation is corrected and the size increased to 12×12 [11].

6.2. DESIGN AND CONSTRUCTION

Yongjun Li in the Semiconductor Devices Laboratory at the University of Virginia fabricated the grid multipliers using monolithic technology [13]. To make diodes for terahertz frequencies, series resistance and zero-bias shunt junction capacitance of the diodes should be greatly reduced by reducing anode diameter and choosing optimum active layer doping and thickness. Fig. 6.4 shows the top view and the cross section of a planar Schottky diode used in the multiplier grids. The anode has a diameter of $0.5\,\mu$m. A surface channel is etched under the anode contact finger to reduce the shunt capacitance. The diodes have an estimated junction capacitance of 0.6 fF at zero bias, and a DC series resistance of $14\,\Omega$.

The grid consists of an array of 12×12 bow-tie antennas on a 30-μm-thick fused-quartz substrate with a relative dielectric constant of 3.78. Each unit cell is $70\,\mu$m on a side. The Schottky-diode junction is located at the center of the cell. The total length of the contact finger is $14\,\mu$m and the widths of the anode and cathode fingers are $1\,\mu$m and $2\,\mu$m. The diode grid is first fabricated on a GaAs substrate. After fabrication the GaAs substrate is etched away and the diode structure is glued on the quartz substrate. Fig. 6.5 shows the grid and the unit cell. The diodes are in series from top to bottom. Two kinds of grids were fabricated. One where all cells in a row are connected, shown with circles in Fig. 6.5(a), and the other with no electrical contacts between cells in a row. The grid can be biased through the bias lines at the top and bottom of the grid. Fig. 6.6(a) shows a picture of a portion of a grid where the unit cells in each

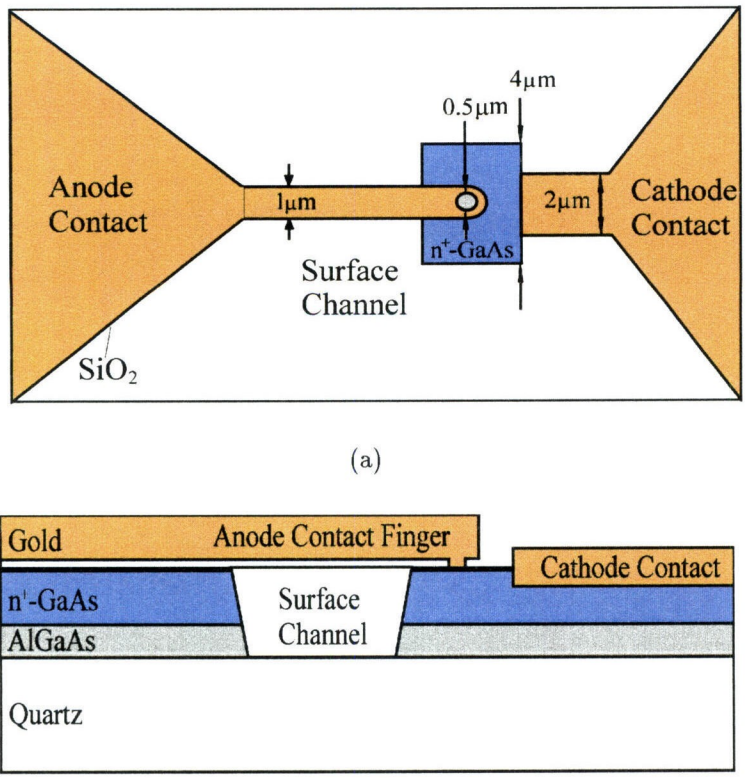

Figure 6.4. Schottky-diode layout. (a) The top view. (b) The cross section. The n-GaAs layer is 0.1 μm thick and has a doping concentration of $4 \times 10^{17}\text{cm}^{-3}$. The n^+-GaAs layer has a thickness of 3 μm and a doping of $5 \times 10^{18}\text{cm}^{-3}$. The AlGaAs layer has a thickness of 1.5 μm.

row have electric contacts and Fig. 6.6(b) is a picture of a grid with no electric contacts in a row. A picture of the unit cell is shown in Fig. 6.7(a) and Fig. 6.7(b) shows the entire grid.

The design of these grids are described in detail in Jon Hacker's and Jung-Chih Chiao's theses [12,14]. The embedding impedance of the grid unit cell is calculated using the EMF method and numerical three-dimensional finite-element HFSS simulation for the unit-cell metal pattern placed inside a waveguide. This equivalent unit-cell model combined with the device equivalent circuit is presented as a transmission-line model and used in the design of the grids [12,14].

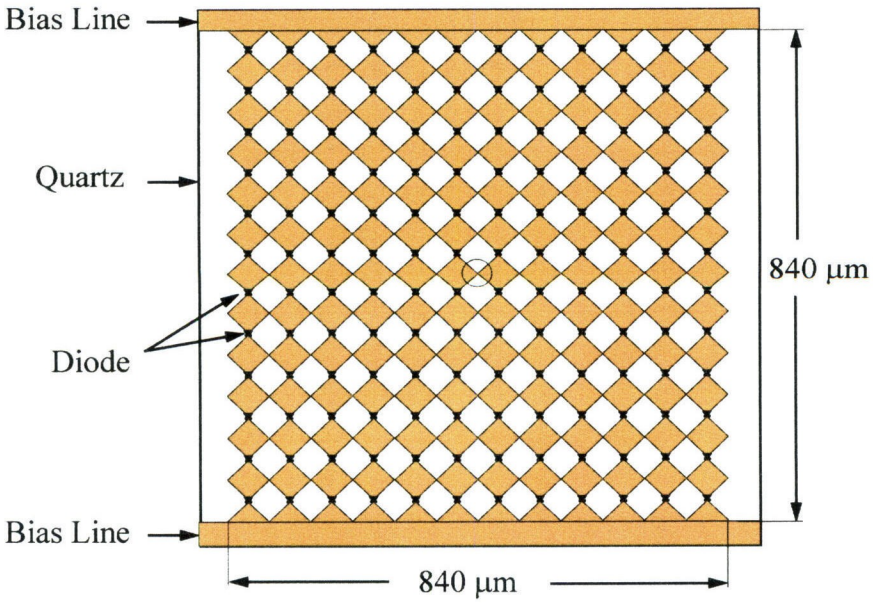

(a)

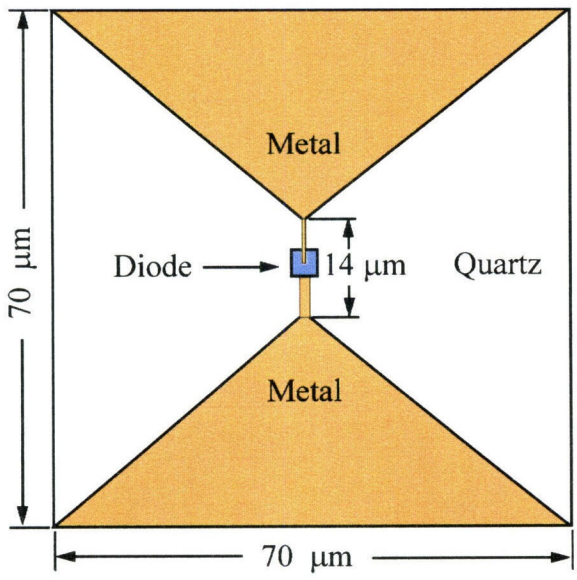

(b)

Figure 6.5. The multiplier grid. (a) The entire 12 × 12 array. (b) The unit cell. The diode is located at the center of the cell.

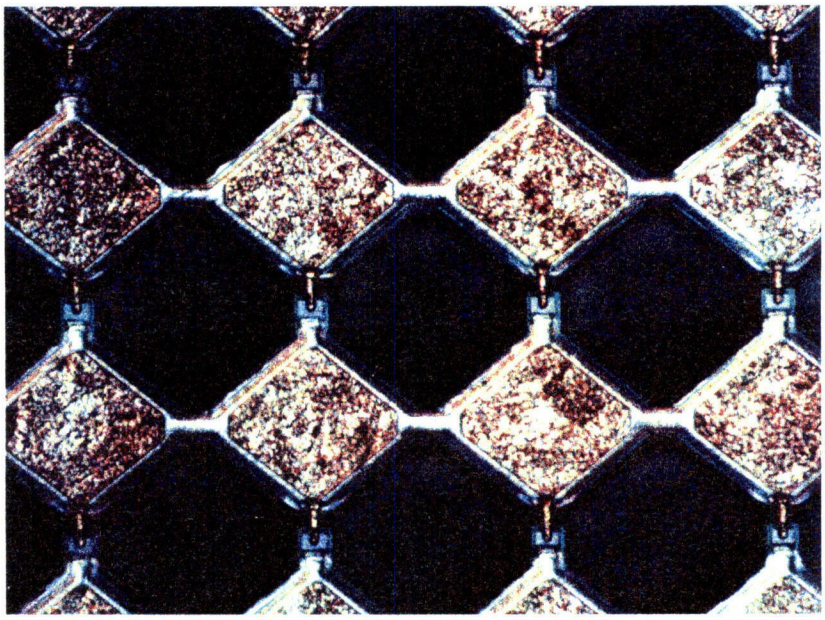

(a)

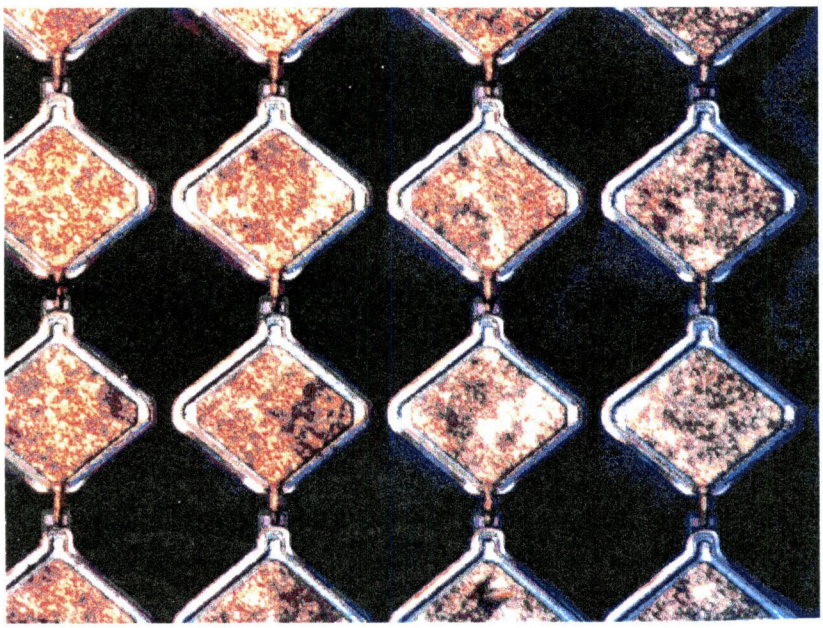

(b)

Figure 6.6. A closeup view of the doubler grid. (a) Grid doubler with electrical contacts in a row. (b) Grid doubler without cell-to-cell connections.

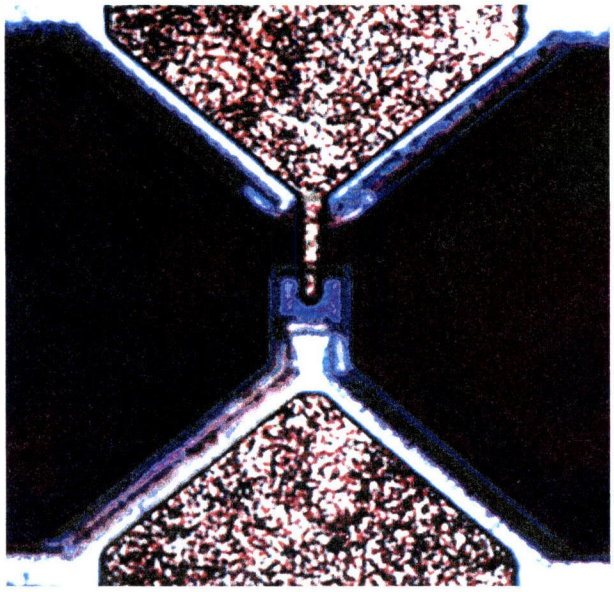

(a)

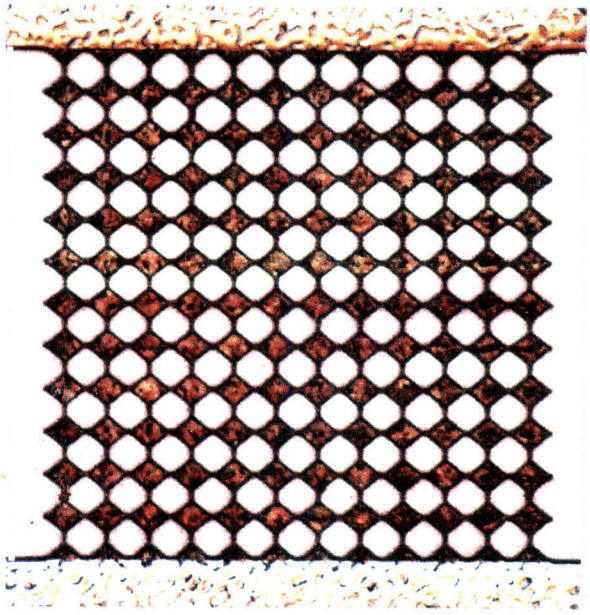

(b)

Figure 6.7. (a) The unit cell of the doubler grid. The diode is located at the center of the cell. (b) The entire 12×12 array.

6.3. MEASUREMENTS

The measurement setup is shown in Fig. 6.8. The input source for these measurements is the free-electron laser (FEL) at the University of California, Santa Barbara [15]. The free-electron laser is capable of generating kilowatts of pulsed power tunable from 120 GHz to 4.8 THz. All the mirrors in the setup are f/1.2 parabolic, with focal length of 13 cm and diameter of 10 cm. Arrows indicate the direction of the beam. The pulse width in the measurements is 3.1 μs. The input power passes through a low-pass multi-mesh filter with a cutoff frequency of 660 GHz and is varied by rotating a polarizer. The second non-rotating polarizer placed after the first one is to maintain the polarization of the beam. A beam splitter directs part of the input power into a pyroelectric reference detector. The rest of the input is focused onto the grid. A metallic-mesh Fabry-Perot interferometer is used to measure the frequency content of the output. The output beam is focused onto a liquid-helium-cooled InSb bolometer through a high-pass filter with a cutoff frequency of 870 GHz. All the components in this setup are aligned using a He-Ne laser. The measurements were done with the assistance of Mike Wanke and Frank Hegmann at UCSB.

The diode grid is suspended in air by gluing it over a hole in a 200-μm-thick microscope cover slip. The hole is cut at the edge of the cover slip as shown in Fig. 6.9 and the grid is glued on top of this hole by placing epoxy at the edges of the grid. To provide the ability to bias the grid, copper strips are etched from copper tape and glued on the microscope cover slip as shown in the figure. Conducting silver epoxy connects the grid bias lines to the copper tape. However, all the measurements were done with the grids unbiased. To add to the robustness of the holder the microscope cover slip is glued on a microscope slide.

The grid is placed in the setup shown in Fig. 6.8 and excited by a 500-GHz input beam. There are no water absorption lines in 500 GHz and 1 THz

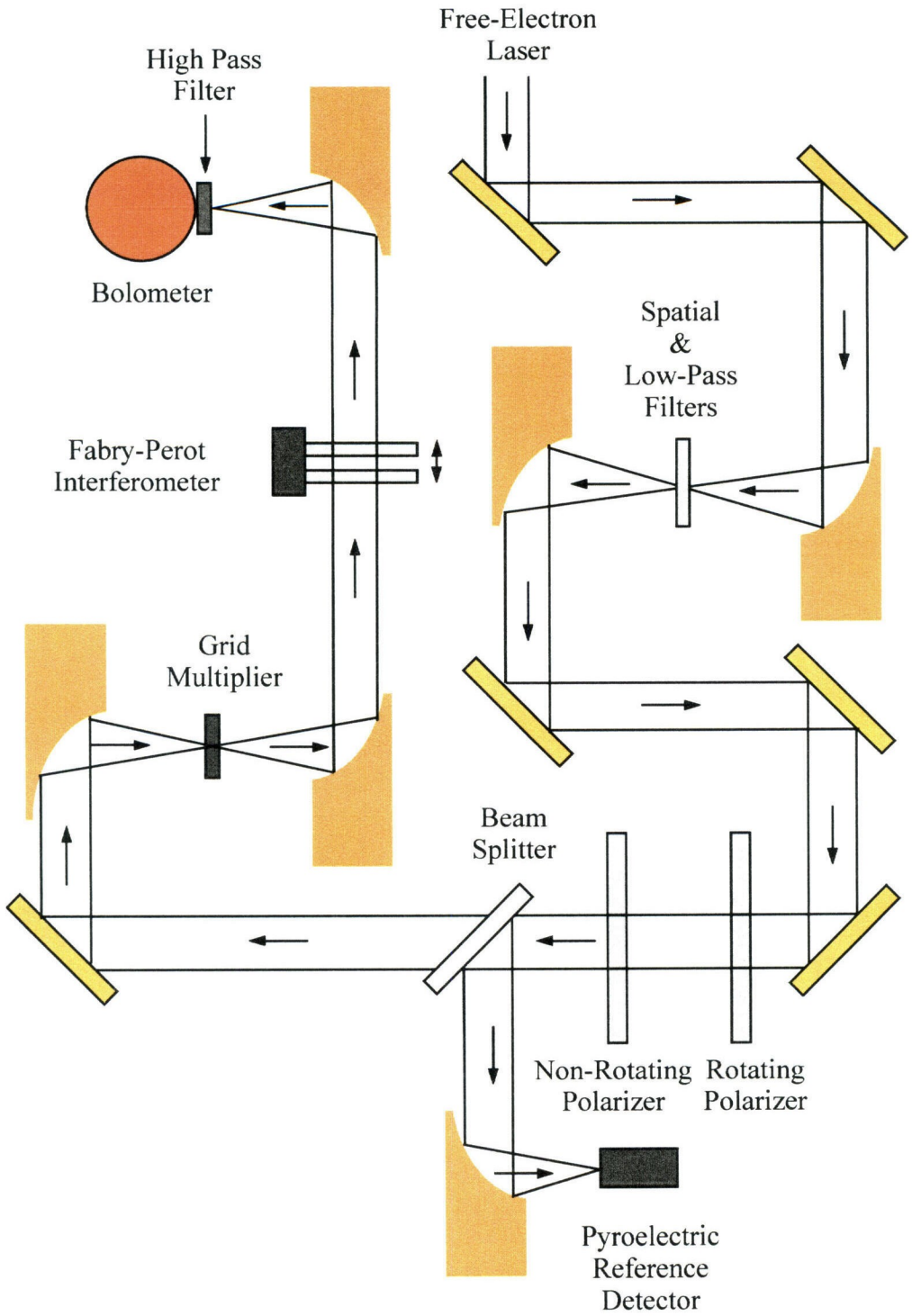

Figure 6.8. Measurement setup.

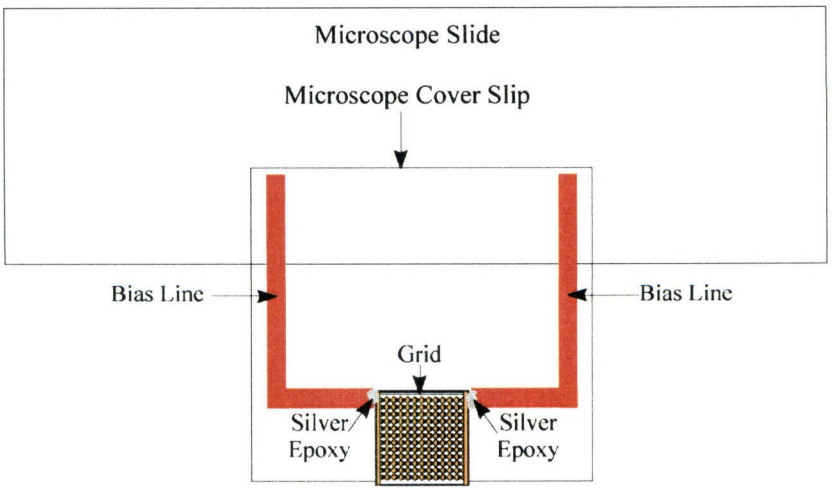

Figure 6.9. Mounting structure of the grid. There is a square hole at the edge of the microscope cover slip and the grid is glued on top of the hole. The hole is slightly smaller than the grid and holds the grid from its three edges.

[16], therefore measurements can be done in free space without the aid of a dry-box. The reference and the output signals are synchronized with the FEL trigger signal that has a frequency of 0.75 Hz. To measure the peak input and output power each pulse is integrated over a time interval in which the signal is flat and divided by the integration time. Fig. 6.10 shows the 3.1 μs output pulse. The pulse width is measured between the points where the voltage of the pulse is half of its maximum voltage. The input pulse, not shown here, also has a pulse width of 3.1 μs as defined in Fig. 6.10. The output and input pulse shapes measured by the bolometer and the pyroelectric detector are almost identical since both detectors are faster than the rise and fall time of the actual pulse. To account for the noise in our measurements the pulses are also integrated for a time period before the arrival of the FEL trigger signal. This offset is subtracted from the measured peak power. This method is used for all the measurements.

The measurements are conducted for two grids. The first grid has electrical contacts connecting all the unit cells in one row as shown in Fig. 6.6(a) and the second grid shown in Fig. 6.6(b) has no contacts in a row. These grids will be referred to as grid #1 and grid #2 respectively.

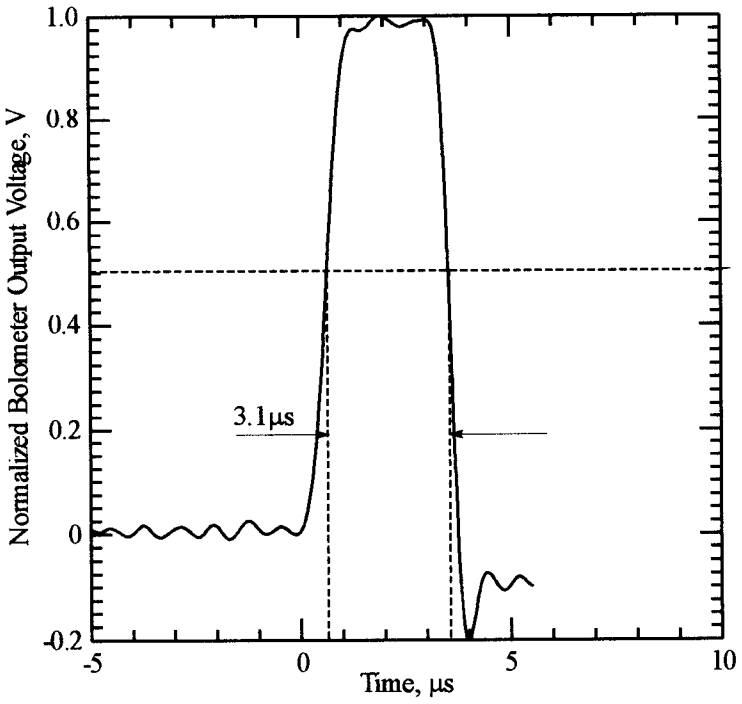

Figure 6.10. Normalized output voltage of the bolometer versus time.

6.3.1. FREQUENCY MEASUREMENT

To investigate whether the grids generate terahertz second harmonics they are placed in the setup shown in Fig. 6.8 and excited with a 500 GHz input signal. A Fabry-Perot interferometer as shown in Fig. 6.8 is used to verify the output frequency of the grids. The metal-mesh plates of the interferometer can be moved in increments of 0.7 μm. Fig. 6.11 shows the output as the Fabry-Perot interferometer is scanned. A sinusoidal wave with a period of 145 μm, is fitted to the measured curve. This period indicates a second-harmonic of 1.03 THz from the grid, for an input frequency of 500 GHz. No other harmonics were detected.

In order to make sure that the output radiation is actually from the grid, we removed the grid. The output pulse disappeared. Also, rotating the grid by 90° had the same effect. This shows that the output signal is not a harmonic of the laser or generated by the GaAs epitaxial layer.

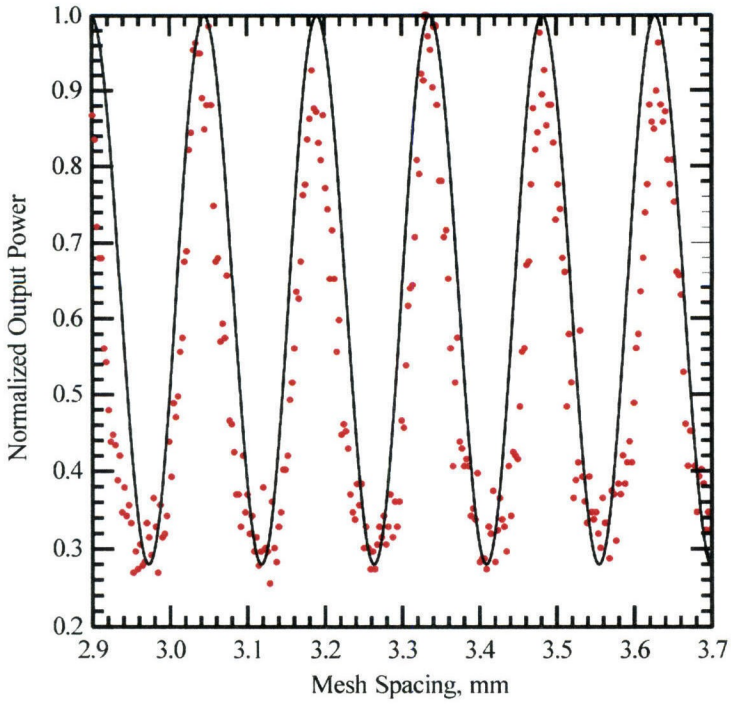

Figure 6.11. Normalized output power as a function of the metal-mesh spacing of the Fabry-Perot interferometer.

6.3.2. INPUT AND OUTPUT POWER MEASUREMENT

To determine the amount of the input power incident on the grid a pyroelectric detector mounted on a two-dimensional positioner was used to measure the spot size of the incident beam at the focal point, where the grid is placed. The measured E and H-plane patterns of the incident beam are shown in Figs. 6.12(a) and 6.12(b) respectively. Comparing the spot size of the incident beam to the grid size which is 840 μm on the side indicates that almost all of the input power is incident on the grid.

Figs. 6.13(a) and 6.13(b) show the power dependence of grids #1 and #2 with normal incidence. A pyroelectric detector measures the input power and a InSb bolometer is used for measuring the output (Fig. 6.8). The input and output power are measured using the technique described in Section 6.3. Both the pyroelectric detector and the InSb bolometer are calibrated versus a Thomas Keating

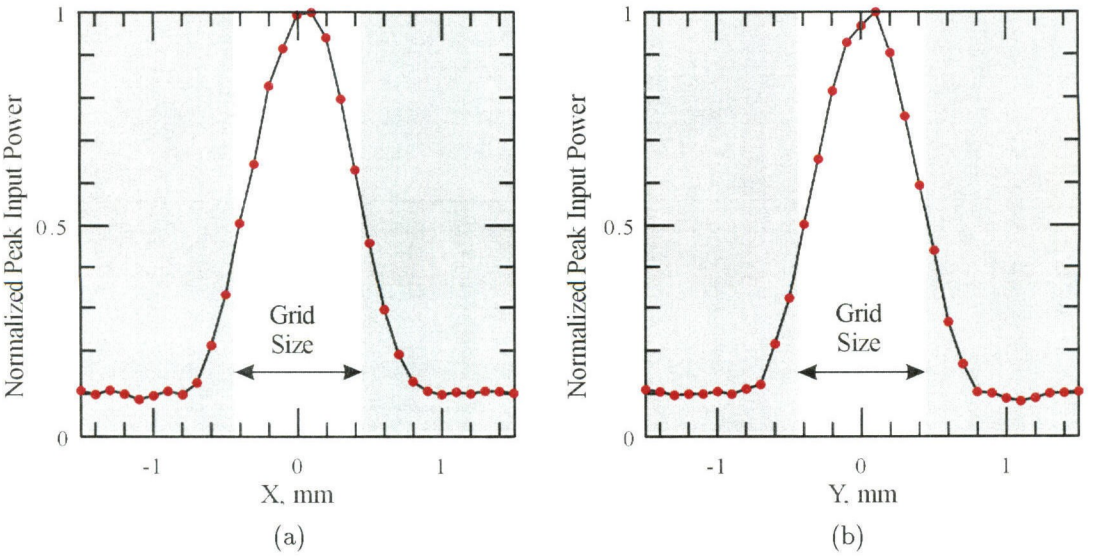

Figure 6.12. Input spot-size measurement at the focal plane using a pyroelectric detector. (a) E-plane pattern. (b) H-plane pattern.

photoacoustic detector. For calibrating the bolometer the FEL is tuned to the second harmonic (1 THz) and the responsiveness of the bolometer is measured versus the photoacoustic detector. Fig. 6.13(a) shows the power dependance of grid #1. A peak output power of 5.5 mW at 1 THz is measured for a peak input power of 36 W at 500 GHz with a pulse width of 3.1 μs. Grid #2 has a peak output power of 2 mW at 1 THz for an input power of 30 W at 500 GHz with the same pulse width. The power dependance of this grid is shown in Fig. 6.13(b). As can be seen in this figure at an input power of approximately 30 W the output starts rolling over. We suspected that some devices in the grid might be damaged. To test this, we remeasured the output power for input powers less than 30 W and compared the new results with the results shown in Fig. 6.13(b). The output was lower than previously measured, indicating damage to the grid. None of the grids were biased or tuned. With low input power, the data follows a square-law relationship for both the measurements. There is a kink in the data for input powers near 1 W . It is possible that the kink is a self-biasing effect, where the RF power changes the diode impedance.

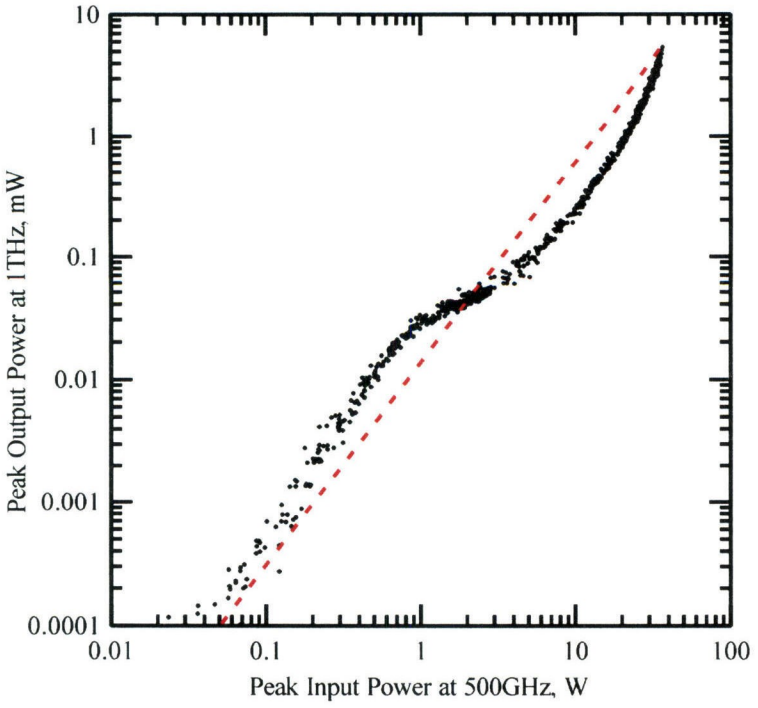

(a)

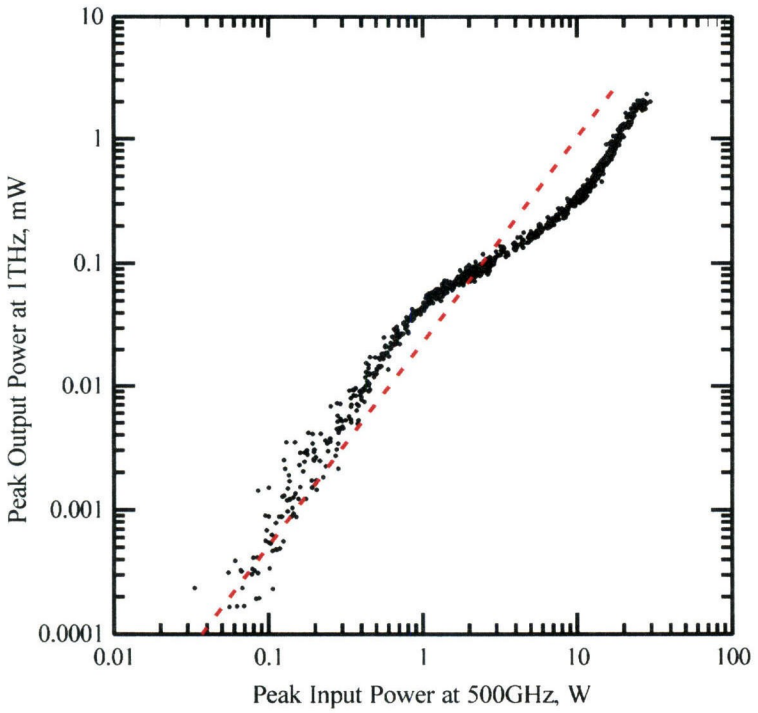

(b)

Figure 6.13. Measured peak output power of the grid versus peak input power. The dashed line shows a square-law relationship. (a) Grid #1. (b) Grid #2.

6.3.3. TUNING MEASUREMENT

The previous measurements were performed with no impedance matching in the input and the output of the grid. Dielectric slab tuners can be used to achieve higher output power and efficiency [17,18]. Instead of double slab tuners as shown in Fig. 6.2 single slabs as shown in Fig. 6.14 are used in the input and the output. The slabs are z-cut crystal-quartz circular discs with a diameter of 1 cm. The input tuner has a thickness of 60 μm and the output tuner is 30-μm thick. Each disc is placed on top of a hole drilled inside a piece of plexiglass and held in place by a drop of glue on one corner of the disc. A motorized micrometer moves each tuner.

To investigate whether the tuners improve the power performance of the grid we first re-measured the output versus the input power of grid #1 with no tuners. The reason for repeating this measurement is because the output

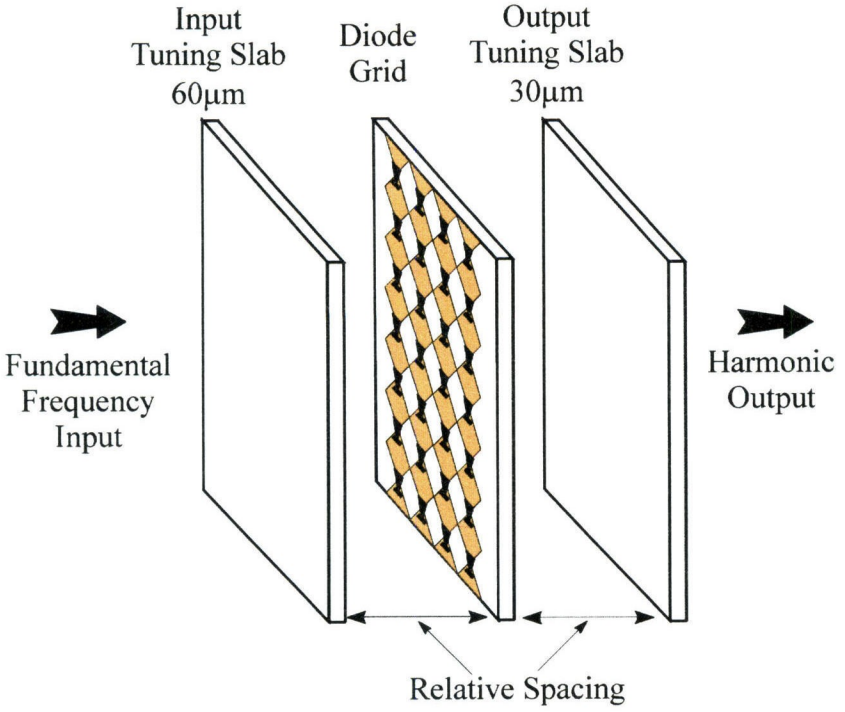

Fig. 6.14. Grid frequency doubler with input and output tuners.

power of the grid is highly dependant on the shape of the input beam and the relative positioning of the grid with respect to the beam which may vary in different measurements. This measurement, shown in Fig. 6.15, indicates a higher efficiency for the grid than the efficiency calculated from Fig. 6.13(a). This is probably due to a better alignment of the grid with the input signal in this measurement.

To measure the input tuning curve shown in Fig. 6.16(a) the output tuner in Fig. 6.14 is removed and the output power is measured versus the input tuner relative distance from the grid. At its closest point to the grid (0 in Fig. 6.16(a)) the tuner is less than 500 μm away from the grid. The average spacing between the peaks in this figure is 300 μm, which is half the wavelength of the fundamental frequency. After the first two periods there is a significant drop in the output

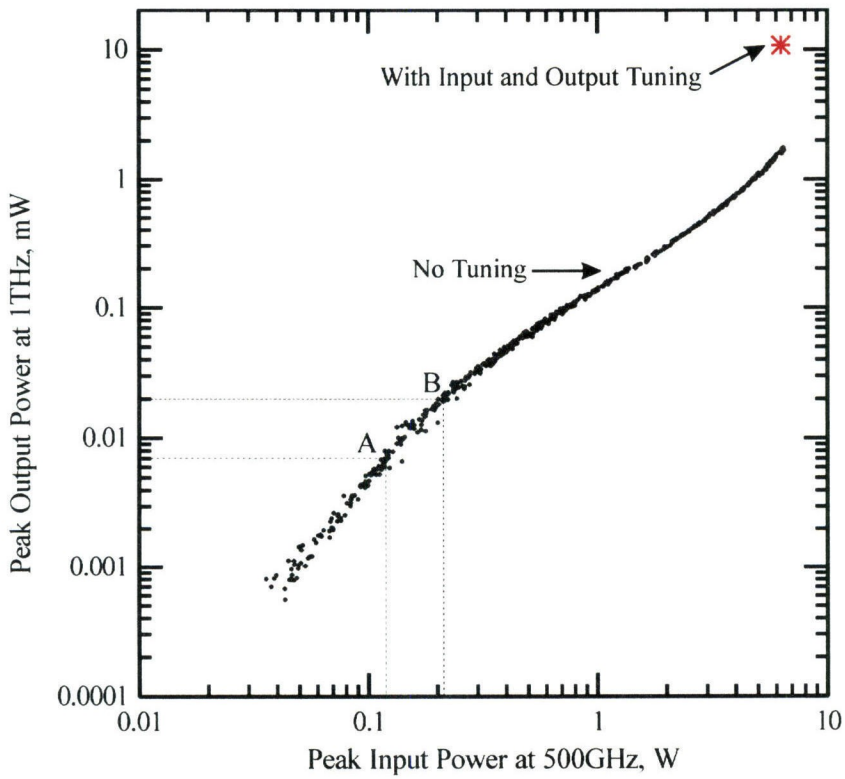

Figure 6.15. Measured peak output power at 1 THz versus the input power at 500 GHz with and without tuners. A and B show the points where the input and output tuning measurements are done.

power which is probably due to diffraction. Point A in Fig. 6.15 shows the input and the output power of the grid for the input tuning measurement before the tuning slab is added. This corresponds to an output power of 7 μW shown with a dashed line in Fig. 6.16(a). By adding the input tuner the 7-μW output power increases to 37 μW (Fig. 6.15).

The output tuning curve is shown in Fig. 6.16(b). For this measurement the input tuning slab shown in Fig. 6.14 is removed and the output is measured versus the relative position of the output tuning slab from the grid. Here also, the closest distance from the grid (0 in Fig. 16(b)) is less than 500 μm. The average spacing between the peaks is 150 μm which is half the second harmonic wavelength. Point B in Fig. 6.15 shows the input and the output powers before adding the output tuning slab. For this measurement the output power of the grid with no tuners is 20 μW shown with a dashed line in Fig. 6.16(b). The output tuner increases the output power from 20 μW to 32.5 μW. It appears that this tuning slab also tunes the input as is evident from the alternating high-low peaks in Fig. 6.16(b).

Next, with both the input and the output tuners in place (Fig. 6.14) we optimized the position of these tuners for maximum output power. For an input power of 6.3 W an output power of 10.8 mW was measured indicating an efficiency of 0.17% (Fig. 6.15).

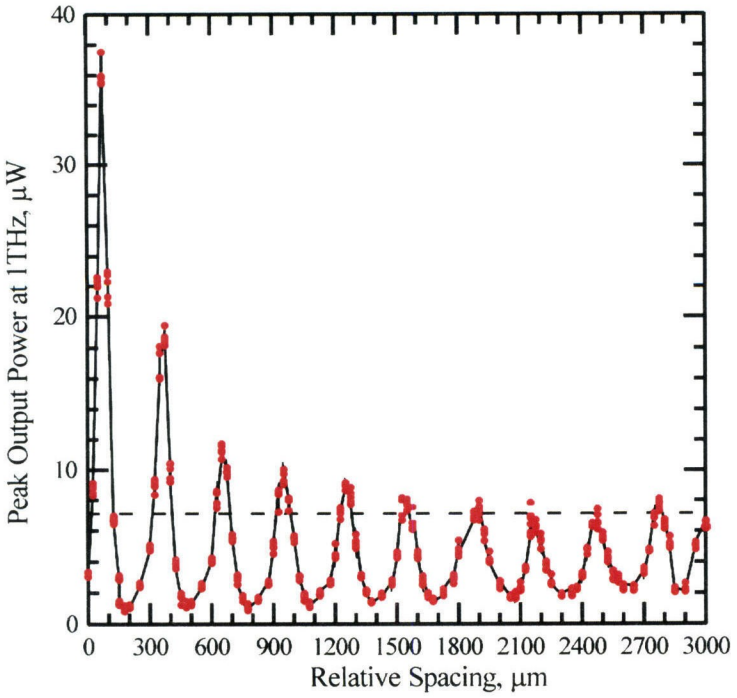

(a)

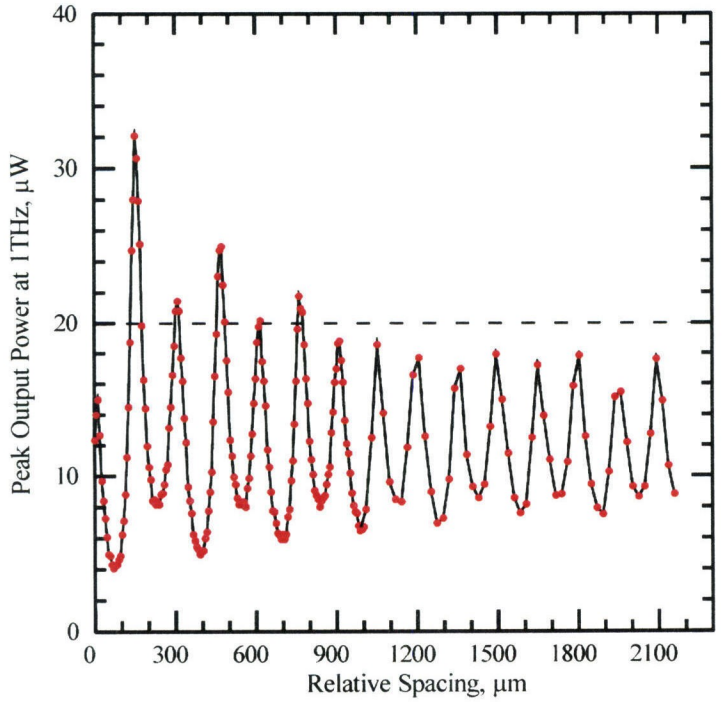

(b)

Figure 6.16. Measured output power versus the relative position of (a) the input tuner, (b) the output tuner. The dashed line is the output power with no tuner for each measurement.

6.3.4. PATTERN MEASUREMENT

Fig. 6.17 shows the effect of rotating the grid about its axis from $-90°$ to $+90°$. Unlike the pattern for the previous doubler grid, reported by Jung-Chih Chiao [10], this pattern has no nulls. In the case of the previous grid the diodes were oriented with opposite polarity about the centerline of the grid, causing a null in the output. Here, the diode orientation is corrected eliminating the null in the pattern. The output power stays within 30% of the maximum for angles up to 30°. A theoretical $\cos^3\theta$ obliquity factor is also plotted in this figure. Because the incident beam to the grid is approximately the same size as the grid, rotating the grid about its axis causes the input power density to reduce by a factor of

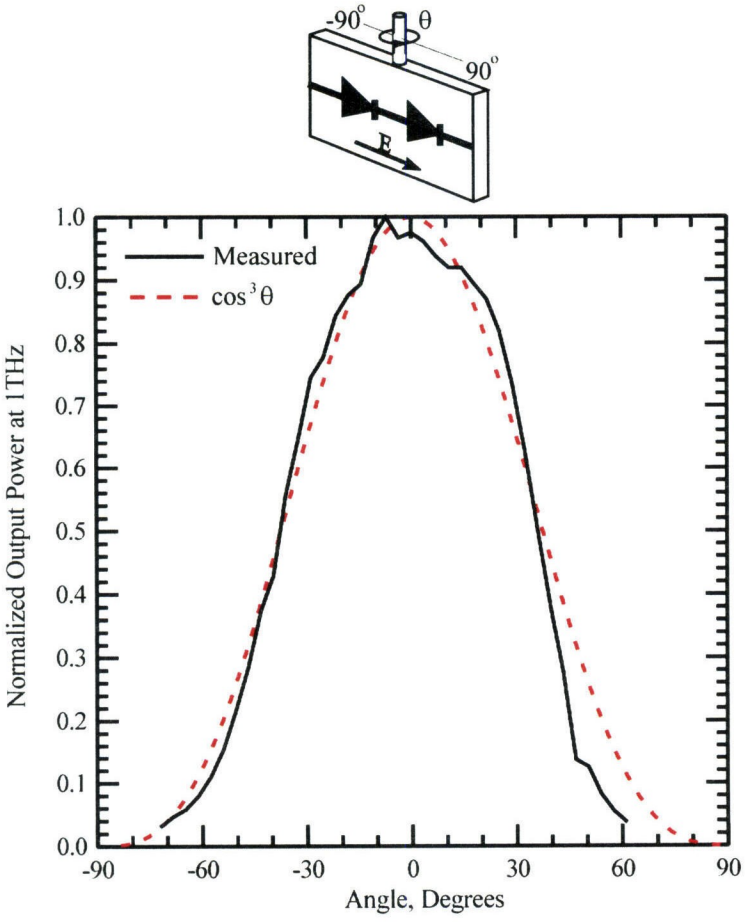

Figure 6.17. Output pattern. The measurement was done by rotating the grid from $-90°$ to 90° with the electric field parallel to the diodes.

$\cos\theta$. The second factor of $\cos\theta$ in this obliquity factor is because the grid is a square law device, and the third factor is because the output beam becomes wider as the grid rotates, missing the output detector.

6.3.5. DOUBLER GRID AT HIGHER FREQUENCIES

This grid (grid #1) is also tested with an input of 645 GHz. A Fabry-Perot measurement similar to the one described in Section 6.3.1 is used to measure the frequency content of the output signal. This measurement indicates an output at 1.29 THz. Fig. 6.18 shows a normalized plot of the peak output power at 1.29 THz versus the peak input power at 645 GHz with a pulse width of 3 μs. Both the input and the output powers are normalized to 1. No absolute power measurements are conducted at this frequency. As in the previous power measurements the input

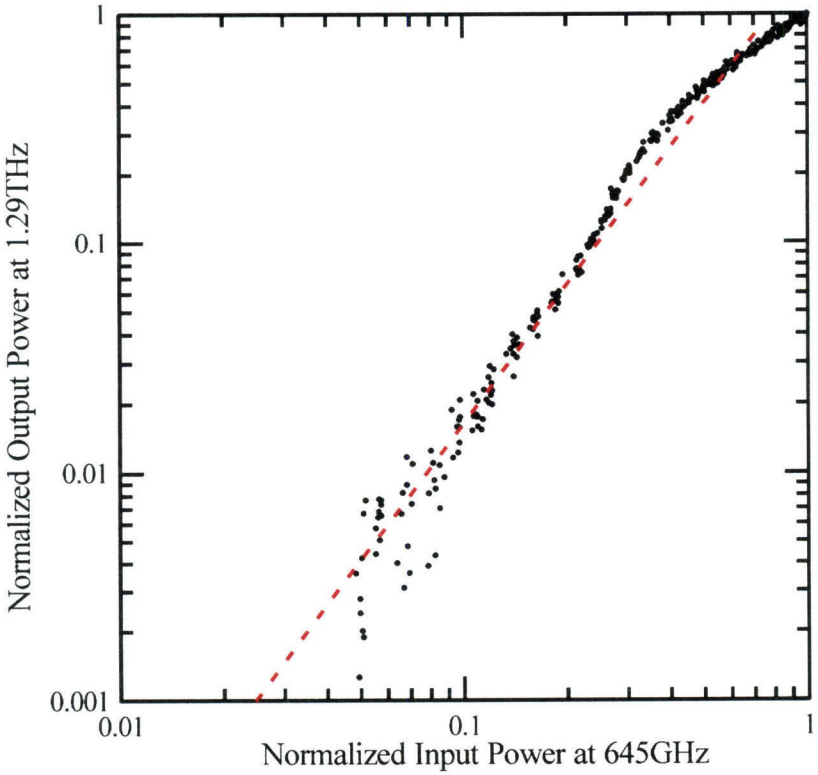

Figure 6.18. Normalized peak output power of the grid versus the normalized peak input power. Both the input and the output are normalized to 1. The dashed line shows a square-law relationship.

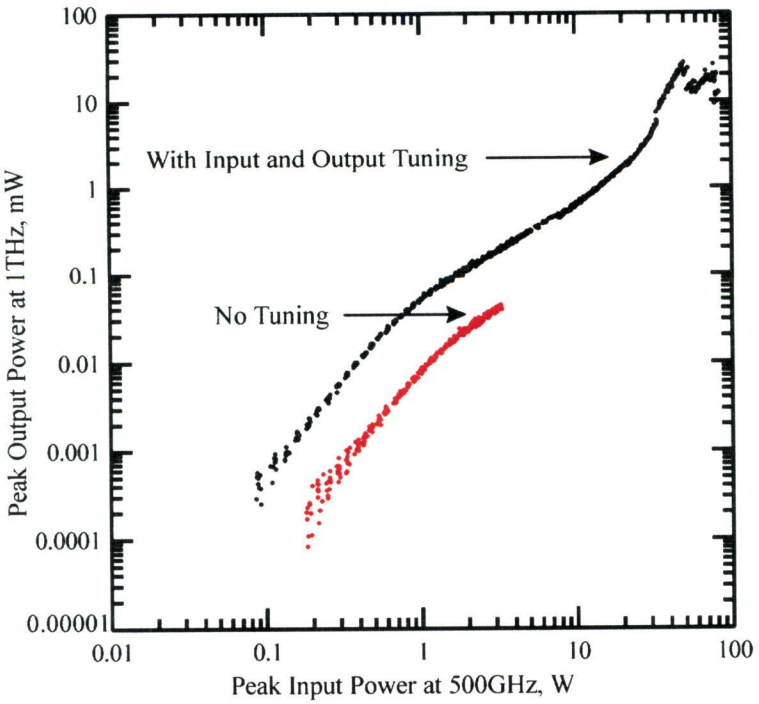

Figure 6.19. Measured peak output power at 1 THz versus input power at 500 GHz with and without tuning.

and the output have a square law relationship only for low inputs. At higher input powers there is a kink in the data. In this measurement the input power is not increased past this kink.

6.3.6. MAXIMUM OUTPUT POWER

To measure the maximum output power of the grid at 1 THz we placed both the input and the output tuners in the setup of Fig. 6.14, optimized their position for maximum output, and increased the input power until the grid was damaged. Grid #1 was used for the measurement. Fig. 6.19 shows the output versus the input power measurement before the input and the output tuners are added, and compares it to the same measurement with the tuners optimized for maximum output. The tuners are at a distance less than 500 μm from the grid. A maximum output power of 24 mW is measured at 1 THz with an input power of 47 W for 3.1-μs input pulses.

At an input power of 47 W the output starts rolling over indicating damage to some devices. As the input power increases further, the output power starts increasing again until some more devices are damaged. Fig. 6.19 shows a second decrease in the output power. We stopped the measurement at this point.

6.4. CONCLUSIONS AND SUGGESTIONS FOR FUTURE WORK

In this chapter a planar grid of 144 Schottky diodes suitable for use as a quasi-optical frequency doubler has been presented. A peak output power of 24 mW is measured at 1 THz for 3.1-μs 500-GHz input pulses with a peak power of 47 W. To date this is the largest power measured for a multiplier grid at terahertz frequencies. Certain improvements might result in a better efficiency and a larger output power for these grids. Rydberg [3] and Erickson [4] have both reported efficiencies near 1% at close to terahertz frequencies for their frequency multipliers. We believe that by improved input and output matching we might achieve higher efficiencies for this grid. As discussed in Section 6.3.3 the output tuner seems to be effecting the input matching of the grid. It might be possible to place a filter between the output tuner and the grid to tune the output independently from the input. Also the effects of biasing the grid needs to be investigated.

References

[1] T.G. Phillips, "Development in Submillimeter Astronomy," *The 19th International Conference on Infrared and Millimeter Waves,* Sendai, Japan, Oct. 1994.

[2] J.W. Waters and P.H. Siegel, "Applications of Millimeter and Submillimeter Technology to Earth's Upper Atmosphere: Results To Date and Potential for the Future," *The 4th International Symposium on Space Terahertz Technology,* Los Angeles, CA, March 1993.

[3] A. Rydberg, B.N. Lyons and S.U. Lidholm, "On the Development of a High Efficiency 750 GHz Frequency Tripler for THz Heterodyne Systems," *IEEE Trans. on Microwave Theory and Tech.,* vol. 40, No. 5, pp. 827-830, May 1992.

[4] N. Erickson and J. Tuovinen, "A Waveguide Tripler for 800-900 GHz," *The 6th International Symposium on Space Terahertz Technology,* Pasadena, CA, March 1995.

[5] R. Zimmermann, T. Rose and T. Crowe, "An All Solid-State 1 THz Radiometer for Space Applications," *The 6th International Symposium on Space Terahertz Technology,* Pasadena, CA, March 1995.

[6] W.W. Lam, C.F. Jou, N.C. Luhmann, Jr. and D.B. Rutledge, "Diode Grids for Electronic Beam Steering and Frequency Multiplication," *Int. Journal of Infrared and Millimeter Waves,* vol. 7, pp. 27–41, 1986.

[7] C.F. Jou, W.W. Lam, H.Z Chen, K.S. Stolt, N.C. Luhmann, Jr. and D.B. Rutledge, "Millimeter Wave Diode Grid Frequency Doubler," *IEEE Trans. on Microwave Theory and Tech.,* vol. 36, No. 11, pp. 1507-1514, Nov. 1988.

[8] R.J. Hwu, N.C. Luhman Jr., L. Sjogren, X.H. Qin, W. Wu, D.B. Rutledge, B. Hancock, J. Maserjian, U. Lieneweg, W. Lam, and C. Jou, "Watt-Level Quasi-Optical Monolithic Frequency Multiplier Development," *the Proceedings of the 1st Int. Symposium on Space Terahertz technology,* pp. 126–149, 1990.

[9] H.-X.L. Liu, L.B. Sjogren, C.W. Domier, N.C. Luhman Jr., D.L. Sivco and A.Y. Cho, "Monolithic Quasi-Optical Frequency Tripler Array with 5-W Output Power at 99 GHz," *IEEE Electron Device Letters,* vol. 14, No. 7, pp. 329–331, July 1993.

[10] J.-C. Chiao, A. Markelz, Y. Li, J. Hacker, T. Crowe, J. Allen, D. Rutledge, "Terahertz Grid Frequency Doublers," *The 6th International Symposium on Space Terahertz Technology,* Pasadena, CA, March 1995.

[11] A. Moussessian, M.C. Wanke, Y. Li, J.-C. Chiao, F.A. Hegmann, S.A. Allen, T.W. Crowe, D.B. Rutledge, "A Terahertz Grid Frequency Doubler," to be presented at *The IEEE MTT-S Int. Microwave Symp.*, June 1997.

[12] J.B. Hacker, "Grid Mixers and Power Grid Oscillators," Ph.D. Thesis, California Institute of Technology. Pasadena, CA, 1993.

[13] T.W. Crowe, R.J. Mattauch, H.P. Röser, W.L. Bishop, W.C.B. Peatman and X. Liu, "GaAs Schottky Diodes for THz Mixing Applications," *Proceedings of the IEEE,* vol. 80, No. 11, pp. 1827-1841, Nov. 1992.

[14] J.-C. Chiao, "Quasi-Optical Components for Millimeter and Submillimeter Waves," Ph.D. Thesis, California Institute of Technology. Pasadena, CA, 1996.

[15] S.J. Allen, K. Craig, B. Galdrikian, J.N. Heyman, J.P. Kaminski, K. Campman, P.F. Hopkins, A.C. Gossard, D.H. Chow, M. Lui and T.K. Liu, "Materials Science in the FAR-IR with Electrostatic Based FELs," presented at *FEL 94,* Stanford, CA, August 1994.

[16] H.M. Pickett, R.L. Poynter, E.A. Cohen, M.L. Delitsky, J.C. Pearson, H.S.P. Müller, "Submillimeter, Millimeter, and Microwave Spectral Line Catalogue," JPL Publication 80–23, Rev.4, NASA, Jet Propulsion Laboratory, Caltech, March 10, 1990.

[17] C.F. Jou, "Millimeter-Wave Monolithic Schottky Diode-Grid Frequency Doublers," Ph.D. Thesis, University of California, Los Angeles, CA, 1987.

[18] H.-X.L. Liu, "Monolithic Schottky Barrier and Quantum Barrier Device Arrays for Millimeter Wave Frequency Multiplication," Ph.D. Thesis, University of California, Los Angeles, CA, 1993.

Chapter 7

Conclusions and Suggestions for Future Work

Since the demonstration of the first quasi-optical grid oscillator in 1988 [1] numerous grids are designed and fabricated. Grid mixers [2], phase shifters [3,4] and grid amplifiers [5,6] are a few examples. Millimeter-wave and submillimeter-wave arrays have been presented [7–12], monolithic technology in building grids has been used [7–9], and quasi-optical arrays with Watt-level output powers have been built [13–15]. The ultimate goal is to build quasi-optical transmitters and receivers by stacking different quasi-optical components as shown in Fig. 7.1. Compact size and low cost of fabricating grids along with their graceful degradation due to use of many devices [6] make them an attractive candidate for building transmitters and receivers.

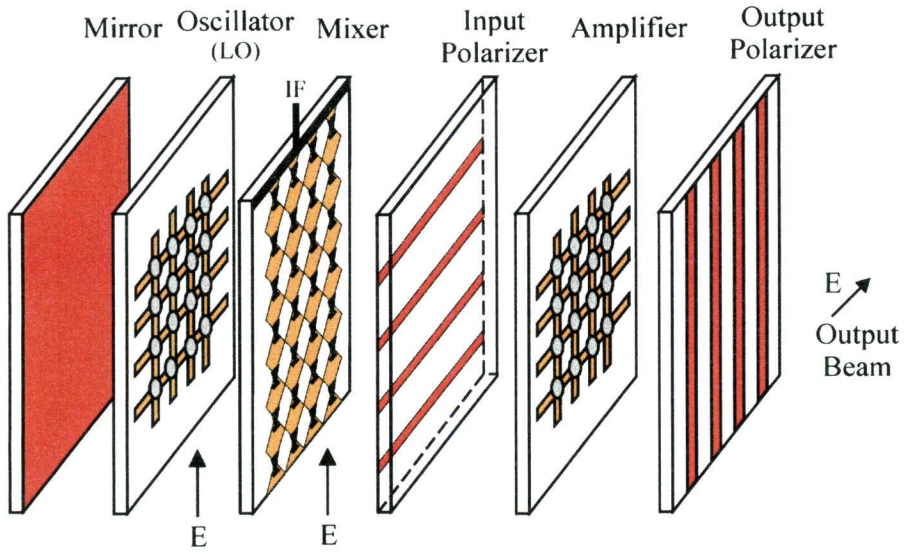

Figure 7.1. A quasi-optical transmitter.

However, there are two major challenges in building quasi-optical arrays that remain to be solved. The first is the ability to accurately model grids, and the second is building high-power arrays. Although higher power grids have been presented, the thermal issues are still the critical challenge in building quasi-optical arrays and need to be addressed.

7.1. MODELLING

Accurate modelling of grids is an area that needs more attention before grids can be designed and build reliably. Computer programs for modeling the radiating element, and the capability to do thermal and stability analysis need to be developed and used in the design of the grids. Finite-Difference-Time-Domain (FDTD) electromagnetic modeling tools along with time-domain non-linear circuit simulation (SPICE) is a possible approach.

7.2. THERMAL ISSUES

The promise of quasi-optics is to deliver high output powers at high frequencies. The biggest obstacle to overcome in achieving this, is dealing with the thermal issues of the grids. In the previous high power grids the duty cycle have been limited by the low thermal conductivity of Duroid and GaAs substrates, to pulses of less then one second [7,8,14]. For most applications this is not acceptable.

One way to deal with thermal issues is the removal of heat generated by the devices. One method is to thin the GaAs chips and mount them on a high-thermal conductivity substrate like diamond or aluminum nitride. Recent advances in CVD diamond growth have made artificial diamond substrates attractive for this application. Another method is to use flip-chip technology in mounting the devices on the substrate. In a flip-chip configuration the device is mounted adjacent to a heat sink. In the case of grids, the heat sink is the metal structure

of the grid. This is an approach that is being investigated by Polly Preventza at Caltech and Dr. Matloubian at Hughes Research Labs in Malibu.

Another approach in dealing with the thermal issues is to improve the efficiency of the grids. For example in the case of grid amplifiers the study of high efficiency grids such as class-E grid amplifiers is suggested [16].

References

[1] Z.B. Popović, M. Kim, D.B. Rutledge, "Grid Oscillators," *Int. J. Infrared Millimeter Waves*, vol. 9, pp. 647–654, July 1988.

[2] J.B. Hacker, R.M. Weikle, M. Kim, M.P. De Lisio, D.B. Rutledge, "A 100-Element Planar Schottky Diode Grid Mixer," *IEEE Trans. Microwave Theory Tech.*, vol. 40, pp. 557–562, March 1992.

[3] W.W. Lam, H.Z. Chen, K.S. Stolt, C.F. Jou, N.C. Luhmann, Jr., D.B. Rutledge, "Millimeter-Wave Diode Grid Phase Shifters," *IEEE Trans. Microwave Theory Tech.*, vol. 36, pp. 902–907, May 1988.

[4] L.B. Sjogren, H.-X.L. Liu, X.-H. Qin, C.W. Domier, N.C. Luhmann, Jr., "Phased Array Operation of a Diode Grid Impedance Surface," *IEEE Trans. Microwave Theory Tech.*, vol. 42, pp. 565–572, April 1994.

[5] M. Kim, J.J. Rosenberg, R.P. Smith, R.M. Weikle, J.B. Hacker, M.P. De Lisio, D.B. Rutledge, "A Grid Amplifier," *IEEE Microwave Guided Wave Lett.*, vol. 1, pp. 322–324, November 1991.

[6] M. Kim, E.A. Sovero, J.B. Hacker, M.P. De Lisio, J.-C. Chiao, S.-J. Li, D.R. Gagnon, J.J. Rosenberg, D.B. Rutledge, "A 100-Element HBT Grid Amplifier," *IEEE Trans. Microwave Theory Tech.*, vol. 41, pp. 1762–1771, October 1993.

[7] C.-M. Liu, E.A. Sovero, W.J. Ho, J.A. Higgins, M.P. De Lisio, D.B. Rutledge, "Monolithic 40-GHz 670-mW HBT Grid Amplifier,"

[8] M.P. De Lisio, S.W. Duncan, D.-W. Tu, S. Weinreb, C.-M. Liu, D.B. Rutledge, "A 44-60 GHz Monolithic pHEMT Grid Amplifier," *1996 IEEE MTT-S Int. Microwave Symp.*, pp. 1127–1130, 1996.

[9] J.A. Higgins, E.A. Sovero, W.J. Ho, "44-GHz Monolithic Plane Wave Amplifiers," *IEEE Microwave Guided Wave Lett.*, vol. 5, pp. 347–348, October 1995.

[10] P. Preventza, M. Matloubian, D.B. Rutledge, "A 43-GHz AlInAs/GaInAs/InP HEMT Grid Oscillator," to be presented at *The IEEE MTT-S Int. Microwave Symp.*, June 1997.

[11] J.-C. Chiao, A. Markelz, Y. Li, J. Hacker, T. Crowe, J. Allen, D.B. Rutledge, "Terahertz Grid Frequency Doublers," presented at *The 6th Int. Symp. Space Terahertz Tech.*, March 1995.

[12] A. Moussessian, M.C. Wanke, Y. Li, J.-C. Chiao, F.A. Hegmann, S.A. Allen, T.W. Crowe, D.B. Rutledge, "A Terahertz Grid Frequency Doubler," to be presented at *The IEEE MTT-S Int. Microwave Symp.*, June 1997.

[13] J.B. Hacker, M.P. De Lisio, M. Kim, C.-M. Liu, S.-J. Li, S.W. Wedge, D.B. Rutledge, "A 10-Watt X-Band Grid Oscillator," *1994 IEEE MTT-S Int. Microwave Symp. Dig.*, pp. 823–826, 1994.

[14] M.P. De Lisio, S.W. Duncan, D.-W. Tu, C.-M. Liu, A. Moussessian, J.J. Rosenberg, D.B. Rutledge, "Modelling and Performance of a 100-Element pHEMT Grid Amplifier," *IEEE Trans. Microwave Theory Tech.*, vol. 44, pp. 2136–2144, December 1996.

[15] P. Liao, R.A. York, "A High Power Two-Dimensional Coupled-Oscillator Array at X-Band," *1995 IEEE MTT-S Int. Microwave Symp.*, pp. 909–912, 1995.

[16] T.B. Mader, Z.B. Popović, "The Transmission-Line High-Efficiency Class-E Amplifier," *IEEE Microwave Guided Wave Lett.*, vol. 5, pp. 290–292, September 1995.